

DTIC FILE COPY

ARO 21438.43-EL

(2)

MICROWAVE LABORATORY REPORT NO. 88-P-2

ANALYSIS AND IMPROVEMENT OF MM-WAVE GaAs MESFET'S

TECHNICAL REPORT

SAMIR M. EL-AZHARY EL-GHAZALY

and

Tatsuo Itoh

MAY 1988

ARMY RESEARCH OFFICE

CONTRACT DAAG 29-84-K-0076

UNIVERSITY OF TEXAS

DEPARTMENT OF ELECTRICAL ENGINEERING

AUSTIN, TEXAS 78712

APPROVED FOR PUBLIC RELEASE

DISTRIBUTION UNLIMITED

DTIC
ELECTE
JUL 18 1988
S D
H

88715051

REPORT DOCUMENTATION PAGE

1a. REPORT SECURITY CLASSIFICATION Unclassified		1b. RESTRICTIVE MARKINGS	
2a. SECURITY CLASSIFICATION AUTHORITY		3. DISTRIBUTION/AVAILABILITY OF REPORT Approved for public release; distribution unlimited.	
2b. DECLASSIFICATION/DOWNGRADING SCHEDULE		4. PERFORMING ORGANIZATION REPORT NUMBER(S) Microwave Laboratory Report No. 88-P-2	
5. MONITORING ORGANIZATION REPORT NUMBER(S) ARO 21438-43-EL		6a. NAME OF PERFORMING ORGANIZATION The University of Texas	
6b. OFFICE SYMBOL (If applicable)		7a. NAME OF MONITORING ORGANIZATION U. S. Army Research Office	
6c. ADDRESS (City, State, and ZIP Code) Dept. of Electrical & Computer Engineering Austin, TX 78712		7b. ADDRESS (City, State, and ZIP Code) P. O. Box 12211 Research Triangle Park, NC 27709-2211	
8a. NAME OF FUNDING/SPONSORING ORGANIZATION U. S. Army Research Office		8b. OFFICE SYMBOL (If applicable)	
8c. ADDRESS (City, State, and ZIP Code) P. O. Box 12211 Research Triangle Park, NC 27709-2211		9. PROCUREMENT INSTRUMENT IDENTIFICATION NUMBER DAAG 29-84-K-0076	
10. SOURCE OF FUNDING NUMBERS		11. TITLE (Include Security Classification) Analysis and Improvement of MM-Wave GaAs MESFET'S	
PROGRAM ELEMENT NO		PROJECT NO	
TASK NO		WORK UNIT ACCESSION NO	
12. PERSONAL AUTHOR(S) Samir M. El-Azhary El-Ghazaly and Tatsuo Itoh			
13a. TYPE OF REPORT Technical		13b. TIME COVERED FROM TO	
14. DATE OF REPORT (Year, Month, Day) May 1988		15. PAGE COUNT 86	
16. SUPPLEMENTARY NOTATION The view, opinions and/or findings contained in this report are those of the author(s) and should not be construed as an official Department of the Army position, policy, or decision, unless so designated by other documentation.			
17. COSATI CODES		18. SUBJECT TERMS (Continue on reverse if necessary and identify by block number)	
FIELD	GROUP	SUB-GROUP	
		GaAs MESFET, Two-dimensional model, P-layer, Gunn domain	
19. ABSTRACT (Continue on reverse if necessary and identify by block number) A two-dimensional computer model, which takes into account the non-stationary conditions, is used to investigate several aspects of the GaAs submicron-gate MESFET. First, this model is used to evaluate the effect of carrier injection into the MESFET buffer-layer. It is shown that the carrier injection reduces the transconductance and increases the output conductance. One of the ways to reduce the carrier injection is to introduce a potential-barrier between the active-layer and the substrate. Therefore, the MESFET grown on a P-substrate is studied. It is shown that a high acceptor concentration in the substrate depletes large part of the active-layer and greatly reduces the output current. A more flexible design can be obtained by introducing a thin P-layer between the active-layer and the semi-insulating substrate. This model is also used in investigating the traveling Gunn domain phenomenon in GaAs MESFET's. It is shown that traveling domains exist in MESFET's with relatively thick active-layers. The propagation characteristics of these domains are studied in detail. (cont'd)			
20. DISTRIBUTION/AVAILABILITY OF ABSTRACT <input type="checkbox"/> UNCLASSIFIED/UNLIMITED <input type="checkbox"/> SAME AS RPT. <input type="checkbox"/> DTIC USERS		21. ABSTRACT SECURITY CLASSIFICATION Unclassified	
22a. NAME OF RESPONSIBLE INDIVIDUAL		22b. TELEPHONE (Include Area Code) 22c. OFFICE SYMBOL	

19. Cont'd

A new structure called Inverted-Gate FET (INGFET) is studied as well. This structure has equal input and output reactances. Hence, it relaxes the restriction on the device width which becomes very severe in the mm-wave range. Another structure that employs carrier injection over an N⁺-i junction and possesses equal input and output reactances is analyzed. It is called Inverted-Gate-Injection FET (INGIFET). The potential characteristics of the INGIFET are compared with those of the INGFET as well as the coplanar MESFET.

Handwritten: (A-1) - 41



Accession For	
NTIS CRA&I	<input checked="checked" type="checkbox"/>
DTIC TAB	<input type="checkbox"/>
Unannounced	<input type="checkbox"/>
Justification	
By.....	
Distribution/.....	
Availability Codes	
Dist	Avail and/or Special
A-1	

MICROWAVE LABORATORY REPORT NO. 88-P-2

ANALYSIS AND IMPROVEMENT OF MM-WAVE GaAs MESFET'S

TECHNICAL REPORT

SAMIR M. EL-AZHARY EL-GHAZALY

MAY 1988

ARMY RESEARCH OFFICE

CONTRACT DAAG 29-84-K-0076

UNIVERSITY OF TEXAS

DEPARTMENT OF ELECTRICAL ENGINEERING

AUSTIN, TEXAS 78712

APPROVED FOR PUBLIC RELEASE

DISTRIBUTION UNLIMITED

ANALYSIS AND IMPROVEMENT OF MM-WAVE GaAs MESFET'S

A two-dimensional computer model, which takes into account the non-stationary conditions, is used to investigate several aspects of the GaAs submicron-gate MESFET.

First, this model is used to evaluate the effect of carrier injection into the MESFET buffer-layer. It is shown that the carrier injection reduces the transconductance and increases the output conductance. One of the ways to reduce the carrier injection is to introduce a potential-barrier between the active-layer and the substrate. Therefore, the MESFET grown on a P-substrate is studied. It is shown that a high acceptor concentration in the substrate depletes large part of the active-layer and greatly reduces the output current. A more flexible design can be obtained by introducing a thin P-layer between the active-layer and the semi-insulating substrate.

This model is also used in investigating the traveling Gunn domain phenomenon in GaAs MESFET's. It is shown that traveling domains exist in MESFET's with relatively thick active-layers. The propagation characteristics of these domains are studied in detail.

A new structure called Inverted-Gate FET (INGFET) is studied as well. This structure has equal input and output reactances. Hence, it relaxes the restriction on the device width which becomes very severe in the mm-wave range. Another structure that employs carrier injection over an N^+ -i junction and possesses equal input and output reactances is analyzed. It is called Inverted-Gate-Injection FET (INGIFET). The potential characteristics of the INGIFET are compared with those of the INGFET as well as the coplanar MESFET.

Table of Contents

List of figures	viii
List of tables	x
List of symbols	xi
 Chapter 1. Numerical Simulation of the Submicron-Gate Field Effect Transistor	 1
1.1 Introduction	1
1.2 Brief review of numerical modelling techniques	2
1.3 The mathematical model	4
1.3.1 The conservation equations	4
1.3.2 The equivalent single electron gas model	6
1.4 Boundary conditions	11
1.4.1 Boundary conditions on free surfaces	11
1.4.2 Boundary conditions on the electrodes	13
1.5 The numerical model	14
1.5.1 Solution of the continuity and energy equations	14
1.5.1.1 Explicit scheme	15
1.5.1.2 Implicit scheme	15
1.5.1.3 Semi-implicit scheme	16
1.5.2 Solution of Poisson's equation	17
1.6 General Discussion	17
 Chapter 2. Carrier Injection Reduction Using MESFET's on P-Substrates and on Thin P-Layers	 20
2.1 Introduction	20
2.2 Effect of carrier injection	21
2.2.1 MESFET on buffer-layer	21
2.2.2 Substrate-less MESFET	25
2.2.3 MESFET with an interfacial -barrier	26

2.2.4	Comparison of the characteristics	30
2.3	MESFET on a P-substrate	34
2.4	MESFET on a thin P-layer	36
Chapter 3. Travelling Gunn Domains in GaAs MESFET's		41
3.1	Introduction	41
3.2	Traveling Gunn domain inside the MESFET	42
3.3	Source and drain currents as functions of time	51
3.4	The oscillation frequency	51
3.5	Effect of gate voltage	53
3.6	Stable structure	55
Chapter 4. Inverted-Gate Field-Effect-Transistors; Novel High Frequency Structures		57
4.1	Introduction	57
4.2	Inverted-gate FET	58
4.3	Comparison between INGFET and coplanar MESFET	62
4.4	Inverted-gate-injection FET	71
Chapter 5. Conclusion		80
References		83

List of Figures

1.1. Comparison between (a) the energy evolution and (b) the velocity evolution obtained using hydro-dynamic model and MC model.	3
1.2. (a) The actual MESFET configuration and (b) the simulated structure.	12
1.3. The contour plots of a MESFET.	19
2.1. The MESFET on a Buffer-layer.	22
2.2. The I-V characteristics of the MESFET on a buffer-layer.	23
2.3. The contour plots of the MESFET on a buffer-layer.	24
2.4. Percentage of the current passing through the buffer-layer to the total current.	24
2.5. The symmetrical MESFET.	25
2.6. The I-V characteristics of the substrate-less MESFET.	27
2.7. The contour plots of the substrate-less MESFET.	27
2.8. The I-V characteristics of the MESFET with an interfacial barrier.	28
2.9. The contour plots of the MESFET with an interfacial barrier.	29
2.10. The I-V characteristics of the three MESFET's at $V_g = 0.0$ V.	30
2.11. The transconductance of the three devices.	31
2.12. The gate-to-source capacitance of the three devices.	32
2.13. The current-gain cutoff frequency of the three devices.	33
2.14. The drain conductance of the three devices.	33
2.15. The contour plots of the MESFET on a P-substrate, $N_a = 10^{16} \text{ cm}^{-3}$.	35
2.16. The I-V characteristics of all the MESFET's at $V_g = 0.0$ V.	37
2.17. The contour plots of the MESFET on a thin P-layer, $N_a = 10^{16} \text{ cm}^{-3}$.	39
3.1. The simulated MESFET.	42
3.2. The contour plots of the simulated MESFET at $t = 0.5$ ps.	43
3.3. The contour plots of the simulated MESFET at $t = 2.0$ ps.	45
3.4. The contour plots of the simulated MESFET at $t = 3.0$ ps.	46
3.5. The contour plots of the simulated MESFET at $t = 4.0$ ps.	47
3.6. The contour plots of the simulated MESFET at $t = 5.5$ ps.	48
3.7. The contour plots of the simulated MESFET at $t = 7.0$ ps.	49

3.8.	The contour plots of the simulated MESFET at $t = 10.0$ ps.	50
3.9.	Transient source and drain currents of the MESFET after applying the 2.0 volt step on the drain at $t = 0$.	52
3.10.	The contour plots of the simulated MESFET at steady state.	54
3.11.	The I-V characteristics of the MESFET of $0.15\text{ }\mu\text{m}$ active-layer thickness.	56
4.1.	(a) The actual Inverted-Gate FET and (b) the simulated one.	59
4.2.	The contour plots of the INGfet at $V_g = -0.5\text{ V}$ and $V_{ds} = 5.0\text{ V}$.	60
4.3.	The contour plots of the INGfet at $V_g = -1.0\text{ V}$ and $V_{ds} = 5.0\text{ V}$.	60
4.4.	Dimensions of the simulated (a) INGfet and (b) the coplanar MESFET.	63
4.5.	The contour plots of Device II.	64
4.6.	The I-V characteristics of the INGfet, Device II.	65
4.7.	The I-V characteristics of the coplanar MESFET, Device III.	65
4.8.	The contour plots of the coplanar MESFET.	67
4.9.	The substrate current as a percentage of the total device current .	68
4.10.	The transconductance of the INGfet and the coplanar MESFET.	69
4.11.	The gate-to-source capacitance of the INGfet and the coplanar MESFET.	70
4.12.	The Inverted-Gate-Injection FET.	71
4.13.	The drain current variation of the INGIFET with the drain voltage for three different intrinsic region lengths.	73
4.14.	The contour plots of the INGIFET.	74
4.15.	The I-V characteristics of the INGIFET, Device IV.	75
4.16.	The I-V characteristics of the INGIFET, Device V.	76
4.17.	The transconductance of the INGIFET, Device V.	77
4.18.	The gate-to-source capacitance of the INGIFET, Device V.	78
4.19.	The current-gain cutoff frequency of Device II, Device III, and Device V.	79

List of Tables

2.1 Summary of the MESFET parameters at $V_{ds} = 4.0$ V
--

40

List of Symbols

C_{gs}	Gate-to-source capacitance.
D	Diffusion coefficient.
E	Electric field.
E_x	Electric field in the x direction.
f	Frequency.
f_t	Current-gain cutoff frequency.
f	Electron distribution function.
g_d	Drain conductance.
g_m	Transconductance.
h	Planck's constant divided by 2π .
I_d	Drain current.
I	Conduction current density (drift + diffusion) divided by the electronic charge.
k_B	Boltzmann constant.
K	Wave vector.
L_i	Intrinsic-layer length in the INGIFET.
m	Electron effective mass.
L_{gd}	Gate-to-drain separation.
n	Free electron concentration.
n_g	Charge density on the gate.
N_a	Acceptor concentration.
N_d	Donor concentration.

p_{xi}	Electron momentum in the x direction in the ith valley.
q	Electron charge.
\mathbf{r}	Position vector.
t	Time.
T	Temperature.
$T(\epsilon), T_i$	Electron temperature (energy dependant).
\mathbf{v}	Electron velocity.
v_s	Saturation velocity.
v_x	Electron velocity in the x direction.
V	Voltage.
V_{bi}	Junction built-in potential.
V_{ds}	Drain-to-source voltage.
V_g	Externally applied gate voltage.
V_{gs}	Gate-to-source voltage.
V_p	Pinch-off voltage.
V_{pb}	Potential barrier.
ϵ	Permittivity.
ϵ	Average electron energy (kinetic + potential).
$(\frac{\partial f}{\partial t})_c$	Rate of change of f due to collision
$(\frac{\partial n_i}{\partial t})_c$	Rate of change of n in the ith valley due to collision.
$(\frac{\partial (n_i \epsilon_i)}{\partial t})_c$	Rate of change of $n\epsilon$ in the ith valley due to collision.

$\left(\frac{\partial p_{xi}}{\partial t} \right)_c$ Rate of change of momentum in the x direction inside the ith valley due to collision.

$\Delta x, \Delta y$ Mesh spacings in the x and y directions respectively.

∇_k Differential operator in the K space $\left(\frac{\partial}{\partial k_x} \frac{ax}{\partial k_x} + \frac{\partial}{\partial k_y} \frac{ay}{\partial k_y} + \frac{\partial}{\partial k_z} \frac{az}{\partial k_z} \right)$

∇_r Differential operator in the real space $\left(\frac{\partial}{\partial x} \frac{ax}{\partial x} + \frac{\partial}{\partial y} \frac{ay}{\partial y} + \frac{\partial}{\partial z} \frac{az}{\partial z} \right)$

$\mu(\epsilon)$ Electron mobility (energy dependant).

$\tau_\epsilon(\epsilon)$ Energy relaxation time (energy dependant).

$\tau_{pii}(\epsilon_i)$ Time constant of momentum loss by intravalley scattering.

$\tau_{pij}(\epsilon_i)$ Time constant of momentum loss by intervalley scattering.

CHAPTER 1.

NUMERICAL SIMULATION OF THE SUBMICRON-GATE FIELD-EFFECT TRANSISTOR

1.1. INTRODUCTION

GaAs Metal-Semiconductor Field-Effect Transistors (MESFET's) are principal devices in the microwave and mm-wave low-noise and power applications. A major part of the current research is directed towards the development of high-speed-submicron-gate FET's. However, the cost of technology necessary to realize sub-half-micron-gate FET's and the uncertainty associated with the available fabrication and measuring techniques necessitate the development and the reliance on analytical and numerical simulation models to obtain a good physical insight to the operation and the potential of these devices.

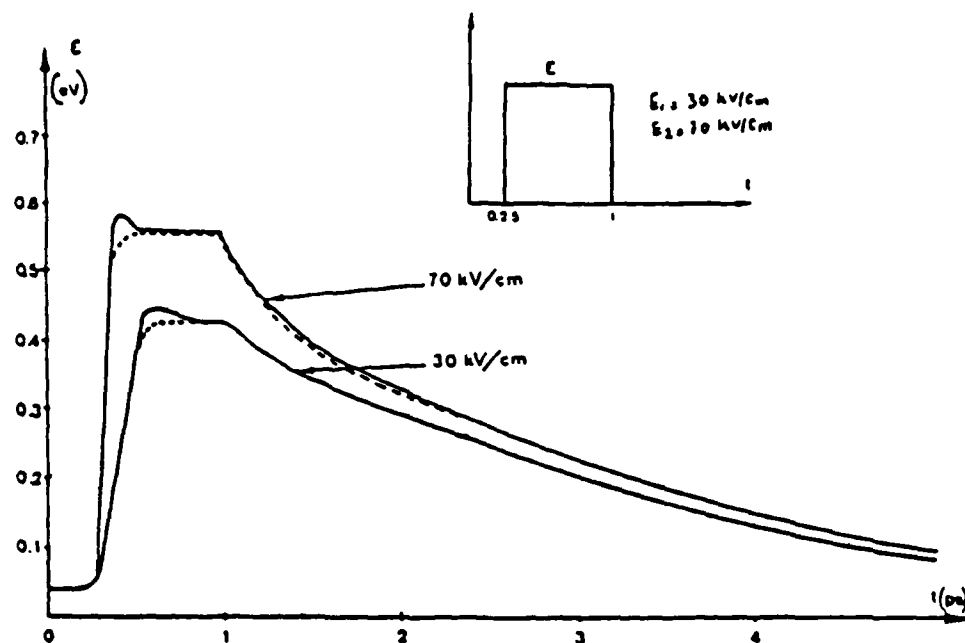
One dimensional models were used quite often in the beginning. Later, two dimensional numerical models became very popular. The necessity of the introduction of two dimensional effects in submicron-gate MESFET simulation is mainly stimulated by the planar structures usually adopted, the small gate-length employed, and the reduced thickness of the active-layer which is associated by large electric field in the gate region affecting the electron transport in both longitudinal and transverse directions. Moreover, for the thin active-layers ($0.05 \sim 0.15 \mu\text{m}$) and the large dopings ($10^{17} \sim 5 \times 10^{17} \text{ cm}^{-3}$) currently employed, the depletion-layer width becomes comparable to the Debye length. Therefore, the use of the concept of a completely deserted depletion region frequently adopted in one dimensional and pseudo two dimensional models, is completely forbidden. Furthermore, the relative importance of the fringing field of the gate electrode increases as the gate-length decreases below one micron. In the same time, the introduction of the momentum and energy relaxation effects becomes imperative for these submicron-gate lengths. In fact, the two dimensional aspects and the non-stationary electron dynamics are closely related and should always be considered simultaneously in treating these devices [1].

1.2. BRIEF REVIEW OF NUMERICAL MODELLING TECHNIQUES

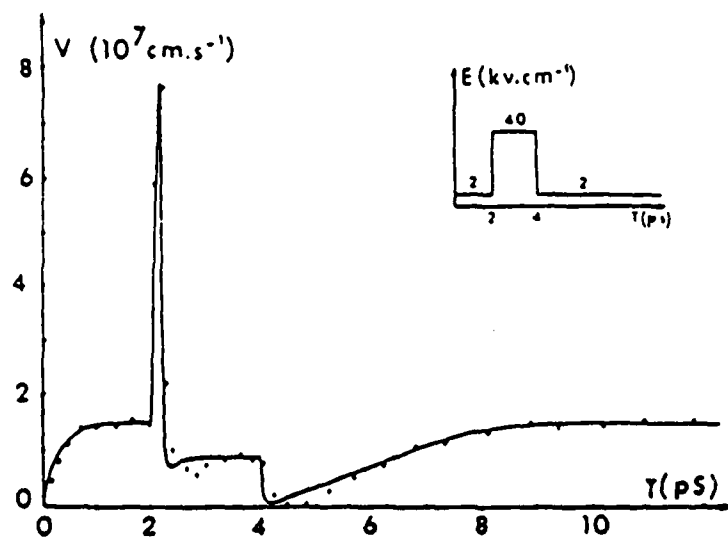
During the last two decades, several theoretical models have been developed. For example, Reiser [2], Yamaguchi *et al.* [3], and Barnes *et al.* [4] developed numerical models for the FET's based on the quasi-stationary approximation. By the quasi-stationary approximation it is meant that the mobility and diffusion coefficient are instantaneous functions of the local electric field. Actually, the mobility requires finite time before it completely adjusts itself to a change in the electric field. This time is in the order of few pico-seconds. Thus, it cannot be neglected compared to the electron transit time in the submicron-gate MESFET's. This simplifying approximation precluded the use of these models to study the modern MESFET's.

Monte-Carlo (MC) simulation techniques have been applied effectively to many electron-dynamic problems. This method, in its simplest form, depends on the observation of a number of electrons simulating directly the stochastic process studied. The electrons are scattered on their way through the substance by ionized impurities, acoustic and optical phonons, ... etc. These scatterings may be inter or intravalley. The program selects the appropriate scattering events using the statistical MC method in such a way that, on a long run, the different scattering mechanisms are chosen with the same frequency as in the real device. The flight time of the electrons between two successive scatterings is statistically chosen using MC as well (for more references see [5] or [7]). This method is phenomenologically correct and simulates the physical device behavior. However, this method suffers from low accuracy and random numerical fluctuations, due to the stochastic motion of the carriers. Therefore, large number of carriers must be used which drastically increase the computational effort. Hence, this method requires very long computation time and powerful computers [1].

A compromise between the two approaches was proposed by Shur [6],[7]. In this method, the scattering events are not dealt with on an individual scale but introduced on a collective and macroscopic scale through the use of momentum and energy relaxation time concepts. The momentum relaxation time, the energy relaxation time, the mobility, and the effective mass are considered dependent only on the average electron energy. Their values, for a given energy, are obtained from the results of MC simulation at steady state. This method was applied to GaAs. The results are in a very good agreement with those of MC [5],[7] as shown in Fig. 1.1.



(a)



(b)

Fig. 1.1 (a) Comparison between the energy evolution with time obtained using "—" hydro-dynamic model and "---" MC model; reprinted after [5]. (b) The velocity evolution with time. The solid line represents the solution using the hydro-dynamic model and the points represent MC solution [5].

Cappy [8] made use of this bona fide method to develop a one dimensional model that takes into account the non-stationary conditions. However, due to the necessary approximations required for a one dimensional model, this program could not consider some important phenomena such as the carrier injection into substrates and the gradual transition from the depletion region to the channel. Such effects can be accounted for by introducing correction factors, as Cappy has already done in his model. It should be noted that such models are more suitable for computer aided design (CAD) than to predict the physical behavior of the devices.

Cook *et al.* [9] developed a more elaborate program based on a two dimensional solution of the continuity and Poisson's equations and one dimensional solution of the energy conservation equ., assuming no energy variation in the transverse direction. The latter approximation reduces the accuracy of this program due to the large transverse field under the MESFET gate.

Curtice *et al.* [10] developed a similar temperature model, in which the energy conservation equ. is solved in two dimensions simultaneously with the other two equations. It was reported that this model predicts higher drain currents and transconductances than the quasi stationary models. It was also reported that the temperature model results are in much better agreement with the design charts than the quasi static ones.

The model used in this study employs the same concept as in [9] and [10] but with a full two dimensional solution and more elaborate formulation of the energy conservation equ. [11]. It was developed separately at about the same time as the other models. Recently, Snowden *et al.* [12] reported a model which is very close to that in [11] as far as the formulation is concerned.

1.3. THE MATHEMATICAL MODEL

1.3.1. THE CONSERVATION EQUATIONS

For submicron gate FET's, of gate length not less than $0.1 \mu\text{m}$, the Boltzmann Transport Equation (BTE) is a valid approximation to accurately describe the electron transport phenomena [1]. This equation specifies the time and spatial variation of the electron distribution function, $f(\mathbf{r}, \mathbf{k}, t)$, as follows:

$$\frac{\partial f}{\partial t} + \mathbf{v} \cdot \nabla_r f + \frac{q\mathbf{E}}{\hbar} \cdot \nabla_k f = \left(\frac{\partial f}{\partial t} \right)_c \quad (1.1)$$

BTE represents the starting point as it will be used to deduce the conservation equations employed in model used through out this work. These equations are obtained by integrating the BTE over the \mathbf{K} space to obtain its moments. The details of this integration are given in some other references, [8], [13] and [14]. A brief outline is given here. Assuming parabolic energy bands and adopting positive electron notation, the procedure can be summarized in the following steps:

Integrating BTE over the i th valley in the \mathbf{K} space produces

$$\frac{\partial n_i}{\partial t} + \nabla \cdot (n_i \mathbf{v}_i) = \left(\frac{\partial n_i}{\partial t} \right)_c \quad (1.2)$$

which is known as Particles Conservation Equation. Multiplying BTE by the electron momentum in the x direction (mv_x) and integrating over the i th valley, the momentum conservation equation in the x direction is obtained as

$$\frac{\partial P_{xi}}{\partial t} + \nabla \cdot (P_{xi} \mathbf{v}_i) = qn_i E_x - \frac{\partial (n_i k_B T_i)}{\partial x} + \left(\frac{\partial P_{xi}}{\partial t} \right)_c \quad (1.3)$$

There are two similar equations for the momentum in the y and z directions. Multiplying BTE by the electron energy and integrating over the i th valley, the energy conservation equation is obtained as

$$\frac{\partial (n_i \epsilon_i)}{\partial t} + \nabla \cdot (n_i \mathbf{v}_i \epsilon_i) = qn_i \mathbf{v}_i \cdot \mathbf{E} - \nabla \cdot (n_i k_B T_i \mathbf{v}_i) + \left(\frac{\partial (n_i \epsilon_i)}{\partial t} \right)_c \quad (1.4)$$

In equations (1.2)-(1.4), the subscript i indicates that the variable is averaged over the i th valley.

The physical meaning of these equations can be interpreted as follows. In equ. (1.2), the left-hand side represents the total variation in the number of electrons in the i th valley as $(\partial n_i / \partial t)$ is the time-rate of increase of the number of electrons and $(\nabla \cdot (n_i \mathbf{v}_i))$ is the rate of outward flux of electrons from the i th valley per unit

volume. The term $(\partial n_i / \partial t)_c$ represents the rate of increase of the number of the i th valley electrons per unit volume due to the net effect of scattering from and to this valley.

Equ. (1.3) represents the balance of momentum per unit volume for the electrons in the i th valley. The left-hand side represents the total rate of change of momentum with respect to time. The term $(qn_i E_x)$ represents the electric force and $(\partial(n_i k_B T_i) / \partial x)$ represents the force due to the electronic pressure. $(\partial P_{xi} / \partial t)_c$ is the force due to collisions

The terms of equation (1.4) can be interpreted in the same way. The left-hand side is the total rate of change of the electrons in the i th valley per unit volume with respect to time. The term $(qn_i v_i \cdot E)$ represents the power gained by the electrons from the electric field. $(\nabla \cdot (n_i k_B T_i v_i))$ is the time rate of work done, or the energy lost, by the electrons in expansion. The term $(\partial(n_i \epsilon_i) / \partial t)_c$ represents the time rate of change of the electrons energy due to collisions.

These equations are valid only for one valley which may be either the lower valley (L) or the upper valley (U) in the case of GaAs. Treating this problem using a two-electron-gas model, one for each valley, with two distinct characteristics and performing the solution in two dimensions is unfavorable due to the excessive memory and CPU time required to solve these highly nonlinear and strongly coupled equations. Moreover, this would be a deviation from the main goal of this approach, namely the simplification. The other alternative is to solve the problem of the equivalent single electron gas. The characteristics of this single electron gas are the weighted average characteristics of the two constituting gases. The latter alternative is adopted in developing the model presented here.

1.3.2. THE EQUIVALENT SINGLE ELECTRON GAS MODEL

The three conservation equations, derived before, has to be averaged over the two, or in general more, valleys of the semiconductor. The averaging procedure is handled in an as precise form as possible, but it is always necessary to make some assumptions.

Consider the carrier conservation equation (1.2). Summing over all the valleys

$$\sum_i \frac{\partial n_i}{\partial t} + \sum_i \nabla \cdot (n_i \mathbf{v}_i) = \sum_i \left(\frac{\partial n_i}{\partial t} \right)_c \quad (1.5)$$

The right-hand side represents the total number of electrons exchanged between the valleys. Hence, this term is equal to zero. The left-hand terms are:

$$\sum_i \frac{\partial n_i}{\partial t} = \frac{\partial}{\partial t} \sum_i n_i = \frac{\partial n}{\partial t} \quad (1.6)$$

where n is the total particle density;

$$\sum_i \nabla \cdot (n_i \mathbf{v}_i) = \nabla \cdot \left(\sum_i (n_i \mathbf{v}_i) \right) = \nabla \cdot (n \langle \mathbf{v} \rangle) \quad (1.7)$$

$$\langle \mathbf{v} \rangle = \frac{\sum_i (n_i \mathbf{v}_i)}{\sum_i n_i} \quad (1.8)$$

$\langle \mathbf{v} \rangle$ is the average electron velocity over all the valleys. Hence, (1.5) becomes

$$\frac{\partial n}{\partial t} + \nabla \cdot (n \langle \mathbf{v} \rangle) = 0 \quad (1.9)$$

which is the continuity equation.

For the momentum conservation equation, knowing that the momentum relaxation-time is about one order of magnitude lower than the energy relaxation-time permits us to neglect the inertia effects in equation (1.3). The physical meaning of this assumption is that the electron momentum is able to adjust itself to a change in the electric field within a time that is much shorter than that required by the electron energy. Therefore, this adjustment time becomes negligible compared to the other ones in the problem at hand. We believe that this assumption is valid up to gate lengths as short as 0.1 μm . It is interesting to notice that this assumption is employed by the other authors who developed similar programs [8]-[12], although some of them did not mention it explicitly. Mathematically, this assumption means equating the left-hand side of equation (1.3) to zero. Hence

$$\frac{\partial p_{xi}}{\partial t} + \nabla \cdot (p_{xi} v_i) = q n_i E_x - \frac{\partial (n_i k_B T_i)}{\partial x} + \left(\frac{\partial p_{xi}}{\partial t} \right)_c = 0 \quad (1.10)$$

The collision term can be written as [13]:

$$\left(\frac{\partial p_{xi}}{\partial t} \right)_c = - m_i n_i v_{xi} \left(\frac{1}{\tau_{pii}(\epsilon_i)} + \frac{1}{\tau_{pij}(\epsilon_i)} \right) \quad (1.11)$$

where

- $\tau_{pii}(\epsilon_i)$: time constant of momentum loss by intravalley scattering.

- $\tau_{pij}(\epsilon_i)$: time constant of momentum loss by intervalley scattering.

Substituting equ. (1.11) into (1.10) and rearranging, one obtains

$$n_i v_{xi} = \mu_i(\epsilon_i) \left(n_i E_x - \frac{\partial (n_i k_B T_i(\epsilon_i))}{\partial x} \right) \quad (1.12)$$

where

$$\mu_i(\epsilon_i) = \frac{q}{m_i} \frac{1}{\left(\frac{1}{\tau_{pii}(\epsilon_i)} + \frac{1}{\tau_{pij}(\epsilon_i)} \right)} \quad (1.13)$$

Performing the summation over all the valleys, one gets

$$\sum_i n_i v_{xi} = \left(\sum_i n_i \mu_i(\epsilon_i) \right) E_x - \sum_i \left(\mu_i(\epsilon_i) \frac{\partial}{\partial x} \left(\frac{k_B T_i(\epsilon_i) n_i}{q} \right) \right) \quad (1.14)$$

Using the same definition of the average quantities as in equ. (1.8)

$$\sum_i n_i v_{xi} = n \langle v_x \rangle \quad (1.15)$$

and

$$\sum_i n_i \mu_i(\epsilon_i) = n \langle \mu(\epsilon) \rangle \quad (1.16)$$

and assuming that the product of averages equals the average of products [8], then

$$\sum_i \left(\mu_i(\epsilon_i) \frac{\partial}{\partial x} \left(\frac{k_B T_i(\epsilon_i) n_i}{q} \right) \right) = \langle \mu(\epsilon) \rangle \frac{\partial}{\partial x} \left(\frac{k_B \langle T(\epsilon) \rangle n}{q} \right) \quad (1.17)$$

Substituting in equ. (1.14),

$$n \langle v_x \rangle = \langle \mu(\epsilon) \rangle \left(n E_x - \frac{\partial}{\partial x} \left(\frac{k_B \langle T(\epsilon) \rangle n}{q} \right) \right) \quad (1.18)$$

Two other similar equations can be derived for the y and the z directions. The three dimensional form becomes:

$$n \underline{v} = \langle \mu(\epsilon) \rangle \left(n \underline{E} - \nabla \left(\frac{k_B \langle T(\epsilon) \rangle n}{q} \right) \right) \quad (1.19)$$

Proceeding to the energy conservation equation, (1.4), performing the summation over all the valleys and using the definition of averages, one obtains

$$\frac{\partial (n \langle \epsilon \rangle)}{\partial t} + \nabla \cdot (n \langle \epsilon \rangle \underline{v}) = q n \langle v \rangle \cdot \underline{E} - \nabla \cdot (n k_B \langle T(\epsilon) \rangle \underline{v}) + \left(\frac{\partial (n \langle \epsilon \rangle)}{\partial t} \right)_c \quad (1.20)$$

The collision term can be evaluated as [13]:

$$\left(\frac{\partial (n \langle \epsilon \rangle)}{\partial t} \right)_c = - \frac{n (\langle \epsilon \rangle - \epsilon_0)}{\tau_\epsilon (\langle \epsilon \rangle)} \quad (1.21)$$

Therefore, the average energy conservation equation becomes

$$\frac{\partial (n \langle \epsilon \rangle)}{\partial t} + \nabla \cdot (n \langle \epsilon \rangle \langle \underline{v} \rangle) = q n \langle \underline{v} \rangle \cdot \underline{E} - \nabla \cdot (n k_B \langle T(\epsilon) \rangle \langle \underline{v} \rangle) - \frac{n (\langle \epsilon \rangle - \epsilon_0)}{\tau_\epsilon (\langle \epsilon \rangle)} \quad (1.22)$$

It is interesting to note that some other formulations for the conservation equations can also be derived. They may, or may not, be equal to the set derived here. However, the previously presented set was finally selected from among other formulations which was programmed. The selection was based on physical, mathematical and numerical reasons [15].

Adding Poisson's equ.to this set, one obtains a complete set of equations that is capable of accurately describing the carrier transport inside the multi-valley semiconductors (e.g. GaAs, AlGaAs, InP.....etc.). The main feature of this model is that all the material related parameters such as mobility, electron temperature and energy-relaxation time are functions of the average electron energy. They are obtained from Monte-Carlo simulations at steady state. To summarize, the four basic equations, after dropping the average sign for simplicity, are:

$$\frac{\partial n}{\partial t} + \nabla \cdot (n \underline{v}) = 0 \quad (1.23a)$$

$$\underline{J} = n \underline{v} = \mu(\epsilon) \left(n \underline{E} - \nabla \left(\frac{n k_B T(\epsilon)}{q} \right) \right) \quad (1.23b)$$

$$\frac{\partial (n \epsilon)}{\partial t} + \nabla \cdot (\underline{J} \epsilon) = q \underline{J} \cdot \underline{E} - \nabla \cdot (k_B T(\epsilon) \underline{J}) - \frac{n (\epsilon - \epsilon_0)}{\tau_\epsilon(\epsilon)} \quad (1.23c)$$

$$\nabla^2 V = - \frac{q}{\epsilon} (n - N_d) \quad (1.23d)$$

All the equations are written employing positive electron notation. The basic variables are the carrier concentration (n), the electric potential (V) and the carriers energy (ϵ).

1.4. BOUNDARY CONDITIONS

In the actual MESFET, the source and the drain electrodes are much longer than the gate electrode. Moreover, to prevent the lattice imperfections of the substrate from reaching the active-layer, a buffer-layer is epitaxially grown between the active-layer and the substrate as shown in Fig. 1.2(a). Simulating the MESFET with its actual dimensions is impractical and unnecessary. It is impractical due to the large computer memory and time required. Furthermore, it is unnecessary since the main electron transport phenomena occur in the active-layer under the gate and in a small fraction of the upper part of the buffer-layer. This permits us to reduce the simulated part of the device to that shown in Fig. 1.2(b). One should notice that the dimensions of the simulated part have to be adequately chosen such that they do not affect the main object of the simulation. For example, the reduction of the total source and drain lengths slightly affects the calculation of the parasitic source and drain resistances. Nevertheless, the calculation of such parameters is not the main goal of this study. These parameters can be introduced as resistive correction elements in the small signal equivalent circuit. On the other hand, the simulated depth of the buffer-layer has to be chosen such that the current carried by the rest of the buffer-layer is negligibly small.

1.4.1. BOUNDARY CONDITIONS ON FREE SURFACES

One of the main features of the new boundaries is that, at equilibrium, there is no current flow except from the source and the drain contacts. This can be introduced in the model by applying Neumann boundary conditions away from the electrodes as follows:

- 1- To ensure zero drift current out of the free surface, the electric field normal to the surface has to be zero, which means

$$\partial V / \partial u = 0. \quad (1.24a)$$

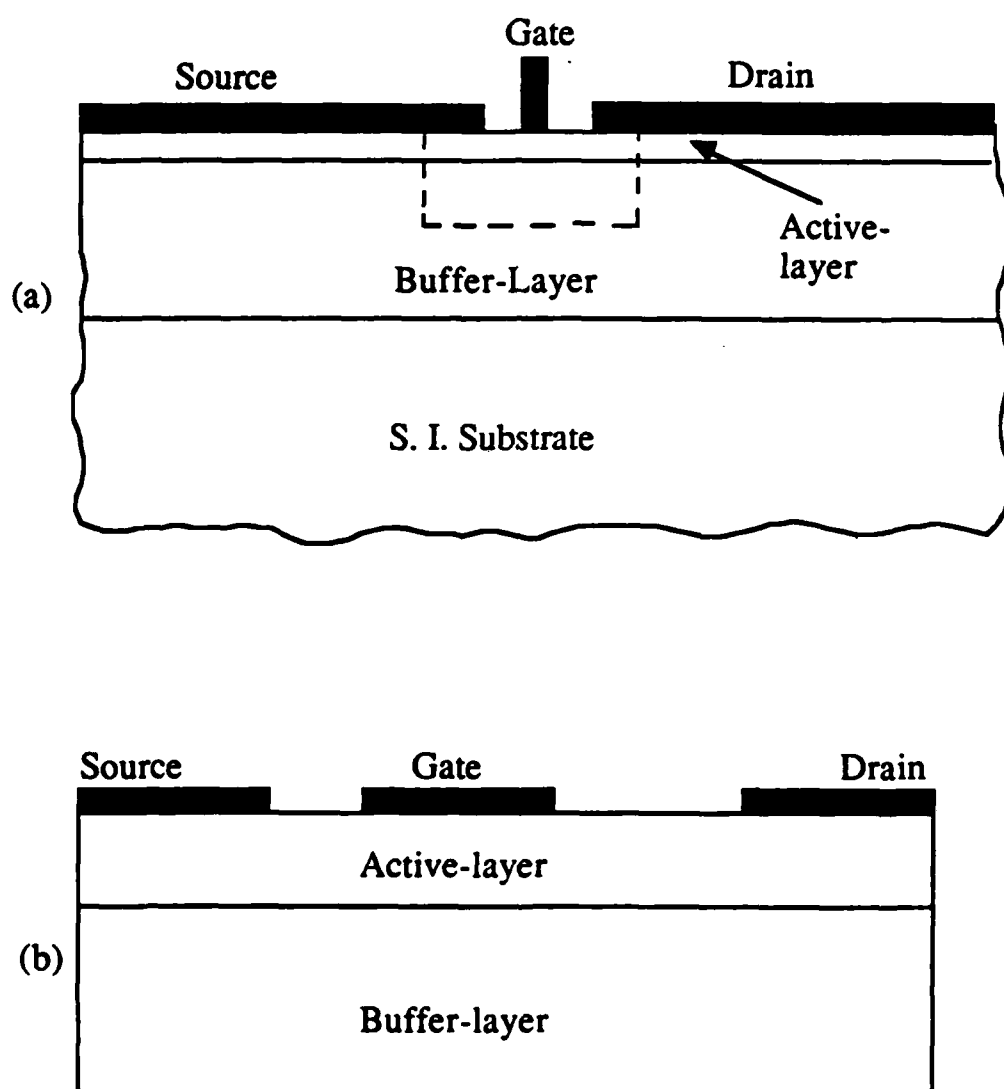


Fig. 1.2. (a) The actual MESFET configuration and (b) the simulated structure.

- 2- To ensure zero diffusion current out of the free surface, the gradient of the carriers and the electron temperature have to be zeros. Then

$$\partial n / \partial u = 0. \quad (1.24b)$$

$$\partial T(\epsilon) / \partial u = 0.$$

which, in terms of the basic variables, means

$$\partial \epsilon / \partial u = 0. \quad (1.24c)$$

Where \underline{u} is a unit vector normal to the free surface.

It should be noted that the surface potential is not explicitly taken into account. However, it is equivalent to a recess structure with a recess equal to the width of the depletion region caused by the surface potential. In other words, it may be regarded as simulating a MESFET with a thicker active-layer than that stated in the program.

1.4.2. BOUNDARY CONDITIONS ON THE ELECTRODES

At the source and the drain ohmic contacts, Dirichlet boundary conditions are applied to allow a current to flow freely from and to the device. Mathematically, this boundary condition means:

- 1- The voltage is constant and equals 0 at the source and V_d at the drain.
- 2- The charge is constant and is equal to N_d at both electrodes.
- 3- The energy is constant and is equal to $3 k_B T_c / 2$ at both electrodes.

The gate rectifying junction is simulated by setting its potential to a fixed value (V_{gs}) which equals the built-in potential, - 0.8 V, plus the external voltage applied to the gate (V_g). For the particle concentration, two possible methods exist:

- 1- Applying a boundary condition on the carrier density on the gate (n_g) as obtained from the physical conditions at the junction, such that

$$n_g = N_d e^{\left(\frac{-q |V_{gs}|}{k_B T} \right)} \quad (1.25)$$

The depletion region is created by the transverse electric field. The net

current flow becomes zero once the balance between the drift and diffusion components of the current is reached.

- 2- Setting the conduction current out of the gate to zero while leaving the charge concentration floating on the gate surface. The value of n_g can be updated each time step using the continuity equation.

Although the first method is widely used, it gives rise in the numerical computation scheme due to the appearance of a gate current resulting from the unbalance between the diffusion and the drift current components in the depletion region. The difference in current, though numerically very small, produces erroneous energy values under the gate due to the large transverse field in the gate depletion region. The second method, which is introduced for the first time in this program, is invented specially to overcome this problem. It resulted in a more stable convergence and a much smaller numerical difference between the source and the drain currents [15].

The energy at the gate is equated to the thermal energy which is an acceptable boundary condition for the metal-semiconductor interface.

1.5. THE NUMERICAL MODEL

The previously described equations are discretized in a two dimensional mesh using the finite difference scheme. The continuity equ. and the energy conservation equ. are highly-nonlinear and strongly-coupled partial-differential equations. Therefore, they have high potential to develop numerical instability. Extreme care has to be taken in discretizing them in space and decoupling them in time in order to obtain a strongly stable program.

1.5.1. SOLUTION OF THE CONTINUITY AND ENERGY EQUATIONS

To explain the possible discretization schemes, consider the case of continuity equation (1.23a) as an example.

$$\frac{\partial n}{\partial t} + \nabla \cdot \mathbf{J} = 0$$

Discretizing it into N mesh points in the x direction and M mesh points in the y direction, this equation becomes

$$\frac{n_{ij}^{k+1} - n_{ij}^k}{\Delta t} + \frac{1}{2} (\nabla \cdot \mathbf{J}^{k+1} + \nabla \cdot \mathbf{J}^k) = 0 \quad (1.26)$$

where the subscripts i and j denote the location in space and the superscript denotes the time discretization. Let

$$\nabla \cdot \mathbf{J}^k = \Psi (n^k, \mathbf{E}^k, \mu^k, T^k) \quad (1.27)$$

There are three possibilities in formulating this equation further.

1.5.1.1. Explicit Scheme

In this scheme, it is assumed that $\nabla \cdot \mathbf{J}^{k+1} = \nabla \cdot \mathbf{J}^k$, then equation (1.26) becomes

$$\frac{n_{ij}^{k+1} - n_{ij}^k}{\Delta t} + \Psi (n^k, \mathbf{E}^k, \mu^k, T^k) = 0 \quad (1.28)$$

which is very simple from the numerical point of view since the new state is got in one shot calculation. However, the disadvantage of this scheme is its large tendency to develop numerical instability [16]. Hence, the time increment, Δt has to be so small such that it satisfies the following the condition

$$\Delta t \leq \min \left\{ \frac{\Delta x^2 \Delta y^2}{2 (\Delta x^2 + \Delta y^2) D_{\max}}, \frac{2 D}{v_{\max}^2} \right\} \quad (1.29)$$

where min means the minimum of the two quantities and D is the diffusion coefficient.

1.5.1.2. Implicit Scheme

This is the most accurate scheme. The equation (1.26) takes the form

$$\frac{n_{ij}^{k+1} - n_{ij}^k}{\Delta t} + \frac{1}{2} \{ \Psi(n^{k+1}, E^{k+1}, \mu^{k+1}, T^{k+1}) + \Psi(n^k, E^k, \mu^k, T^k) \} = 0 \quad (1.30)$$

In fact, this is a system of strongly nonlinear equations in n^{k+1} since it depends on E^{k+1} which also depends on n^{k+1} . It is absolutely stable for all values of Δt [16]. However, it is too costly to be performed each time step.

1.5.1.3. Semi-Implicit Scheme

This scheme represents a compromise between the other two schemes. It is assumed that

$$E^{k+1} \approx E^k \quad (1.31a)$$

$$\mu^{k+1} \approx \mu^k \quad (1.31b)$$

$$T^{k+1} \approx T^k \quad (1.31c)$$

in the coefficients of Ψ only. Hence, equation (1.26) becomes

$$\frac{n_{ij}^{k+1} - n_{ij}^k}{\Delta t} + \frac{1}{2} \{ \Psi(n^{k+1}, E^k, \mu^k, T^k) + \Psi(n^k, E^k, \mu^k, T^k) \} = 0 \quad (1.32)$$

For this method to be stable, the time increment must be smaller than the dielectric-relaxation time [16], which means

$$\Delta t < \frac{\epsilon}{q N_d \mu_{\max}} \quad (1.33)$$

In this model both the continuity and the energy equations are formulated using the semi-implicit scheme. The solution of equ. (1.32), and the corresponding one for the energy equation, is performed using the successive-over-relaxation method (SOR).

1.5.2. SOLUTION OF POISSON'S EQUATION

The accuracy of the solution and the convergence of the program depends greatly on the accuracy of Poisson's equation solver due to the strong nonlinearity of the equation. Accordingly, it was decided that Poisson's equation has to be solved exactly in this program, despite the fact that many iterative solutions for this particular equation do exist. Hence, a direct and exact method was developed by Ibrahim [14]. It was developed specially for this program. It is called Matrix Double Sweep Method (MDS). The reader is referred to the original author for any further discussion of this MDS method. Some other fast and direct solutions are available as well; for example see [17].

1.6. GENERAL DISCUSSION

This model is already developed. It is phenomenologically correct and numerically stable. A special algorithm exploiting the difference in the dielectric-relaxation time between the active layer and the buffer layer as well as the large difference between the energy relaxation time and the dielectric relaxation time is developed to reduce the execution time [15].

One should notice that the aim of this computer model is to produce a physical insight to the electron transport phenomena inside the device under investigation. Moreover, it is a very powerful tool in studying the two dimensional aspects of the MESFET's such as fringing effects, effect of carrier injection into the substrate, formation of stationary and travelling domains ,... etc. Although the model is capable of accurately predicting the I-V characteristics as well as parameters of the small signal equivalent circuit of the FET and some other unipolar devices, it is not suitable for computer aided design (CAD) use due to the relatively large CPU time required. On the other hand, the amount of information generated by this model is much more than that required for CAD.

The distributions of the carrier concentration, the electric potential and the average electron energy are plotted in contour-lines form. These plots are very helpful and informative for analyzing the device performance. To be acquainted with these plots, we will present one set which shows the state of a MESFET under

normal operation. The simulated device has the same general configuration as that shown in Fig. 1.2(b). The length of each electrode as well as the spacing between them is equal to $0.5\text{ }\mu\text{m}$. The active-layer depth is $0.2\text{ }\mu\text{m}$. It is doped at 10^{17} cm^{-3} . The upper $0.3\text{ }\mu\text{m}$ of the buffer-layer is also included. Fig. 1.3(a) shows the contour plots of the carrier concentration (n/N_D) in steps of 0.1 with N_D equal to 10^{17} cm^{-3} . It shows that the region under the source has a concentration between 9×10^{16} and 10^{17} cm^{-3} . This concentration drops rapidly at the interface between the active and buffer layers until it finally reaches a concentration less than 10^{16} cm^{-3} in the buffer. Starting from the depletion region under the gate, we notice that the concentration gradually increases from $n < 10^{16}\text{ cm}^{-3}$ to $2 \times 10^{16} < n < 3 \times 10^{16}\text{ cm}^{-3}$ in the channel. Then it drops below 10^{16} cm^{-3} in the buffer-layer. An important result is observed here; n does not reach N_D in the channel under the gate. Fig. 1.3(b) shows the equipotential lines inside the MESFET in steps of 0.1 volt each. The high field region under the gate, which represents the field in the depletion region, is clearly shown. It is shown that most of the applied voltage is absorbed in the channel under the gate; the rest of the active layer is in low field for this bias condition. Due to the potential barrier of the N-i junction between the active and buffer layers, this plot shows a line of potential -0.1 volt which means that the region below it is in potential $-0.1 > V > -0.2$ volt. Fig 1.3(c) shows the distribution of the average electron energy in steps of 0.05 eV each. This figure shows that in the region between the source and the gate the average electron energy is less than 0.05 eV. The energy increases gradually until it reaches 0.2 eV in the channel. Near the edges of the gate electrode, there are two high energy regions. The source for these two anomalous regions is the fact that the numerical balance between the drift and diffusion current components at the gate edges is not reached. A numerically very small current exists and it is either flowing to or from the depletion region. This small current is multiplied by the very high field, that results from the singularity at the gate edge, and produces this high energy. However, these anomalies have no effect on the accuracy of this model since they occur in practically depleted regions.

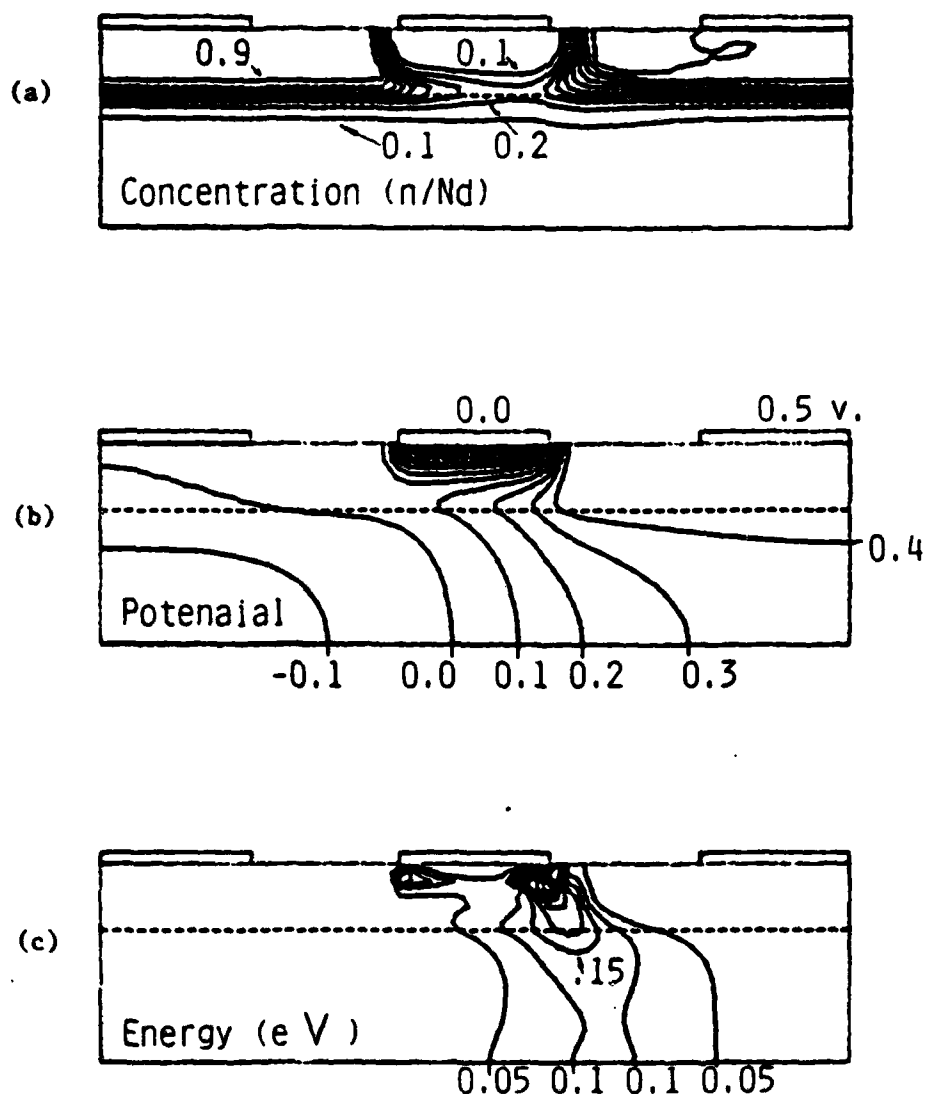


Fig. 1.3. The contour plots of a MESFET at $V_g = 0.0$ V and $V_{ds} = 0.5$ V. (a) The carrier concentration is shown as (n/N_d) in steps of 0.1. (b) The equipotential lines are shown in steps of 0.1 V. (c) The average electron energy is shown in steps of 0.05 eV.

CHAPTER 2.

CARRIER INJECTION REDUCTION USING MESFET'S ON P-SUBSTRATES AND ON THIN P-LAYERS

2.1. INTRODUCTION

GaAs MESFET's are very promising devices to produce both low-noise and power amplification up to the mm-wave range. In general, the MESFET is made of a very thin GaAs active-layer, in the order of a fraction of a micron, epitaxially grown over a Semi-Insulating (SI) GaAs substrate. For such a thin active-layer, a large number of electrons are injected into the SI substrate underneath the active-layer. The carrier injection is enhanced by the fringing fields from the very short gate. The importance of studying the substrate effect can be appreciated by knowing that as high as 40 % of the total current is actually passing through the substrate [18].

Growing the MESFET active-layer directly on the SI substrate does not produce a good quality device due to the crystallographic defects which may deteriorate the carrier mobility in the active-layer. Moreover, the substrate may contain some impurities such as Oxygen or Chromium, or both. This results in the presence of deep levels in the forbidden energy gap of the GaAs material [19]-[21] and leads to the formation of an interfacial-barrier between the active-layer and the substrate [22]-[26]. This interfacial-barrier depletes the lower part of the active-layer which reduces the effective depth of the active-layer and, consequently, the device current. On the other hand, it makes the D.C. characteristics sensitive to the substrate potential. The latter phenomenon is known as Back-Gating [24],[27]. However, the trapping levels have weak effects on the high frequency performance due to its large time constant. Nevertheless, they have a destructive effect on the noise figure due to the generation-recombination noise associated with them [28].

The undesirable effects of the SI substrate can be greatly reduced by introducing a relatively thick, $0.5 \sim 5.0 \mu\text{m}$, epitaxially grown buffer-layer between the active-layer and the SI substrate. This buffer-layer results in higher mobility values in the lower part of the active-layer, in the vicinity of the interface. It was also reported that the interfacial-potential-barrier between the active-layer and the buffer becomes negligible in this case [19],[21].

The aim of this chapter is two fold. The first aim is to extract the effect of the carrier injection into the substrates by studying two types of MESFET's. The first type is a symmetric MESFET in which the carrier injection into the substrate is irrelevant or, simply, which has no substrate effects. The second type is a MESFET fabricated on an ideal buffer-layer. The MESFET with an interfacial barrier will be studied as well. The source of this interfacial barrier may be due to deep trap levels in the GaAs substrate or due to a P-layer intentionally developed right below the active-layer as what will be explained later. The second aim of this chapter is to introduce techniques to reduce the carrier injection into MESFET substrates and to assess their potential as well. Two main techniques are proposed, the MESFET on a P-substrate and the MESFET on a thin P-layer.

2.2. EFFECT OF CARRIER INJECTION

2.2.1. MESFET ON A BUFFER-LAYER

The first device simulated here is a MESFET of $0.5 \mu\text{m}$ gate-length and $0.15 \mu\text{m}$ active-layer thickness. The active-layer is doped at 10^{17}cm^{-3} . It is considered to have mobility equal to $5000 \text{cm}^2/\text{V}.\text{sec}$. at low electron-energy values; but the mobility drops to about $360 \text{cm}^2/\text{V}.\text{sec}$. when the electron-energy equals 0.35eV . This device is fabricated on an ideal buffer-layer doped with shallow donors of density 10^{14}cm^{-3} to account for any residual doping that may exist. The interface between the active-layer and the buffer-layer is considered to be ideal which means that the potential barrier is just equal to the built-in potential of the N-i junction. The upper $0.25 \mu\text{m}$ of this buffer-layer is included as shown in Fig. 2.1.

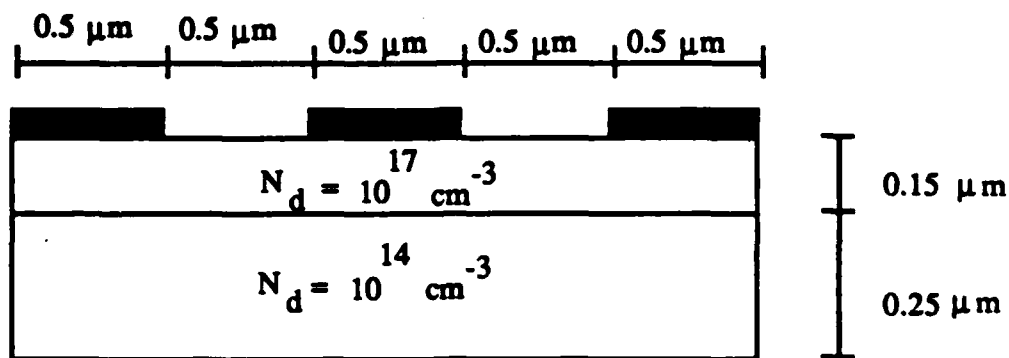


Fig. 2.1. The MESFET on a buffer-layer

The I-V characteristics of this device are shown in Fig. 2.2. There are two interesting features in this characteristics:

- 1- The current does not saturate, but it is continuously increasing with V_{ds} .
- 2- The pinch-off voltage is normally estimated as

$$V_p = V_g + V_{bi} = - \frac{q N_d a^2}{2 \epsilon} = -1.6 \text{ V} \quad (2.1)$$

Where V_p is the voltage which completely depletes the active-layer and V_{bi} , the built-in potential, is taken as -0.8 V . From (2.1), the current is expected to be zero when V_g is less than -0.8 V . However, the device does not follow this equation. In fact, Fig. 2.2 shows that an appreciable current is passing through the device at $V_g = -1.0 \text{ V}$.

The source of these two observations can be understood by examining Fig. 2.3 which shows the state of this device at $V_g = 0.0 \text{ V}$ and $V_{ds} = 5.0 \text{ V}$. It is shown that large number of carriers are injected into the buffer-layer. This carrier injection increases when the drain bias is increased. This is the reason for the continuous rise in the current with the drain bias. On the other hand, the contribution of the current passing through the buffer-layer to the total device

current cannot be ignored since the buffer-layer has a substantial free carrier density, as shown in Fig. 2.3(a). Fig. 2.4 shows the percentage of the current passing through the buffer-layer to the total device current. It is shown that the role of the buffer-layer current becomes more and more important as the device approaches the pinch-off. When the active-layer is completely depleted (i.e. for $V_g < -0.8$ V), the total device current is actually passing through the buffer-layer. This explains the second observation mentioned before.

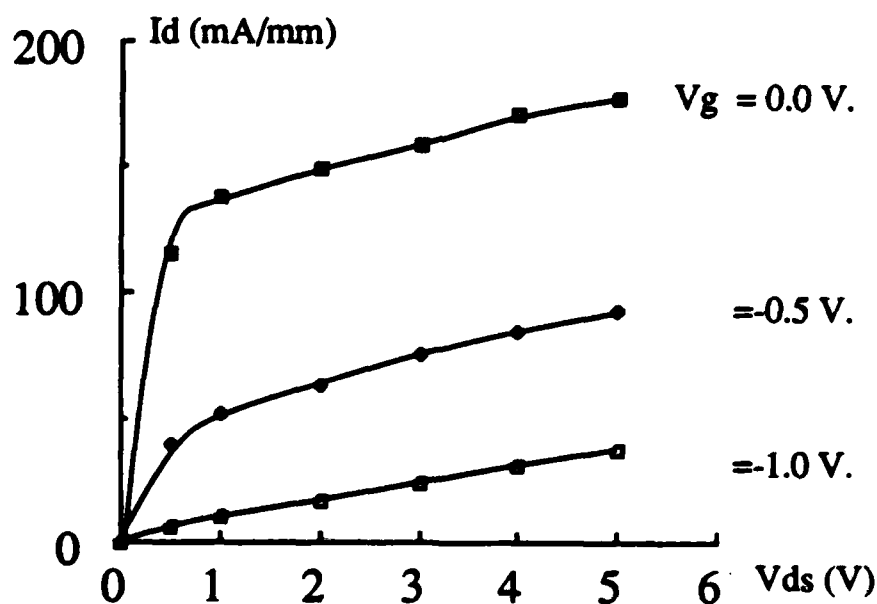


Fig. 2.2. The I-V characteristics of the MESFET on a buffer-layer.

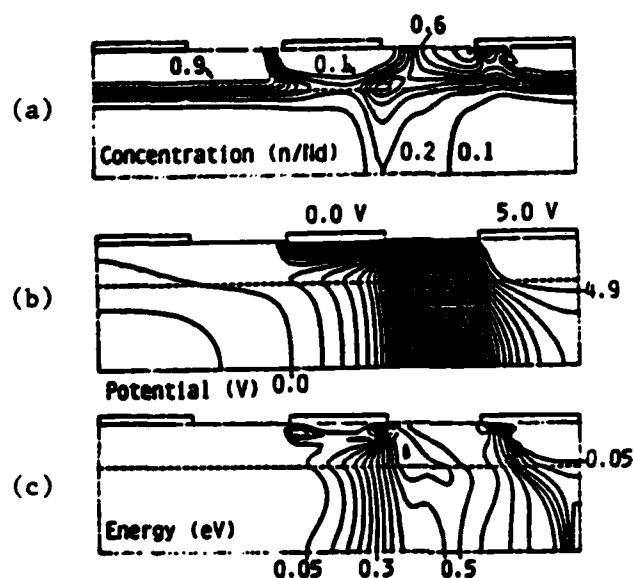


Fig. 2.3. The contour plots of the MESFET on a buffer-layer at $V_g = 0.0$ V and $V_{ds} = 5.0$ V. (a) The carrier concentration (n/N_d) is shown in steps of 0.1. (b) The equipotential lines are shown in steps of 0.1 volt. (c) The average electron energy is shown in steps of 0.05 eV.

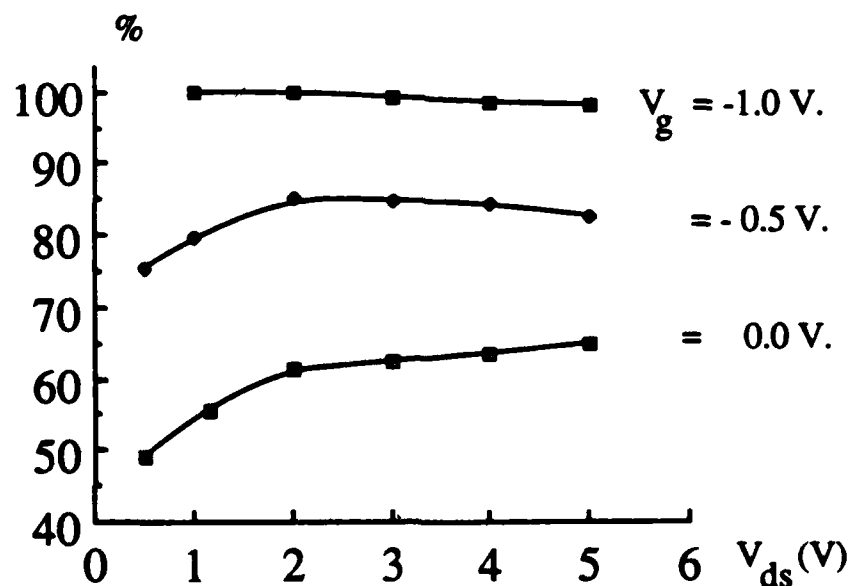


Fig. 2.4. Percentage of the current passing through the buffer-layer to the total device current.

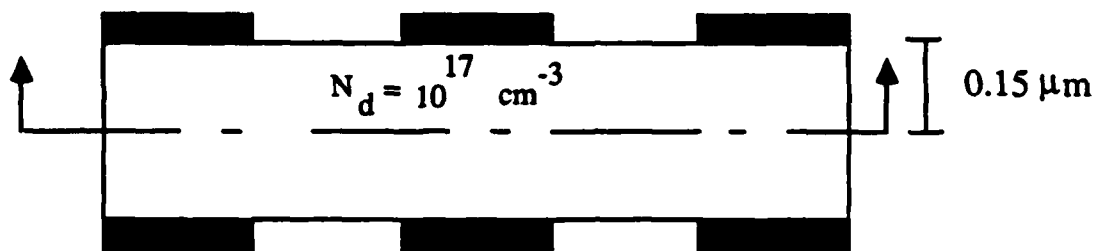


Fig. 2.5. The symmetrical MESFET. One half of it is the substrate-less MESFET.

2.2.2. SUBSTRATE-LESS MESFET

In order to correctly extract the effect of the carrier injection into the buffer-layer, a MESFET which has no substrate, that is a substrate-less device, is simulated. A substrate-less device means a transistor in which the carriers are confined to the active-layer. This situation physically corresponds to the symmetrical MESFET shown in Fig. 2.5. In this study, only the upper half of this structure will be considered. This substrate-less MESFET is simulated using the same dimensions and parameters as the active-layer of the MESFET on a buffer-layer. The I-V characteristics of this substrate-less MESFET are shown in Fig. 2.6. The main features of these characteristics, compared to those of the MESFET on a buffer-layer shown in Fig. 2.2, are:

- 1- The current in the saturation region demonstrates less dependence on the drain voltage.
- 2- The device reaches pinch-off at the gate-voltage predicted by equ.(2.1).
- 3- For the same bias condition, the substrate-less device produces a smaller current.

It is interesting to observe that although the current of the substrate-less device is less than that of the MESFET on a buffer-layer, the difference in the current does not exactly correspond to the current passing through the buffer-layer in the later device, especially for the open channel case. For example, consider the case when $V_g = 0.0$ and $V_{ds} = 5.0$ V. The substrate-less MESFET produces a current of 140.6 mA/mm while the MESFET on a buffer-layer produces 177.6 mA/mm and

its buffer-layer current is 115.1 mA/mm. The reason for this phenomenon can be understood by examining Fig. 2.7, which shows the state of the substrate-less MESFET at this bias condition, and comparing it with Fig. 2.3. Fig. 2.7(a) shows that the lowest carrier concentration in the channel $0.4 < n/N_d < 0.5$ while Fig. 2.3 shows that $0.2 < n/N_d < 0.3$. Hence, it can be seen that the substrate-less MESFET has a smaller effective-channel depth but with a relatively high carrier concentration. Furthermore, both the MESFET on a buffer-layer and the substrate-less MESFET exhibit a stationary Gunn domain formation in the saturated-channel region, as shown in Fig's 2.3 and 2.7 respectively. Nevertheless, the maximum carrier concentration inside the domain is less than $0.7 \times 10^{17} \text{ cm}^{-3}$ (i.e. less than N_d) for the MESFET on a buffer-layer, while it exceeds $1.2 \times 10^{17} \text{ cm}^{-3}$ for the substrate-less MESFET. Obviously, this is due to the carrier diffusion to the buffer-layer in the former case.

2.2.3. MESFET WITH AN INTERFACIAL-BARRIER

The third device simulated here is the MESFET with an interfacial-barrier. The interfacial-barrier is simulated by replacing the buffer-layer of the MESFET shown in Fig. 2.1 by another layer of GaAs material which has an acceptor concentration of 10^{16} cm^{-3} . The origin of this interfacial-barrier can be interpreted in different ways; it may result from unavoidable deep traps inside the substrate, or from an intentionally Chromium doped layer under the active-layer, or a combination of both as well. The active-layer has the same parameters and dimensions as the device fabricated on a buffer-layer. The I-V characteristics of this device are shown in Fig. 2.8. It is observed that this MESFET has the smallest output current compared to the other two devices. This reduction in the current can be attributed to the partial depletion of the lower part of the active-layer due to the potential barrier. This figure also shows that this MESFET almost reaches pinch-off at $V_g = -0.5 \text{ V}$. The effective active-layer thickness can be derived from (2.1) as

$$a_{\text{eff}} = \sqrt{\frac{-2\epsilon(V_g + V_{bi})}{qN_d}} = 0.135 \quad (2.2)$$

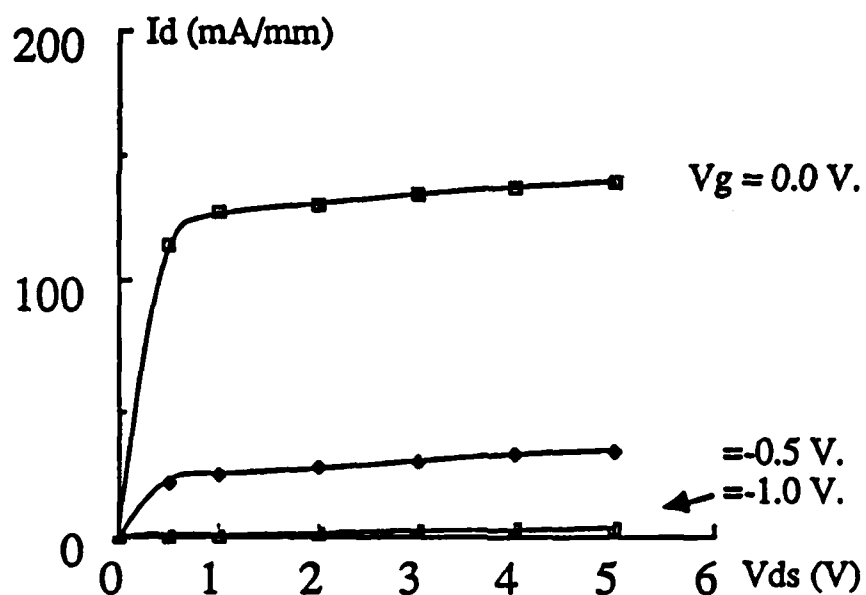


Fig. 2.6. The I-V characteristics of the substrate-less MESFET.

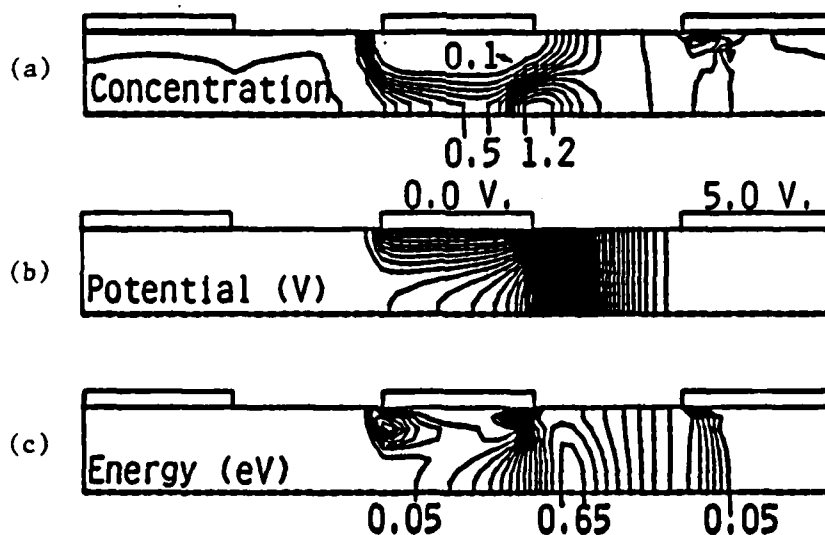


Fig. 2.7. The contour plots of the substrate-less MESFET at $V_g = 0.0$ V and $V_{ds} = 5.0$ V. (a) The carrier concentration (n/N_d) is shown in steps of 0.1. (b) The equipotential lines are shown in steps of 0.1 volt. (c) The average electron energy is shown in steps of 0.05 eV.

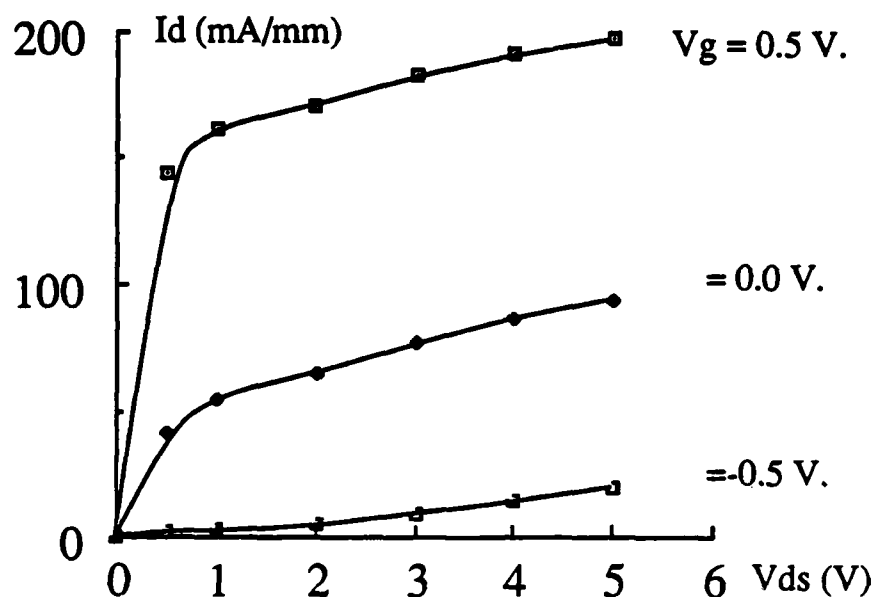


Fig. 2.8. The I-V characteristics of the MESFET with an interfacial barrier.

If one desires to compensate for the reduction in the active-layer thickness, a positive bias has to be applied to the gate.

The contour plots for this device at $V_g = 0.0$ V and $V_{ds} = 5.0$ V are shown in Fig. 2.9. The main features that can be deduced from this figure are:

- 1- The free carrier contour lines, in Fig. 2.9(a), are displaced upwards which indicates the partial depletion of the lower part of the active-layer.
- 2- The height of the potential barrier is about 0.5 V. This is clearly shown in Fig. 2.9(b) in the region right under the source.
- 3- There is a stationary domain formed at the gate exit. The highest carrier concentration inside this domain does not exceed $0.5 \times 10^{17} \text{ cm}^{-3}$.
- 4- The carrier injection from the active-layer is greatly reduced due to the potential barrier. Nevertheless, the stationary domain managed to inject some carriers since its transverse electric field could reduce the potential barrier underneath the domain.

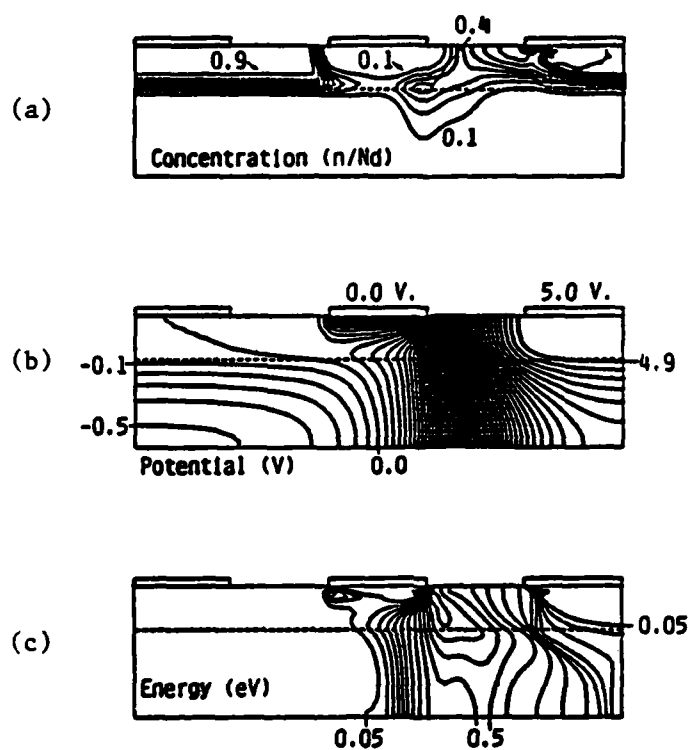


Fig. 2.9. The contour plots of the MESFET with an interfacial barrier at $V_g = 0.0$ V and $V_{ds} = 5.0$ V. (a) The carrier concentration (n/N_d) is shown in steps of 0.1. (b) The equipotential lines are shown in steps of 0.1 volt. (c) The average electron energy is shown in steps of 0.05 eV.

2.2.4. COMPARISON OF THE CHARACTERISTICS

In order to assess the potential of each one of the three MESFET's presented here, a complete comparison between the main parameters will be presented. First, a comparison of their typical I-V characteristics is given in Fig. 2.10, which describes the currents at $V_g = 0.0$ V. It is shown that the highest current can be obtained from the MESFET fabricated on a buffer-layer, and the lowest current results from the MESFET with an interfacial barrier due to the reduction of its active-layer thickness. This suggests that the characteristics of these devices cannot be compared under the same external bias condition. This is because the channel widths are different for the same external gate bias. When examining the small signal equivalent circuit, we compare the parameters of the MESFET on a buffer-layer or those of the substrate-less MESFET at $V_g = 0.0$ volt against those of the MESFET with an interfacial barrier at $V_g = 0.5$ V. In what follows, this 0.5 voltage offset is added in order to compare devices with about the same channel width.

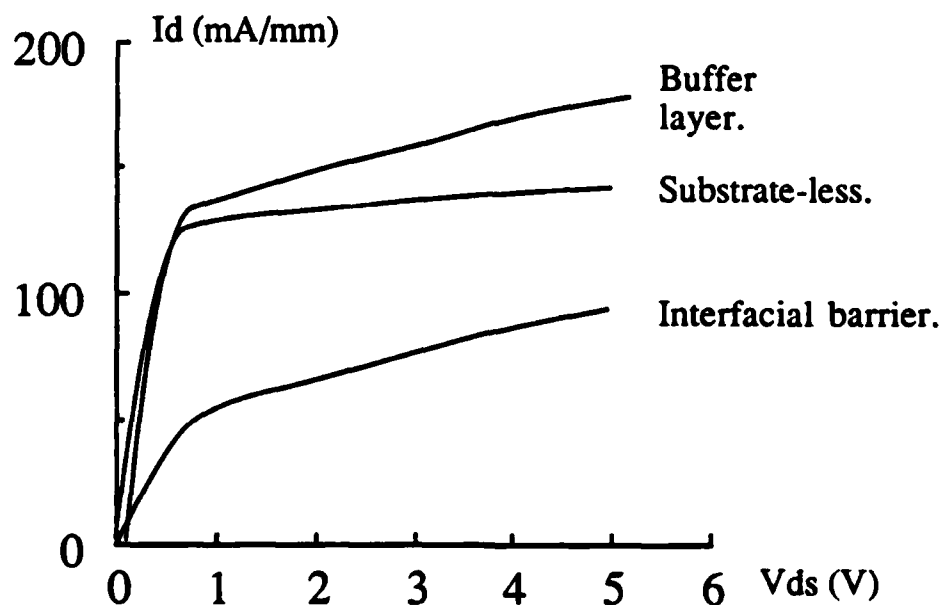


Fig. 2.10. The I-V characteristics of the three MESFET's at $V_g = 0.0$ V.

The transconductances (g_m) of the three devices, as function of V_{ds} and with V_g as a parameter, are given in Fig. 2.11. It is shown that the MESFET with an interfacial barrier and the substrate-less MESFET supersede the MESFET on a buffer-layer for the open channel case. By closing the channel, the MESFET on a buffer-layer produces a better g_m . Obviously, this is due to the large dynamic range of this device. The gate-to-source capacitances (C_{gs}) of the three devices are shown in Fig. 2.12. By comparing devices at equal channel widths, it is easily seen that the MESFET with an interfacial barrier has the highest C_{gs} . This can be understood by knowing that for the same channel width, this MESFET has a smaller depletion region compared to the other two devices which directly means larger C_{gs} . On the other hand, the MESFET on a buffer-layer and the substrate-less device produce about the same C_{gs} at $V_g = -0.25$ V, but the latter device produces the lowest C_{gs} at $V_g = -0.75$ V.

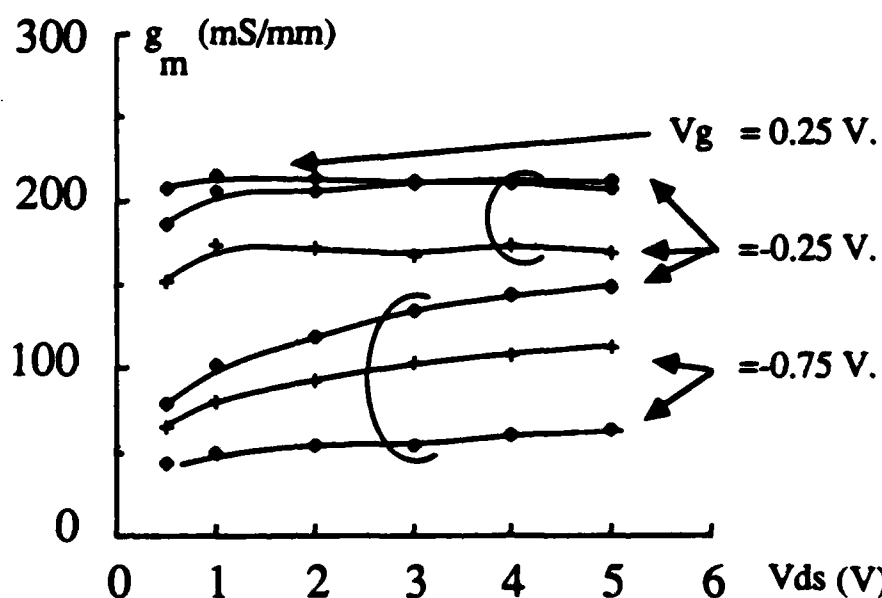


Fig. 2.11. The transconductance of three devices. "+++" The MESFET on buffer-layer. "•••" The substrate-less MESFET. "xxx" The MESFET with an interfacial barrier.

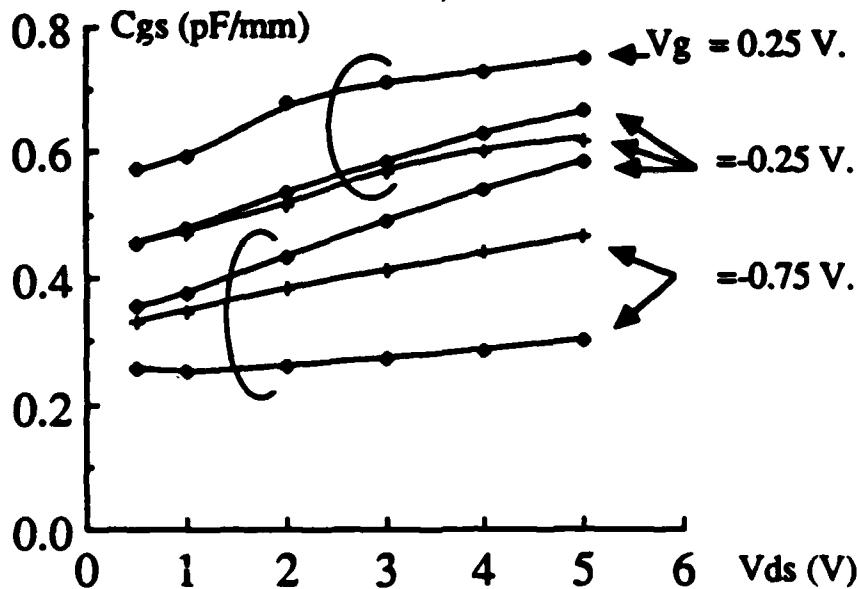


Fig. 2.12. The gate-to-source capacitance of three devices. "—" The MESFET on buffer-layer. "x—" The substrate-less MESFET. "o—" The MESFET with an interfacial barrier.

The current-gain cutoff frequency defined as

$$f_t = \frac{g_m}{2\pi C_{gs}} \quad (2.3)$$

is given in Fig. 2.13. It is shown that the substrate-less device has the highest f_t for an open channel. It is interesting to observe that the f_t curves of the MESFET with an interfacial barrier lay between the curves of the other two devices.

The drain conductances (g_d) of the three devices are shown in Fig. 2.14. It is shown that at any bias condition, the MESFET on a buffer-layer has the highest g_d and the substrate-less device has the lowest one. This clearly proves that the carrier injection into the buffer-layer, or the substrates in general, directly leads to higher drain conductance. This explains the case of the MESFET with an interfacial barrier which produces an intermediate g_d curves since its carriers are not perfectly confined to the active-layer as the substrate-less MESFET, but it has a better confinement compared to the MESFET on a buffer-layer.

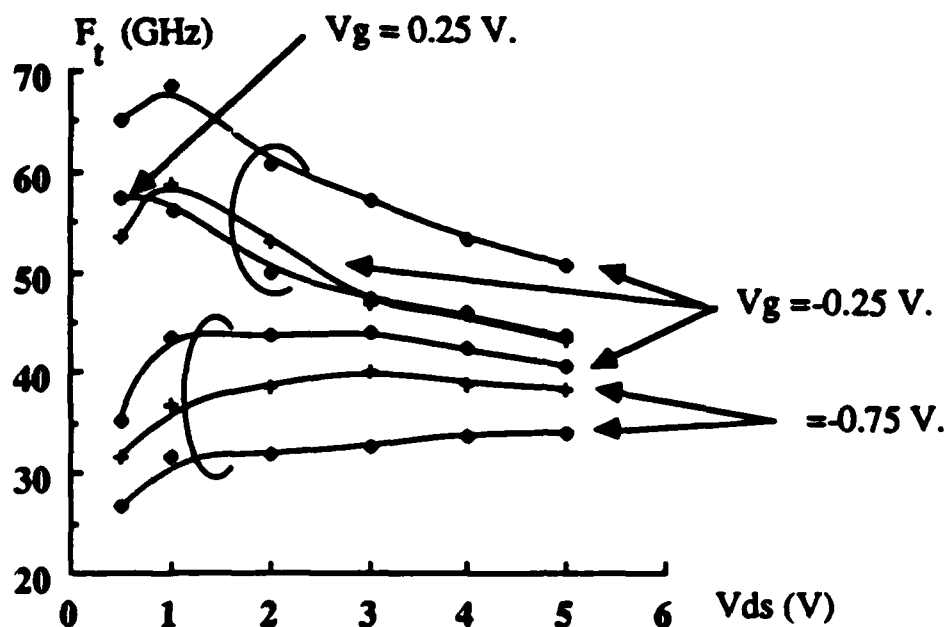


Fig. 2.13. The current-gain cutoff frequency of three devices. "—+"— The MESFET on buffer-layer. "—♦—" The substrate-less MESFET. "—x—" The MESFET with an interfacial barrier.

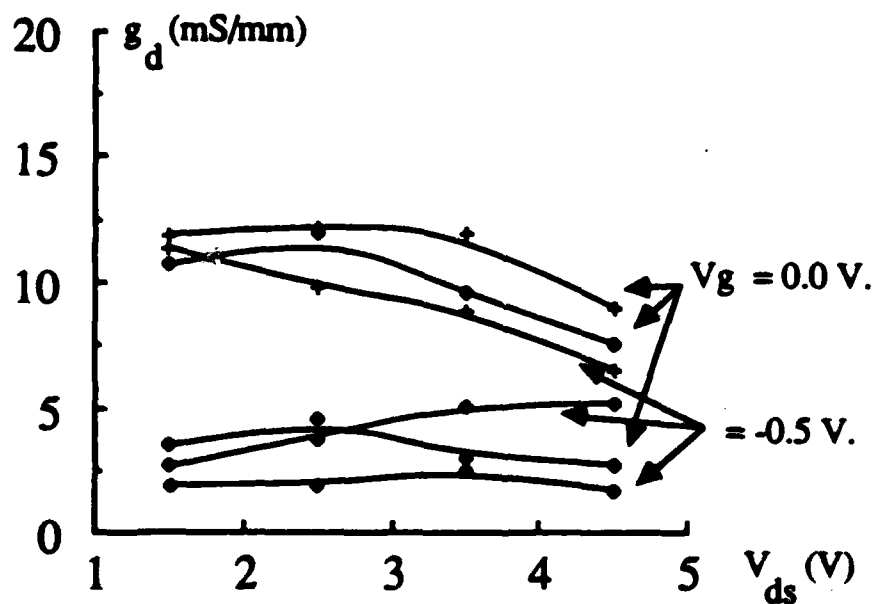


Fig. 2.14. The drain conductance of three devices. "—+"— The MESFET on buffer-layer. "—♦—" The substrate-less MESFET. "—x—" The MESFET with an interfacial barrier.

2.3. MESFET ON A P-SUBSTRATE

It was previously shown that the MESFET performance is improved by confining the carriers into the active-layer. The best carrier confinement was achieved using the symmetrical FET. Unfortunately, it is not easy to realize this structure in the mm-wave range. It was also shown that introducing a potential barrier between the active-layer and the substrate provides some carrier confinement and, therefore, it improves the performance. The simplest way to achieve this is to fabricate the N-active-layer of the MESFET on a P-substrate such that the built-in potential-barrier of the created P-N junction is used to confine the electrons to the active-layer [18], [29]. This approach is considered as a compromise between the normal MESFET on SI buffer-layer and the symmetrical MESFET. In this approach, the potential barrier is determined by the junction properties. It is, more or less, fixed once the dopings and the temperature are determined. In this section, we will investigate the effect of changing the doping of the P-substrate on the characteristics of the N-channel-submicron-gate MESFET.

Throughout this section, the basic MESFET structure, similar to that in Fig. 2.1, is simulated. The electrodes dimensions are always the same as shown in the figure. However, the active-layer thickness is equal to $0.125\text{ }\mu\text{m}$ and it is doped at $2 \times 10^{17}\text{ cm}^{-3}$ to ensure reasonable output current. In order to account for the higher doping in the active-layer, the selected mobility curve has a maximum mobility equal to $4000\text{ cm}^2/\text{V}\cdot\text{sec}$. Three different acceptor concentrations in the substrates are simulated, $N_{a1} = 10^{16}\text{ cm}^{-3}$, $N_{a2} = 2.5 \times 10^{16}\text{ cm}^{-3}$, and $N_{a3} = 5 \times 10^{16}\text{ cm}^{-3}$. The depth of the simulated part of the P-substrate is chosen such that it creates a potential-barrier exactly equal to that of the corresponding P-N junction in each case.

The contour plots of the MESFET which has a substrate doping $N_a = 10^{16}\text{ cm}^{-3}$ is shown in Fig. 2.15, at $V_g = 0.0\text{ V}$ and $V_{ds} = 5.0\text{ V}$. A slight depletion of the lower part of the active-layer is observed. Moreover, comparing this figure with those of MESFET on buffer-layer, e.g. as in Fig. 2.3, a great reduction of the carrier injection from the active-layer is also observed, though Fig. 2.15 has twice the doping and supposed to inject more carriers in normal cases. This shows the effectiveness of the potential-barrier. In Fig. 2.15, a stationary domain is formed under the gate end on the drain side of the gate. This domain creates a transverse

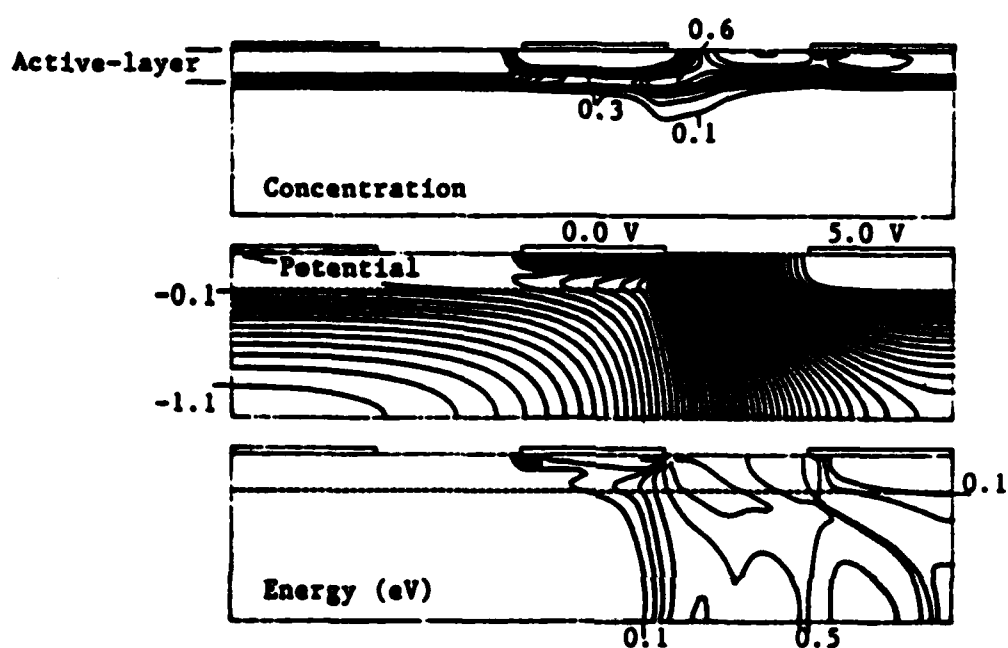


Fig. 2.15. The contour plots of the MESFET on a P-substrate, $N_a = 10^{16} \text{ cm}^{-3}$. (a) The carrier concentration (n/N_d) shown in steps of 0.1. (b) The equipotential lines shown in steps of 0.1 V. (c) The average electron energy shown in steps of 0.1 eV.

field that lowers the potential barrier. Therefore, a considerable carrier injection is observed under this domain. The carriers are pushed back to the active-layer immediately after the end of this domain. By increasing the doping level of the substrate, more depletion in the active-layer is observed.

The I-V characteristics of these three devices are shown in Fig. 2.16, set A, at $V_g = 0.0$ V. It is observed that the drain current is drastically reduced by increasing the concentration of the acceptor atoms in the substrate. This current reduction is a direct effect of the active-layer depletion. It also means that the device dynamic range is reduced by increasing the substrate doping. However, apart from the other improvements introduced by this P-substrate, the reduction of the device dynamic range is unfavorable for some applications. Therefore, it can be considered as a disadvantage of using high doping in the P-substrate. On the other hand, the height of the potential barrier can be estimated from the basic P-N junction law

$$V_{bi} = \frac{k_B T}{q} \ln \left(\frac{N_d N_a}{n_i^2} \right) \quad (2.4)$$

where k_B is the Boltzmann constant, T is the temperature in °K, q is the electronic charge, N_d and N_a are the dopings at the two sides of the junction, and n_i is the intrinsic carrier pair density. At room-temperature, the potential barrier changes from 1.22 V to 1.27 V when N_a is changed from 10^{16} cm^{-3} to $5 \times 10^{16} \text{ cm}^{-3}$ respectively. The difference between the potential-barriers created by these two dopings is practically negligible; but the amount of depletion produced at the bottom of the active-layer and the drain current reduction is substantial. Accordingly, high acceptor concentrations in the substrate are not recommended.

2.4. MESFET ON A THIN P-LAYER

It should be noted that the electrons can be confined into the active-layer using a much smaller potential-barrier than that created by the P-N junction. This suggests that introducing a thin P-layer between the MESFET active-layer and the semi-insulating substrate can be very beneficial if the thickness of this layer is chosen so small that the P-layer becomes fully depleted. In this case, the height of the potential barrier and the active-layer depletion can be controlled by changing the depth of the P-

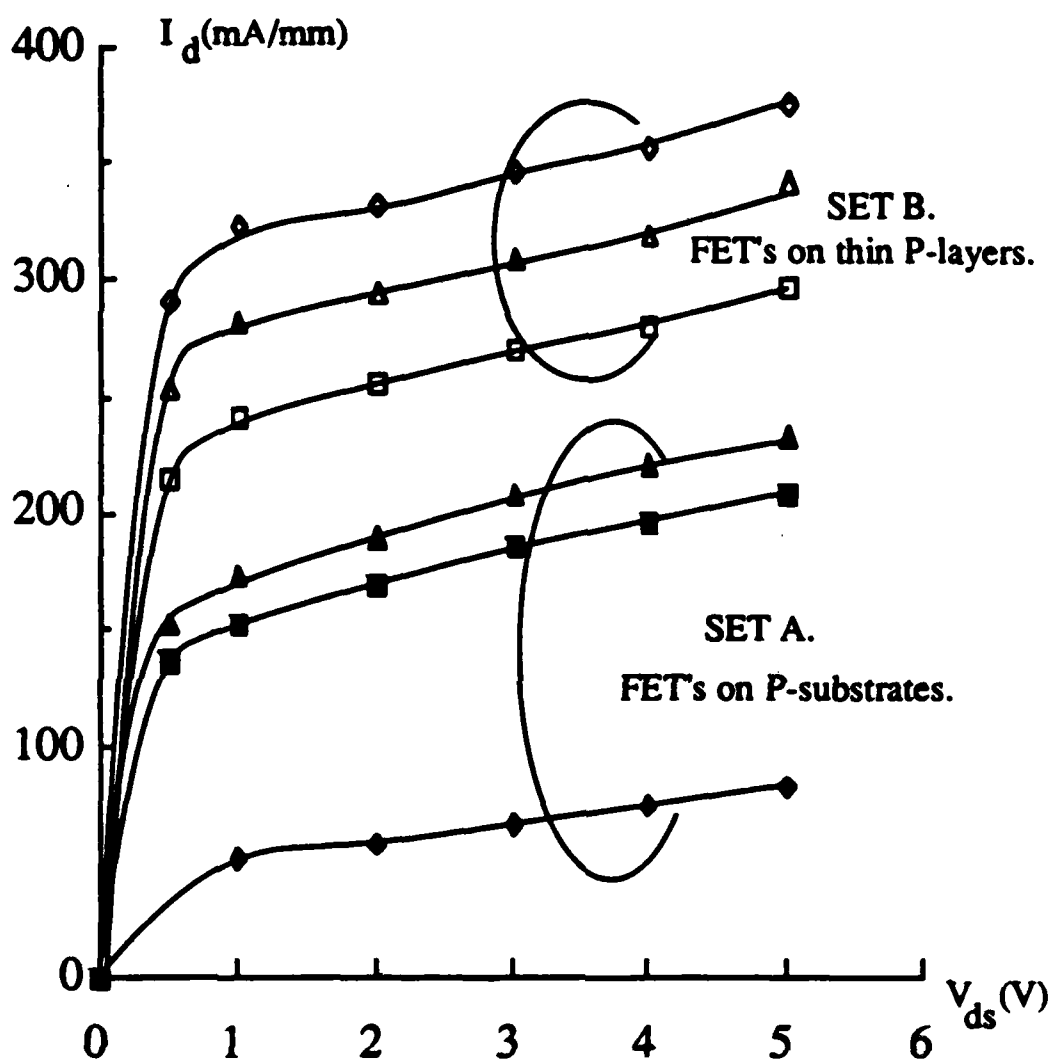


Fig. 2.16. The I-V characteristics of all the MESFET's at $V_g = 0.0$ V. SET A, MESFET's on P-Substrates with "◆" $N_d = 5 \times 10^{16}$, "■" $N_d = 2.5 \times 10^{16}$ and "▲" $N_d = 10^{16}$ cm⁻³. SET B, MESFET's on thin P-layers with "◻" $N_d = 1.5 \times 10^{16}$, "▲" $N_d = 10^{16}$ and "◇" $N_d = 5 \times 10^{15}$ cm⁻³.

layer or its doping or both. This produces a flexible MESFET structure from the potential-barrier point of view. Enoki et al. [30] tried this approach in what so called Advanced SAINT FET. It was reported that this approach resulted in a high transconductance, 240 mS/mm.

To examine the effectiveness of the thin P-layer approach, three MESFET structures are simulated. All of them have the same active-layer parameters as the previous MESFET on a P-substrate.

The relation between the simulated thickness of the P-layer and the resulting potential barrier can be obtained analytically by integrating Poisson's equation at the interface and using the full-depletion approximation

$$V_{pb} = \frac{q N_a y_p^2}{2 \epsilon} \left(1 + \frac{N_a}{N_d} \right) \quad (2.5)$$

where V_{pb} is the resulting potential barrier and y_p is the simulated depth of the P-layer. y_p is chosen such that dopings of $5 \times 10^{15} \text{ cm}^{-3}$, 10^{16} cm^{-3} , and $1.5 \times 10^{16} \text{ cm}^{-3}$ result in a maximum potential barrier of 0.3 V, 0.55 V, and 0.9 V respectively.

The contour plots for the case of $N_a = 10^{16} \text{ cm}^{-3}$, and at $V_g = 0.0 \text{ V}$ and $V_{ds} = 5.0 \text{ V}$, are shown in Fig. 2.17. It is observed that there is a smaller depletion in the active-layer compared to Fig. 2.15. The stationary domain extends slightly more inside the P-layer. Moreover, the carrier concentration in the channel under the gate is $0.4 < n/N_d < 0.5$ while it is $0.3 < n/N_d < 0.4$ in the MESFET on a P-substrate. The I-V characteristics of the three MESFET's are shown in Fig. 2.16, set B. The drain current shows a dramatic increase compared to the MESFET on a P-substrate. In the $N_a = 10^{16} \text{ cm}^{-3}$ case, the device on a thin P-layer shows a current increase of about 98 mA/mm over the corresponding device on a P-substrate.

A brief comparison of the main small-signal parameters is given in Table 2.1. Before speculating on the behavior of these parameters, one should notice that increasing the potential barrier between the active-layer and the substrate results in two counter balancing effects simultaneously. First, it increases the carriers confinement to the active-layer. Therefore, higher transconductance and lower drain conductance are expected. Second, it reduces the dynamic range of the device which

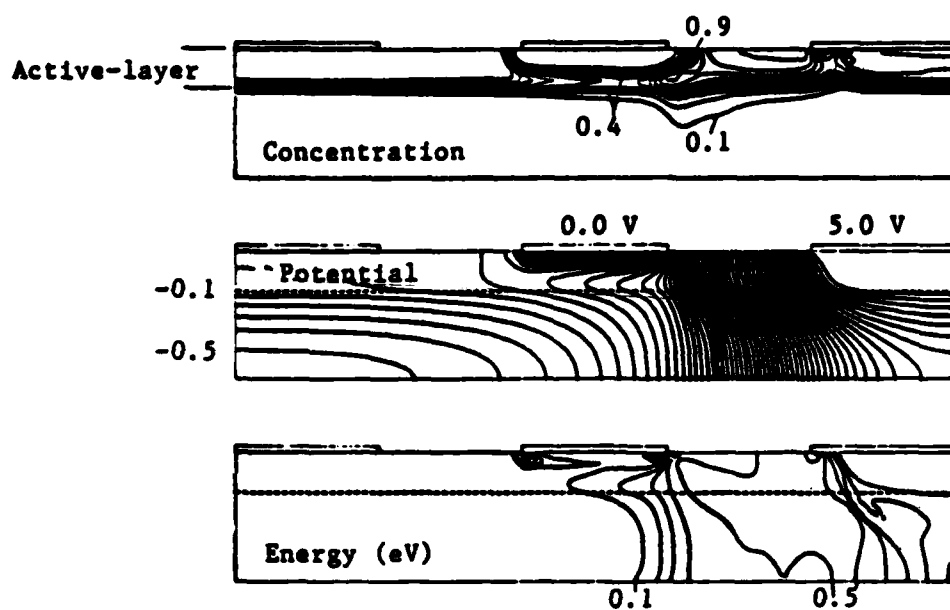


Fig. 2.17. The contour plots of the MESFET on a thin P-layer, $N_A = 10^{16} \text{ cm}^{-3}$. For more explanation see captions of Fig. 2.15.

means that the MESFET becomes closer to the pinch-off. Hence, lower transconductance is expected. The drain conductance increases since the device approaches the space-charge limited current mode.

	N_d cm^{-3}	V_{pb} volt	I_d mA/mm	g_m mS/mm	C_{gs} pF/mm	g_d mS/mm	f_t GHz
MESFET on P-Substrate.	10^{16}	1.23	221	229.8	0.79	18	46.3
	2.5×10^{16}	1.25	197	232.5	0.785	16	47.1
	5×10^{16}	1.27	74.5	207	0.67	9	49.2
MESFET on Thin P-Layer.	5×10^{15}	0.3	356	206	0.80	14	41.0
	10^{16}	0.55	319.5	221	0.81	14	43.4
	1.5×10^{16}	0.9	280	228.5	0.81	13	44.9

Table 2.1. Summary of the MESFET parameters at $V_{ds} = 4.0$ V. V_{b1} is the potential-barrier. I_d is the drain current at $V_g = 0.0$ V. The small-signal parameters, g_m , C_{gs} , g_d and f_t are given at $V_g = -0.25$ V.

CHAPTER 3.

TRAVELING GUNN DOMAINS IN GAAS MESFET'S

3.1. INTRODUCTION

The complexity and the non-linear aspects of the physical phenomena involved in the electron transport inside submicron-gate MESFET's resulted in controversy about some fundamental effects that influence the device performance to a great extent. Consider, for example, the formation of traveling Gunn domains inside the MESFET; this effect has been investigated both theoretically and experimentally. Engelmann *et al.* [31] investigated this phenomenon experimentally and confirmed the formation of the traveling Gunn domains. Yamaguchi *et al.* [3] used a two dimensional computer model and reported the domain formation in a MESFET of 1 μm gate length. They developed criteria for the domain formation based on the channel thickness and doping. Fjeldly *et al.* [32] developed another analytical relation to study the domain formation possibility as a function of the bias condition. An analytical model for the stationary domain in GaAs MESFET was developed as well [33]. Nevertheless, the formation of the traveling domain inside the submicron-gate GaAs MESFET's is still controversial since all these models are based on quasi-static velocity field relations which are not valid for this problem as already explained.

In this chapter, the traveling Gunn domain phenomenon in the submicron-gate MESFET is studied using the previously presented computer model. The time history of the domain is thoroughly investigated. The criteria for the domain formation and stabilization is discussed as well. It is tested by simulating a stable transistor which is free from traveling domains

3.2. TRAVELING GUNN DOMAIN INSIDE THE MESFET

A MESFET with a gate length equal to $0.5\ \mu\text{m}$ and an active layer thickness of $0.2\ \mu\text{m}$ is simulated. The top $0.3\ \mu\text{m}$ of the buffer layer is also included as shown in Fig. 3.1. The doping of the active layer is 10^{17} cm^{-3} . The buffer layer is considered to have a doping of 10^{14} cm^{-3} to account for the imperfect compensation. The maximum electron mobility is taken as $5000\text{ cm}^2/\text{V sec.}$ in the active layer as well as in the buffer. The built-in potential of the Schottky junction is 0.8 volt . This device is biased by applying 0 volt to the gate and 2 volts to the drain at $t=0$. The initial state was 0 volt on the gate and on the drain as well.

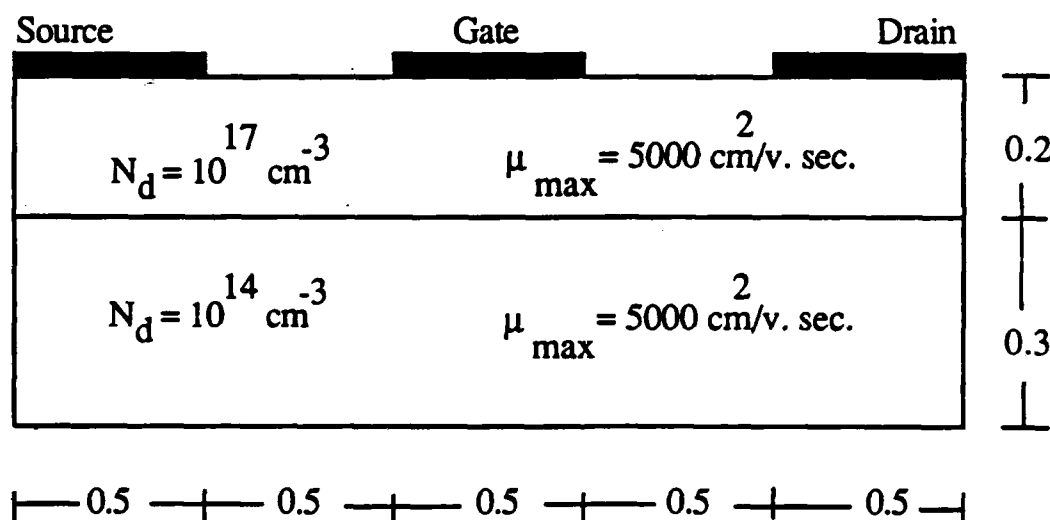


Fig. 3.1. The simulated MESFET. The dimensions are in microns.

Figures 2-8 show the device history during the first 10 ps after the application of the voltage pulse to the drain. Fig. 3.2 shows the device state at $t = 0.5\text{ ps}$. The nucleating domain under the gate exit is clearly shown in this figure. While it is growing, the domain gains area at the expense of the depletion region and the buffer-layer. Fig. 3.2(b) shows that the domain is associated with a

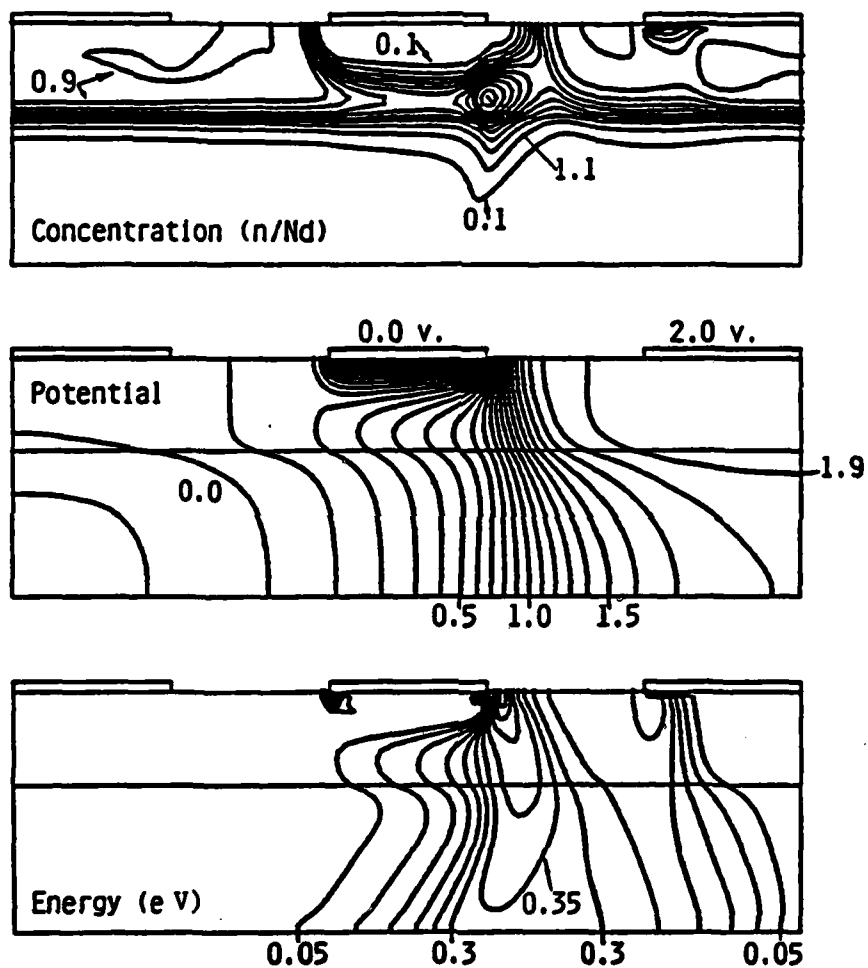


Fig. 3.2. The contour plots of the simulated MESFET at $t = 0.5$ ps, $V_g = 0.0$ and $V_{ds} = 2.0$ volts. (a) The carrier concentration (n/N_d) is shown in steps of 0.1. (b) The equipotential lines are shown in steps of 0.1 volt. (c) The average electron energy is shown in steps of 0.05 eV.

MICROWAVE LABORATORY REPORT NO. 88-P-2

ANALYSIS AND IMPROVEMENT OF MM-WAVE GaAs MESFET'S

TECHNICAL REPORT

SAMIR M. EL-AZHARY EL-GHAZALY

and

Tatsuo Itoh

MAY 1988

ARMY RESEARCH OFFICE

CONTRACT DAAG 29-84-K-0076

UNIVERSITY OF TEXAS

DEPARTMENT OF ELECTRICAL ENGINEERING

AUSTIN, TEXAS 78712

APPROVED FOR PUBLIC RELEASE

DISTRIBUTION UNLIMITED

high field region, this is the reason for being called high field domain sometimes. Moreover, it is preceded by a relatively high energy region as shown in Fig. 3.2(c). However, the point of the highest concentration slightly precedes the points of highest energy and highest field as one moves from the source towards the drain. Fig. 3.3 shows the device state at $t = 2.0$ ps when the domain accumulated large amount of charge, $n_{\max} > 1.3 N_d$, and injected more carriers into the buffer layer. It also gained more electric field demonstrated by the large number of equipotential lines associated to it as shown in Fig. 3.3(b). Moreover, the energy inside the domain exceeds 0.5 eV as shown in Fig. 3.3(c). The device state at $t = 3.0$ ps is presented in Fig. 3.4. This figure will be used later to estimate the oscillation period of the domain. In Fig. 3.5, which shows the device state at $t = 4.0$ ps, the domain becomes mature. The carrier concentration exceeds $1.4 N_d$ in the accumulation region and drops below $0.6 N_d$ in the depletion region. This figure also shows that the domain has travelled an appreciable distance away from the gate. The high field region associated to it becomes well defined as shown in Fig. 3.5(b). No major change is observed in the average energy, $0.5 < \epsilon_{\max} < 0.55$ eV. The high energy region is moving with the domain as one may expect. The domain status while discharging, at $t = 5.5$ ps, is shown in Fig. 3.6. It is shown that the domain depletion region travels a noticeable distance under the drain electrode and so does the high energy region. However, the high electric field is shown to be short circuited due to the boundary condition on the drain (i.e. zero tangential field). Fig. 3.7 is a specially important one since it simultaneously shows the discharge of the old domain as well as the formation of the new domain under the gate, at $t = 7.0$ ps. The mechanism leading to the new domain formation is summarized in Fig. 3.7(b) which shows that after the discharge of the old domain, the electric field in the channel under the gate starts to increase and so does the average energy. This energy increase leads to the negative differential mobility state and thus the carrier accumulation starts and the whole process is repeated again. Fig. 3.8 shows the new domain after becoming mature, at $t = 10$ ps, and starts to travel towards the drain. This figure proves that the traveling domain formation is not just an initialization problem but it is an

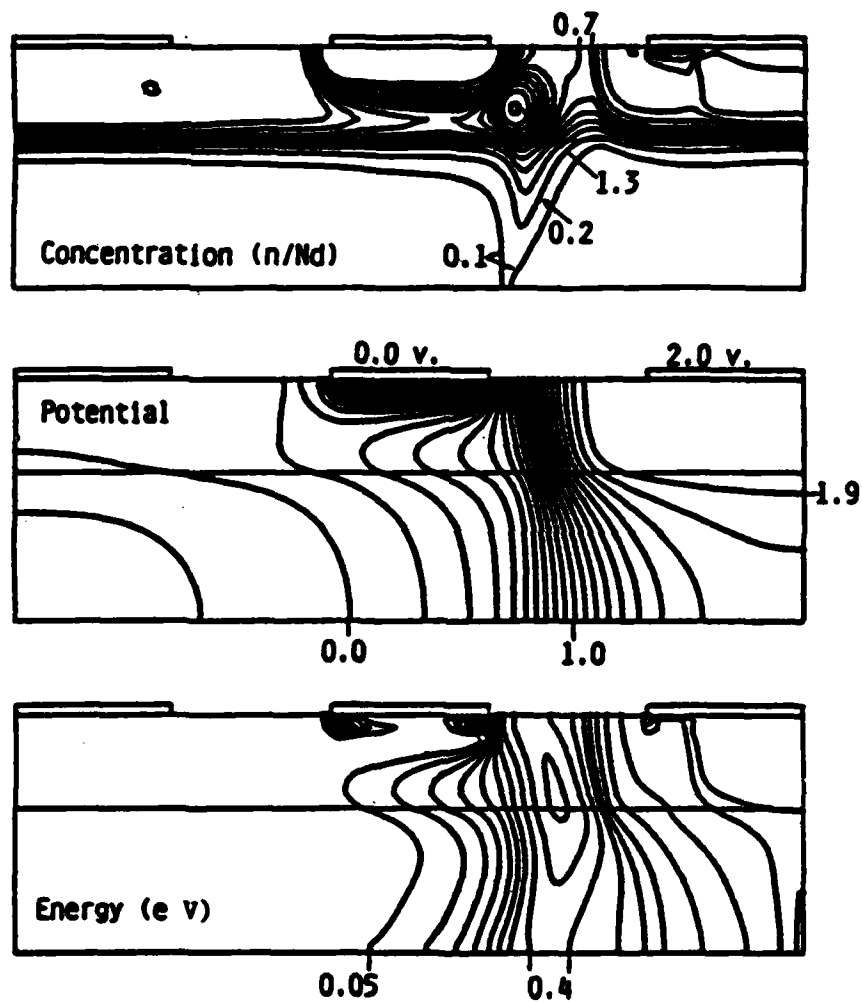


Fig. 3.3. The contour plots of the simulated MESFET at $t = 2.0$ ps, $V_g = 0.0$ and $V_{ds} = 2.0$ volts. For more details, see captions of Fig. 2.

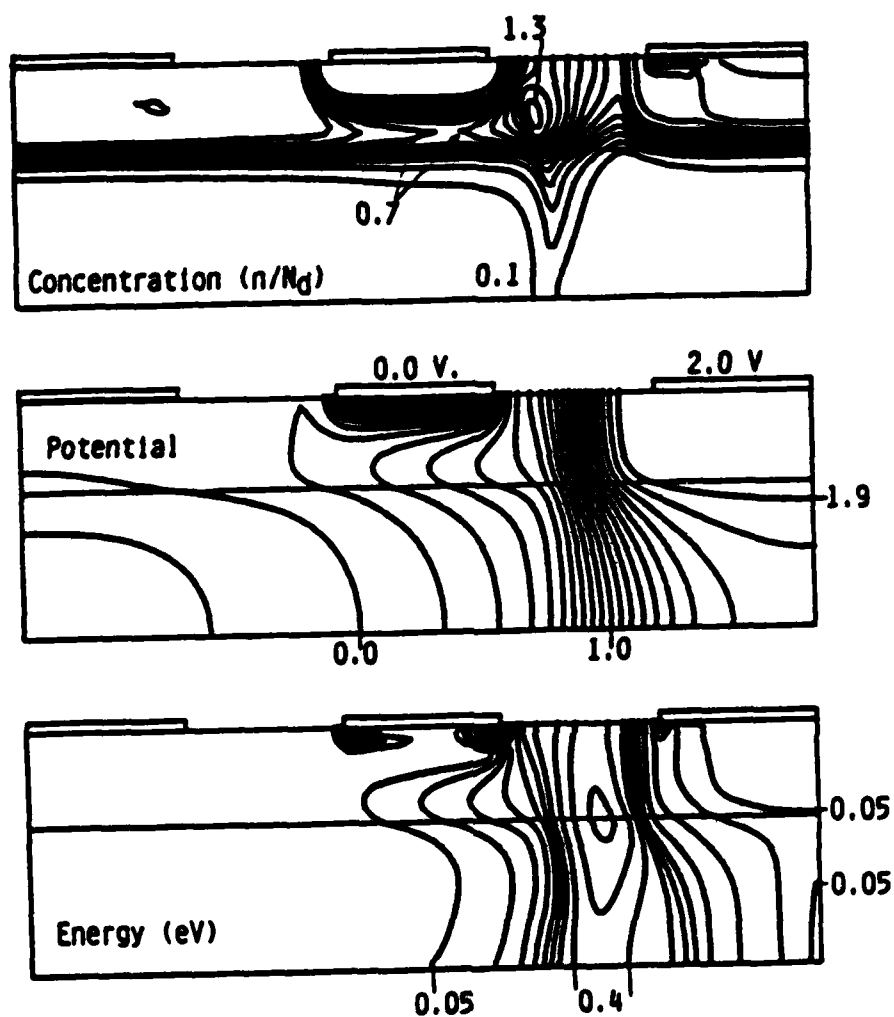


Fig. 3.4. The contour plots of the simulated MESFET at $t = 3.0$ ps, $V_g = 0.0$ and $V_{ds} = 2.0$ volts. For more details, see captions of Fig. 2.

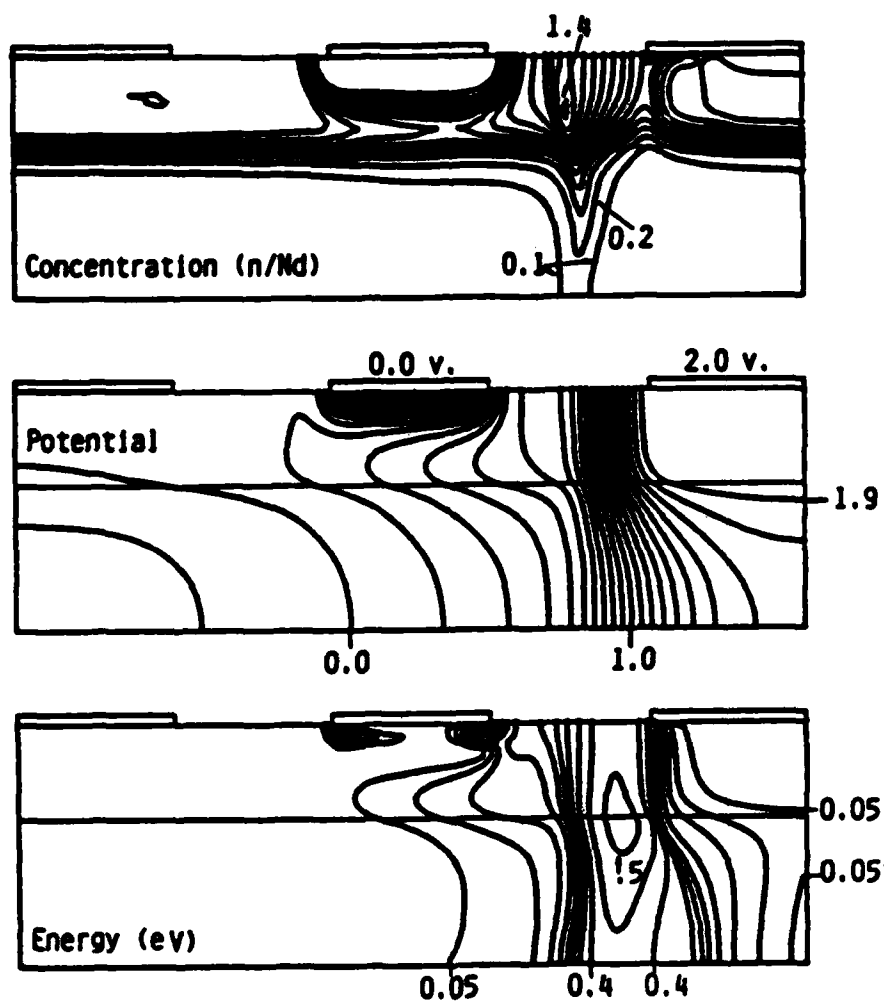


Fig. 3.5. The contour plots of the simulated MESFET at $t = 4.0$ ps, $V_g = 0.0$ and $V_{ds} = 2.0$ volts.

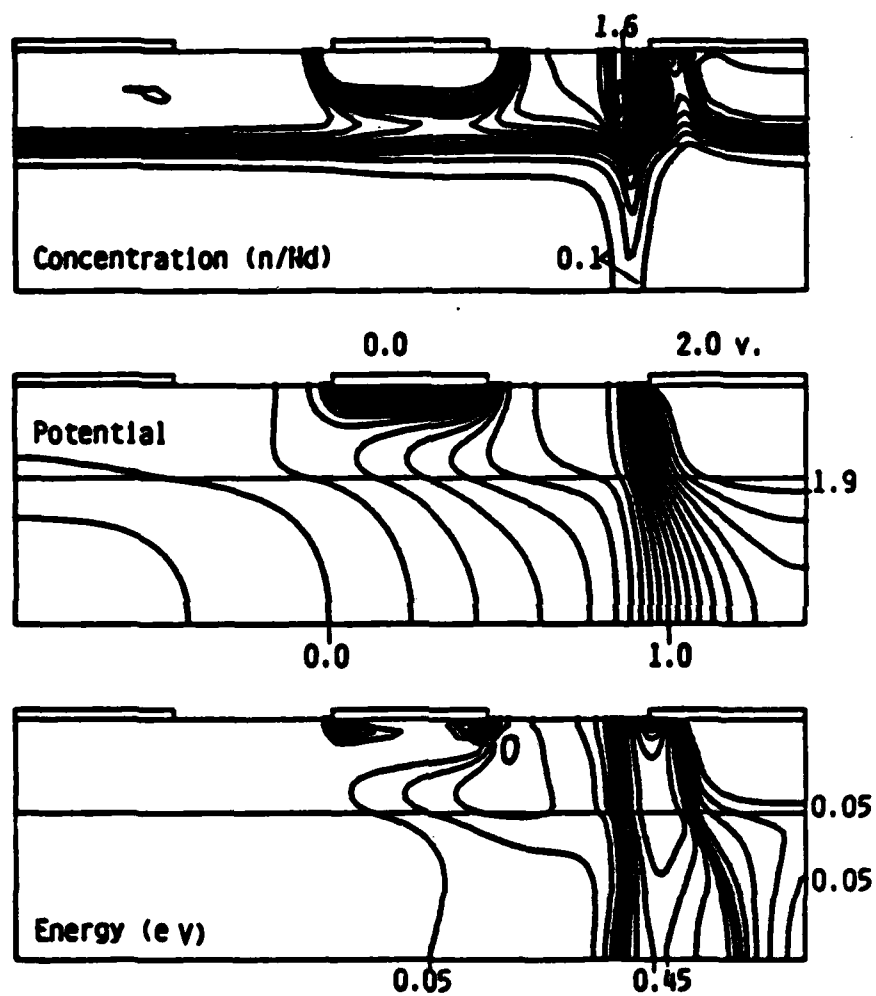


Fig. 3.6. The contour plots of the simulated MESFET at $t = 5.5$ ps, $V_g = 0.0$ and $V_{ds} = 2.0$ volts.

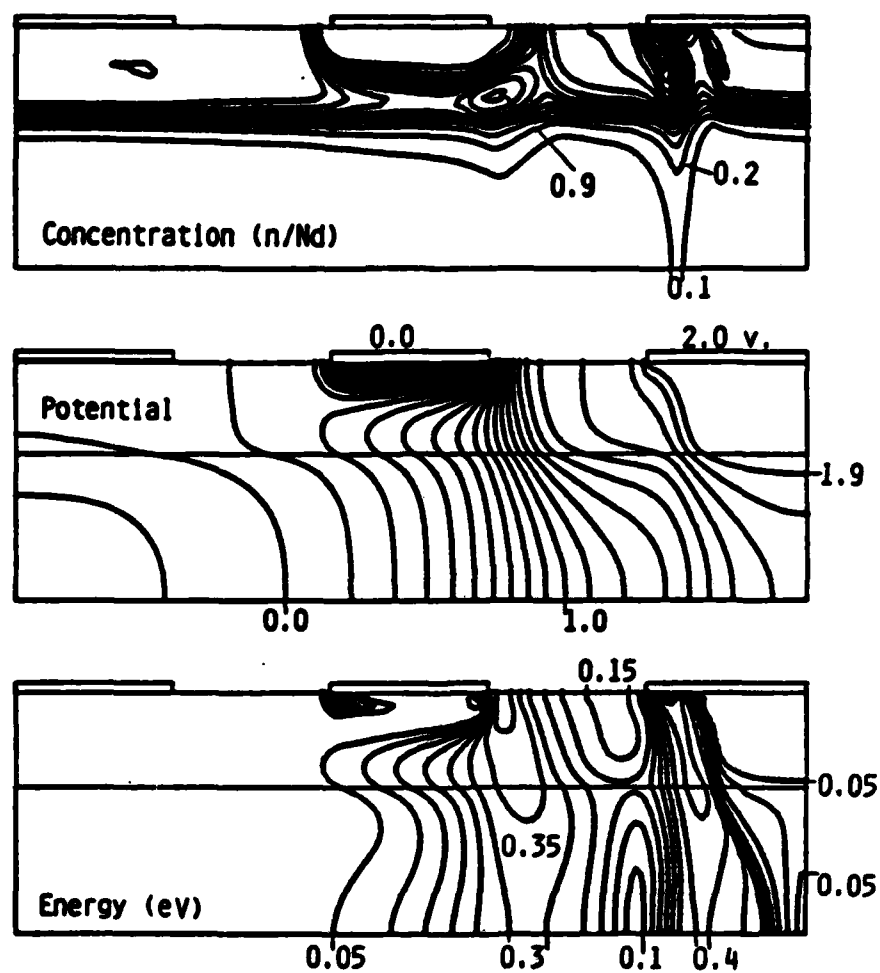


Fig. 3.7. The contour plots of the simulated MESFET at $t = 7.0$ ps, $V_g = 0.0$ and $V_{ds} = 2.0$ volts.

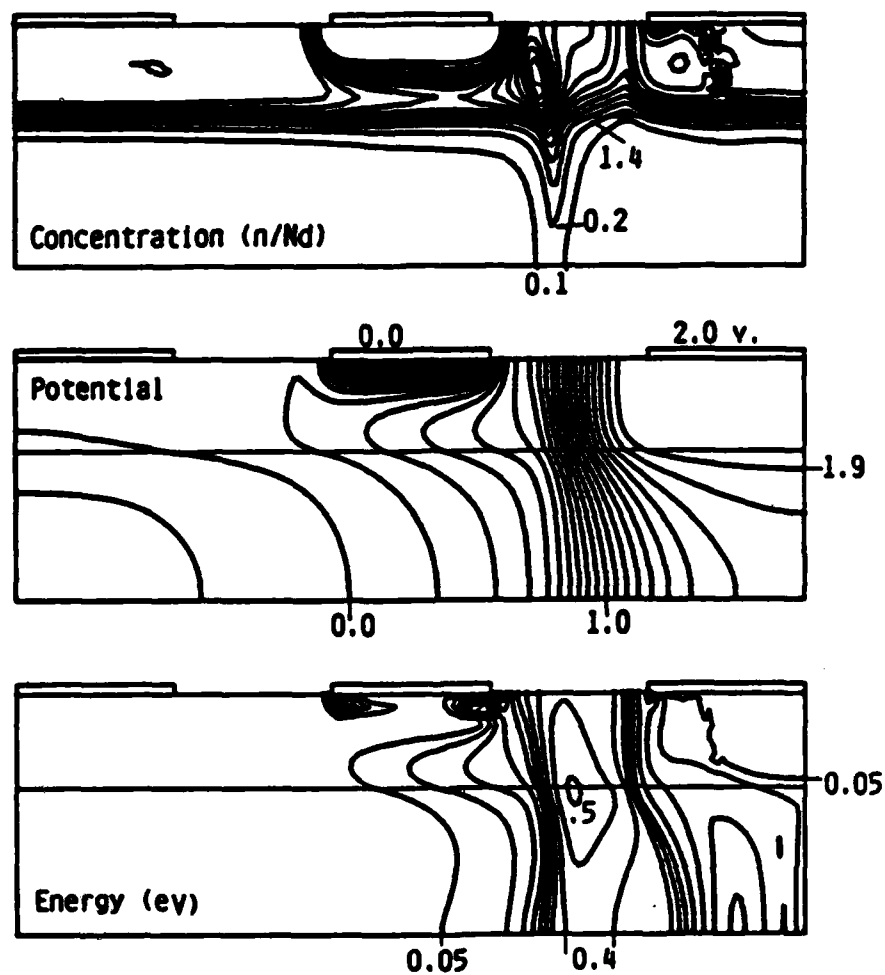


Fig. 3.8. The contour plots of the simulated MESFET at $t = 10.0$ ps, $V_g = 0.0$ and $V_{ds} = 2.0$ volts.

inherent instability of this structure. It is interesting to observe that the equipotential lines in Fig. 3.8(b) are quite similar to those in Fig. 3.4(b), which means that the oscillation period of this domain is about 7 ps.

3.3. SOURCE AND DRAIN CURRENTS AS FUNCTIONS OF TIME

The resulting source and drain currents as functions of time are shown in Fig. 3.9. For $t < 0.5$ ps, high transient currents are observed due to the application of the voltage step on the drain. For the next 3 ps, the electron energy rapidly increases as the electrons pass under the gate and it exceeds 0.35 eV. Consequently, considerable number of electrons are transferred into the secondary valleys. This results in a drop in the electron mobility, which is known as the negative differential mobility region. Hence, the domain starts to nucleate. During this nucleation time, the source current becomes greater than the drain current. Obviously, this extra current is used to charge the capacitor associated with the domain. The same argument applies to the time interval between 7.0 and 9.5 ps, which is the nucleation time of the new domain. During the discharge time, $5.0 < t < 7.0$ ps, the drain current exceeds the source current to remove the excess charge in the domain. It is noted that the areas between the two curves for the charge and the discharge times are equal.

3.4. THE OSCILLATION FREQUENCY

The domain propagation velocity is estimated as 1.08×10^7 cm/sec. The period of oscillation is estimated as 7 ps. This is the total time taken by the domain to become mature, come out from underneath the gate, cross the gate to drain region and to discharge. This results in a fundamental oscillation about 143 GHz. However, this frequency is about 25% less than that predicted using classical method ;

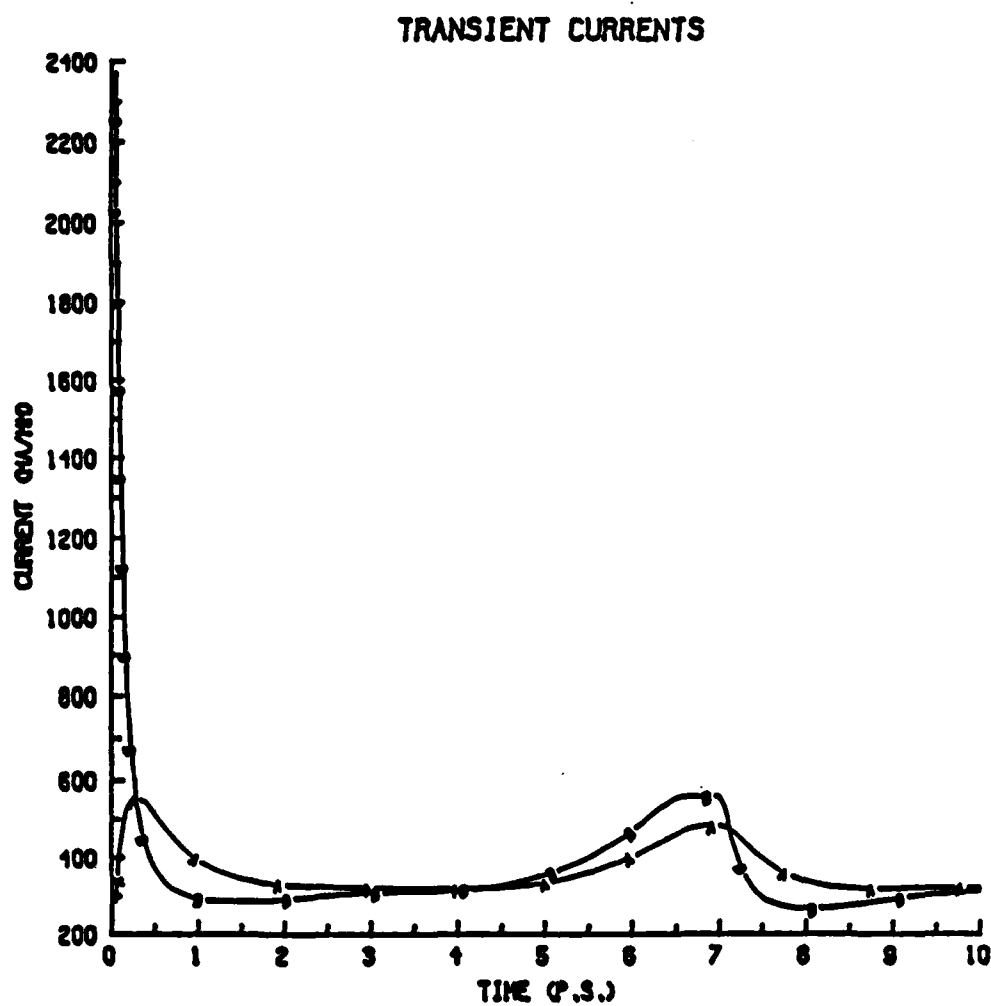


Fig. 3.9. Transient source and drain currents of the MESFET after applying the 2.0 volts step on the drain at $t = 0$. "—A—A—" Source current. "—B—B—" Drain current.

$$f = \frac{V_s}{L_{gd}} = \frac{10^7}{0.5 \times 10^{-4}} = 200 \text{ GHz} \quad (3.1)$$

where f is the oscillation frequency, V_s is the saturation velocity and L_{gd} is the gate to drain spacing. This difference is due to the fact that the domain starts to nucleate under the gate rather than at the gate-end on the drain side of the gate. Moreover, the domain does not discharge instantaneously when it reaches the drain, but it travels for a short distance under the drain. In other words, the finite charge and discharge times can not be neglected in this case. It is interesting to notice that such oscillations may not be observed in normal amplifier operation for two reasons. The first is that the load line bias combinations push the transistor away from the domain formation conditions. The second reason is that when such oscillations exist, they are filtered out by the selective network since they are very high frequencies compared to the normal range for MESFET operation.

3.5. EFFECT OF GATE VOLTAGE

By negatively biasing the gate, the depletion region becomes larger and the conducting channel becomes narrower and has less carrier concentration. Therefore, the possibility of a traveling domain formation is reduced. In this study, the traveling domain is observed at $V_g = 0.0 \text{ V}$ and -0.5 V . No traveling domain is observed at $V_g = -1.0 \text{ V}$ or lower.

The domain presence possibility when the channel is closed is presented in Fig. 3.10 which shows the contour plots for this device at $V_g = -2.0 \text{ volts}$ and $V_{ds} = 5.0 \text{ volts}$, at steady state. Even at this high drain voltage, no traveling domain is observed. However, a stationary local accumulation region is observed at the second half of the gate. The maximum carrier concentration inside this accumulation layer is less than the background doping. One should also notice that the average electron energy rapidly increases from less than 0.05 e.V at the gate entrance to about 0.6 eV at the gate exit.

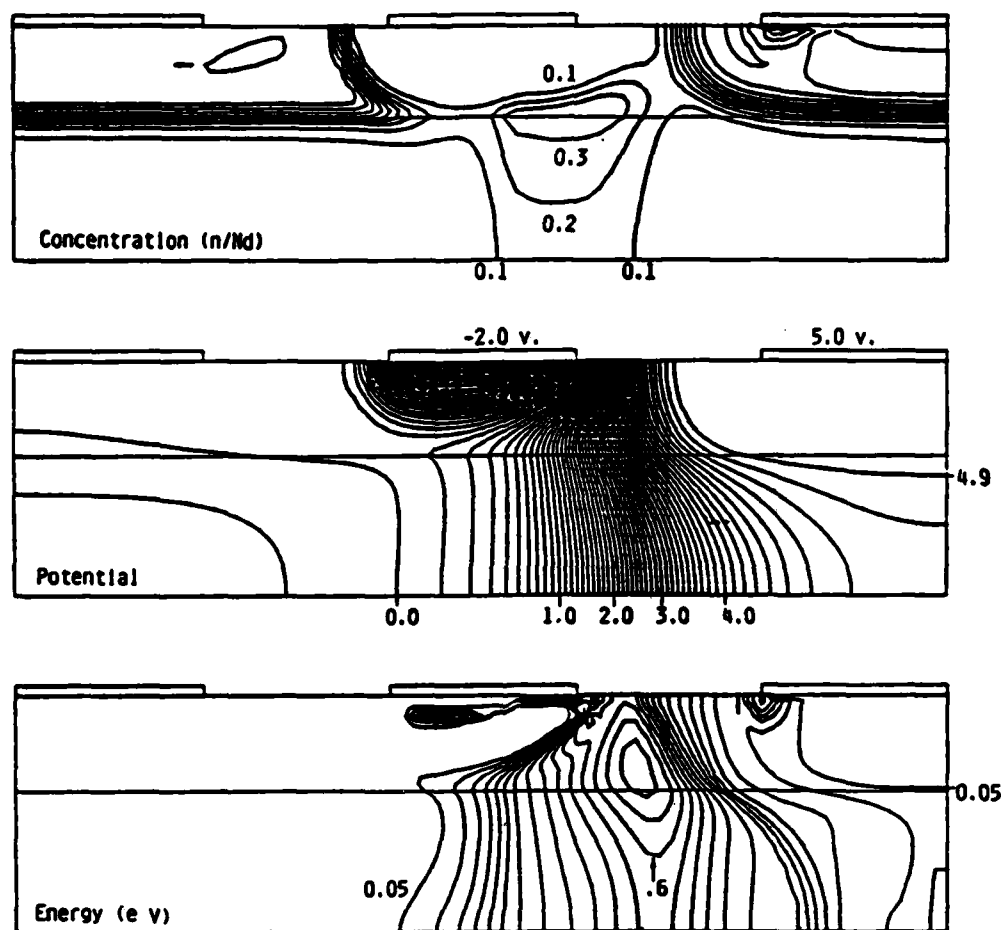


Fig. 3.10. The contour plots of the simulated MESFET at steady state. $V_g = -2.0$ volts and $V_{ds} = 5.0$ volts.

The conditions for traveling or stationary domain formation can be qualitatively deduced from the previous discussion. When the channel is open, the average energy and the electric field reach their threshold values for domain formation in a region where there are enough carriers to form a domain. Therefore, the traveling domain starts to nucleate under the gate exit. It becomes mature after traveling a short distance away from the gate where it finds high carrier concentration. On the other hand, for a closed channel, the electrons acquire high energy as they pass under the gate. Hence, the threshold field and energy are reached in a place where there are not enough carriers to form a domain. When the electrons eventually reach a high carrier concentration region, their velocity is already saturated and they possess no negative differential mobility to form a domain. The stationary domain forms to maintain current continuity by compensating for the velocity saturation and the channel narrowness at the gate exit.

The I-V characteristics for the MESFET with a traveling domain are not presented here for two reasons. First, when the traveling domain exists, the device current is a function of time ; the I-V characteristics represent the steady state solution which does not exist in this case. Second, the current measured experimentally, in this case, is the time average of the actual device current. The same process can be simulated on the computer. However, the resulting averaged current has no practical value from this discussion point of view and, not to mention, this process would be very time consuming.

3.6. STABLE STRUCTURE

A stable design for the MESFET (i.e. device free from traveling Gunn domains) can be obtained by using a narrower channel which, in other words, means using a thinner active layer. This idea is tested by simulating another MESFET similar to that shown in Fig. 3.1, but the active layer thickness is reduced to $0.15\text{ }\mu\text{m}$ rather than $0.2\text{ }\mu\text{m}$. All the other parameters are exactly the same. No traveling domain is observed for this design. The I-V characteristics for this device are shown in Fig. 3.11.

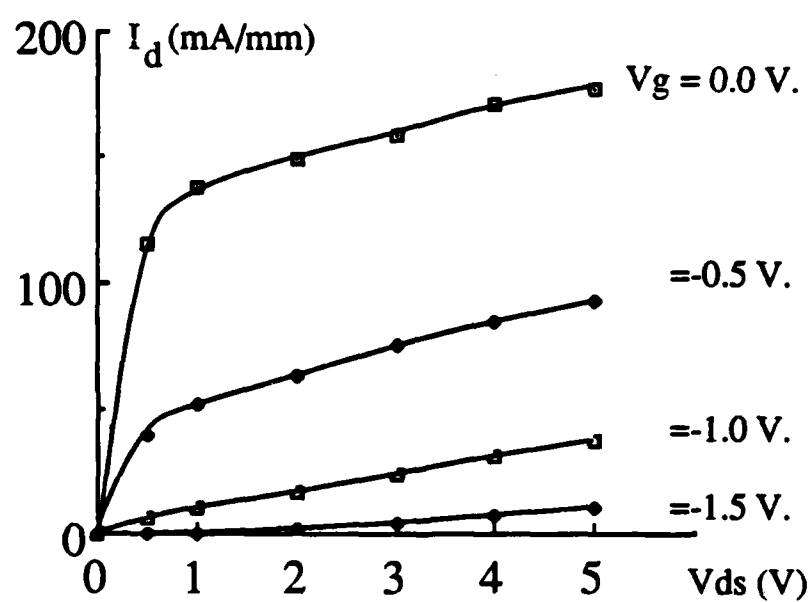


Fig. 3.11. The I-V characteristics of the MESFET of 0.15 μm active-layer thickness.

CHAPTER 4.

INVERTED-GATE FIELD-EFFECT-TRANSISTORS; NOVEL HIGH FREQUENCY STRUCTURES

4.1. INTRODUCTION

The gain and output power of a MESFET unit are directly related to the device width, which is the direction along the device electrodes and perpendicular to the electron flow. This width is limited by two factors. The first is the signal attenuation along the input electrode. The second is that the device width must be small compared to the wavelength to avoid any distributed effects. The first effect is the limiting one in the low frequency applications while, apparently, the second effect is only pertinent to the high frequency applications whenever there is a difference between the reactances of the input and output electrodes. These electrodes act as transmission lines since their width is comparable to the wavelength. Because of their different reactances, these input and output electrodes will have different phase velocities. To avoid phase cancellation due to this phase velocity mismatch, the device width is limited to 0.1 wavelength. This limitation becomes very severe in the mm-wave range. It also precludes the exploitation of the traveling wave phenomenon along the device width to realize what is called Traveling-Wave-Transistor [34]-[37] which is an MMIC amplifier. However, this restriction can be removed by having a transistor which possesses equal input and output reactances and, consequently, exhibits equal input and output phase velocities. This can be achieved by using a MESFET that has a symmetrical structure around the gate and employed in a common-gate configuration. The conventional coplanar MESFET, which has its gate is on the same plane as the source and the drain, far above the ground plane, does not permit proper R.F. grounding in the mm-wave range. Hence, it is not suitable for common-gate amplifiers. To overcome this problem, Yoder proposed the use of a non-coplanar FET in which the gate is located on the lower plane of the active layer

opposing the source-drain plane [38]. This device is called Inverted-Gate Field-Effect Transistor (INGFET) [39].

In fact the idea of non-coplanar FET's is not new. For example, Krusius *et al.* proposed the Opposed-Gate-Source Transistor (OGST) and reported its fabrication as well [40]. Though non-coplanar and symmetrical around its gate, the OGST does not possess equal input and output reactances and, hence, cannot be used as a traveling-wave transistor.

The INGfet overcomes another problem facing the mm-wave transistors, namely the metallic-gate resistance. It is commonly accepted that operating a FET at high frequencies means employing shorter gate-length. The gate length becomes shorter than $0.5\text{ }\mu\text{m}$ in the mm-wave range. This reduces the cross-sectional area of the gate electrode and, thus, increases the metallic-gate resistance. The height of the gate-electrode is increased as a way to obtain a larger cross-sectional area. Eventually, the gate electrode becomes high and thin and, therefore, vulnerable since it can be broken easily. In contrast, Fig. 4.1(a) shows that in the INGfet, the gate can be realized with a large cross-sectional area [38]; hence, this problem is practically eliminated.

In this chapter, the D.C. characteristics of the Inverted-Gate FET (INGfet) are simulated. The characteristics of the INGfet are to be compared with those of the corresponding coplanar structure. Finally, another device called Inverted-Gate-Injection FET (INGIFET) is to be presented. The promising characteristics of this device as well as its intrinsic small-signal parameters are predicted using the same computer model presented before.

4.2. INVERTED-GATE FET

The first simulated INGfet, Device I, is shown in Fig. 4.1(b). It consists of an active layer of $0.2\text{ }\mu\text{m}$ thickness, doped at 10^{17} cm^{-3} . A gate of $0.5\text{ }\mu\text{m}$ length is located on the lower plane of the active layer. The source and the drain electrodes are on the top plane of the active layer, in a symmetrical position with respect to the gate. Obviously, there is no need to simulate a substrate for this structure since the effective conduction is confined to the active layer. The source and the drain ohmic contacts are considered as ideal ones. However, the resistances of these contacts can be taken

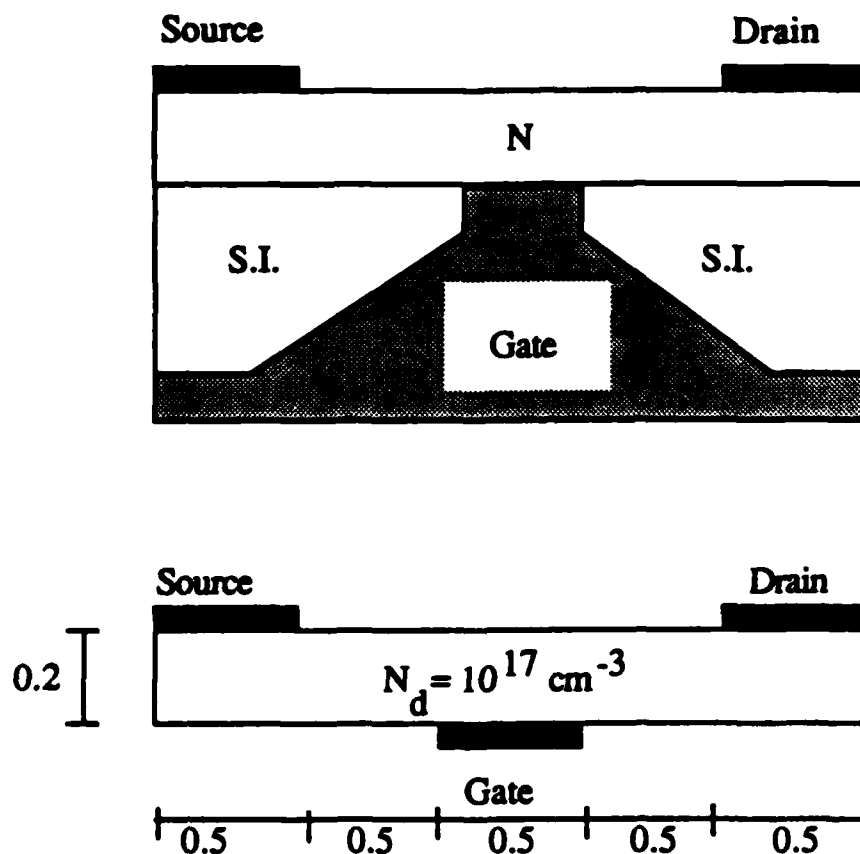


Fig. 4.1. (a) The actual Inverted-Gate FET and (b) the dimension, in microns, of the simulated one.

into consideration as parasitic elements in the extrinsic equivalent circuit of the device. The built-in junction potential is taken as 0.8 volt. To account for scattering due to ionized impurities, the selected average mobility curve has a maximum value of 5000 $\text{cm}^2/\text{volt}\cdot\text{sec.}$ at low energy values. The mobility drops to about 300 $\text{cm}^2/\text{volt}\cdot\text{sec.}$ at very high energy values.

Fig. 4.2(a-c) shows the contour plots of the carrier concentration, electric potential, and average electron energy for this device at $V_g = -0.5$ volt and $V_{ds} = 5.0$

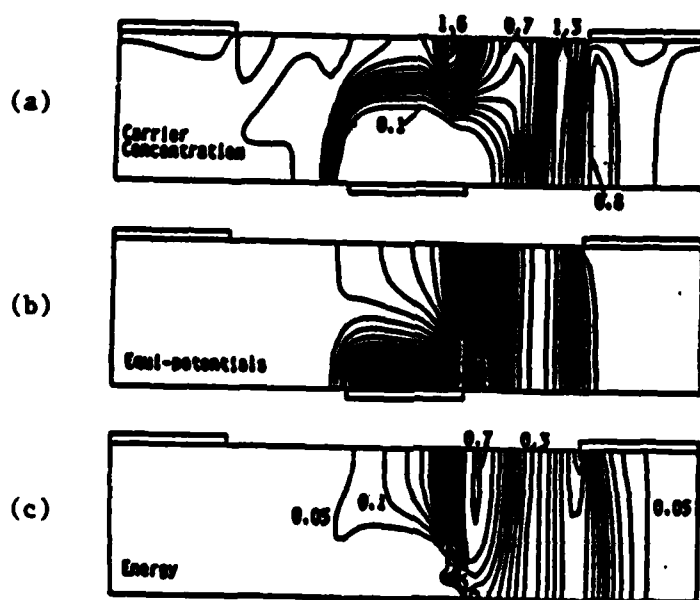


Fig. 4.2. The contour plots of the INGDET, Device I, at $V_g = -0.5$ volt and $V_{ds} = 5.0$ volts. (a) The carrier concentration (n/N_d) is shown in steps of 0.1. (b) The equi-potential lines are shown in steps of 0.1 volt. (c) The average electron energy shown in steps of 0.05 e.V.

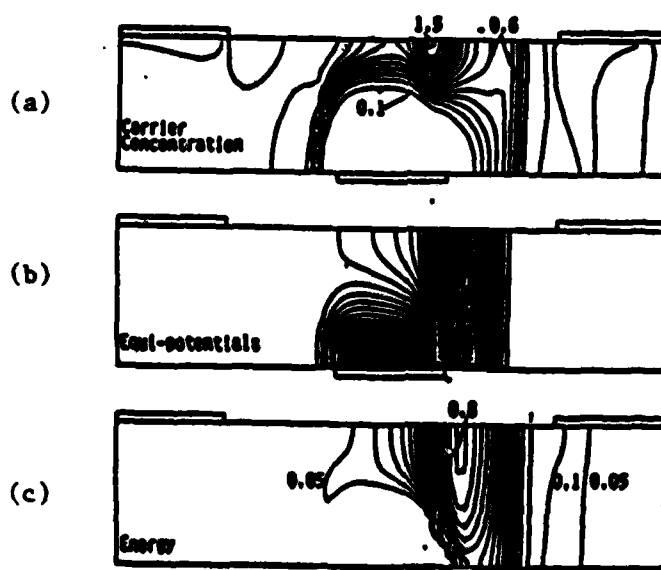


Fig. 4.3. The contour plots of the INGDET, Device I, at $V_g = -1.0$ volt and $V_{ds} = 5.0$ volts. For more explanation, see caption of Fig. 4.2.

volts. It is interesting to notice that a stationary domain is formed in the channel above the gate. In this domain, the carrier concentration exceeds $1.6 \times 10^{17} \text{ cm}^{-3}$ in the accumulation layer then drops below $0.7 \times 10^{17} \text{ cm}^{-3}$ in the depletion layer. Moreover, a traveling Gunn domain is formed in the channel between the gate and the drain. The state of this domain after traveling close to the drain is shown. The accumulation layer of this domain has a concentration above $1.3 \times 10^{17} \text{ cm}^{-3}$. Its depletion layer has a concentration below $0.8 \times 10^{17} \text{ cm}^{-3}$. Fig. 4.2(b) shows that two high field regions are associated with these domains. The electric field associated with the stationary domain is substantially higher than that associated with the traveling domain. Fig. 4.2(c) shows that two high energy regions spatially precede these two domains (i.e. towards the source-side of the device). The mechanism leading to the formation of these domains can be understood as follows. The relatively narrow channel above the gate requires higher electric field to maintain current continuity. This high electric field results in a higher energy; consequently, the mobility drops. The carrier concentration increases in order to compensate for the mobility drop. This process continues until a balance is reached between all the parameters. When this balance is reached while a strong enough electric field is still existing in the region between the gate and the drain, a traveling domain is formed in order to absorb this extra field. This leads us to the idea that by closing the channel above the gate (i.e. applying more reverse bias to the gate) while keeping the drain to source voltage constant, the traveling domain may disappear. This is explained by the fact that a narrower channel above the gate requires a higher electric field which is gained at the expense of the field between the gate and the drain. Eventually, the electric field in the region between the gate and the drain drops to a value below the threshold field necessary for the traveling domain formation. This idea is proven to be correct in Fig. 4.3(a-c) which shows the device state at $V_g = -1.0$ volt and $V_{ds} = 5.0$ volts. It is shown that the traveling domain disappeared by closing the channel. It also shows that the maximum carrier concentration inside the stationary domain is below $1.6 \times 10^{17} \text{ cm}^{-3}$. Evidently, this is to produce lower output current. On the other hand, all the high field region is associated with the stationary domain; the rest of the device has a low electric field, except the depletion region of course. A slight increase in the average electron energy is also observed. This energy increase does not practically affect the electron velocity since this velocity is already saturated.

The oscillation frequency of the traveling domain is about 150 GHz. This frequency is far above the normal operating frequency of this transistor. Nevertheless, one must get rid of this domain since it adversely affects the device speed. This can be achieved by properly biasing the device as it was shown before. On the other hand, it can also be permanently suppressed by [7]:

- 1) Reducing the gate-to-drain separation.
- 2) Reducing the active layer thickness.
- 3) Lightly doping the active layer.

Bearing in mind that the gate-to-drain separation is currently equal to $0.5\ \mu\text{m}$, the first alternative listed above becomes unfavorable since it may lead to an unrealistic design.

Starting by the second alternative, Fig. 4.4(a) shows Device II which is an INGfet similar to Device I, but its active layer thickness is reduced to $0.1\ \mu\text{m}$. This transistor is normally off; therefore, a positive voltage must be applied to the gate in order to get a practical output current. The contour plots of this device, at $V_g = 0.6$ volt and $V_{ds} = 5.0$ volts, are shown in Fig. 4.5(a-c). This figure clearly shows that the traveling domain has been suppressed but the stationary domain is still existing. One should notice that this stationary domain reaches the maximum accumulation right at the gate exit and extends over longer distance compared to the case of Device I (see Fig. 4.3(a))

4.3. COMPARISON BETWEEN INGfet AND COPLANAR MESFET

In order to have a fruitful discussion, the corresponding conventional coplanar MESFET is also simulated. This coplanar MESFET, Device III, is shown in Fig. 4.4(b). The dimensions and the doping are kept the same as in Device II. However, a buffer layer of $0.3\ \mu\text{m}$ thickness is added to this device in order to have a realistic coplanar MESFET. To account for the imperfections of the buffer layer, its maximum electron mobility is set equal to $5000\ \text{cm}^2/\text{volt}\cdot\text{sec}$.

Figures 4.6 and 4.7 show the I-V characteristics for Devices II and III respectively. By comparing the two characteristics, one should notice the following:

- 1) Device III has a higher saturation current than Device II for the same bias condition.

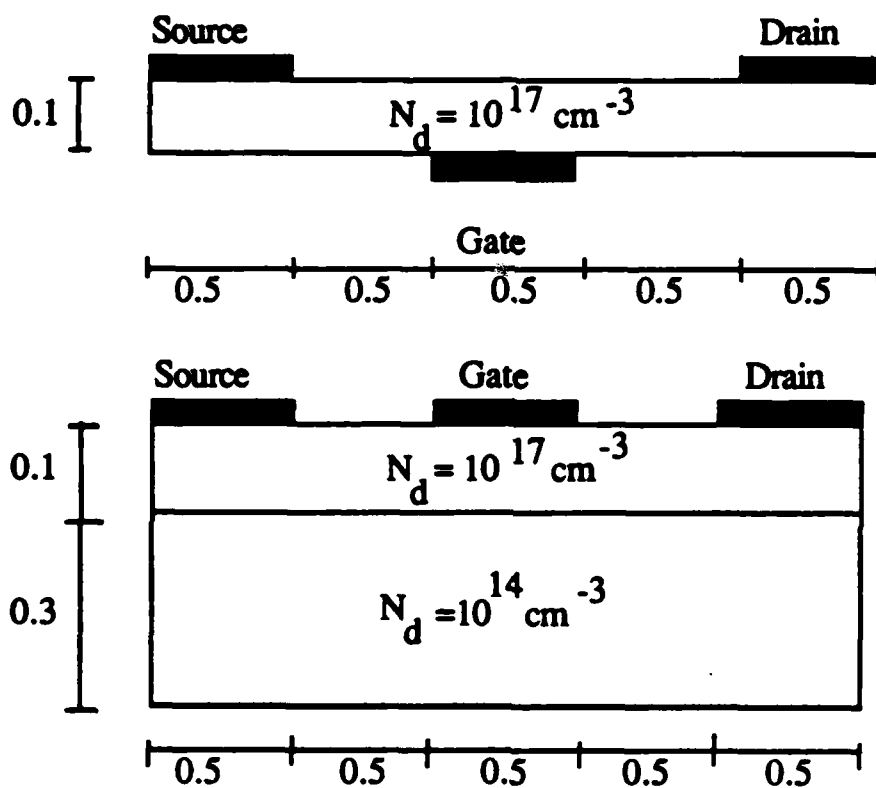


Fig. 4.4. Dimensions of the simulated (a) INGfet, Device II, and (b) the coplanar MESFET, Device III.

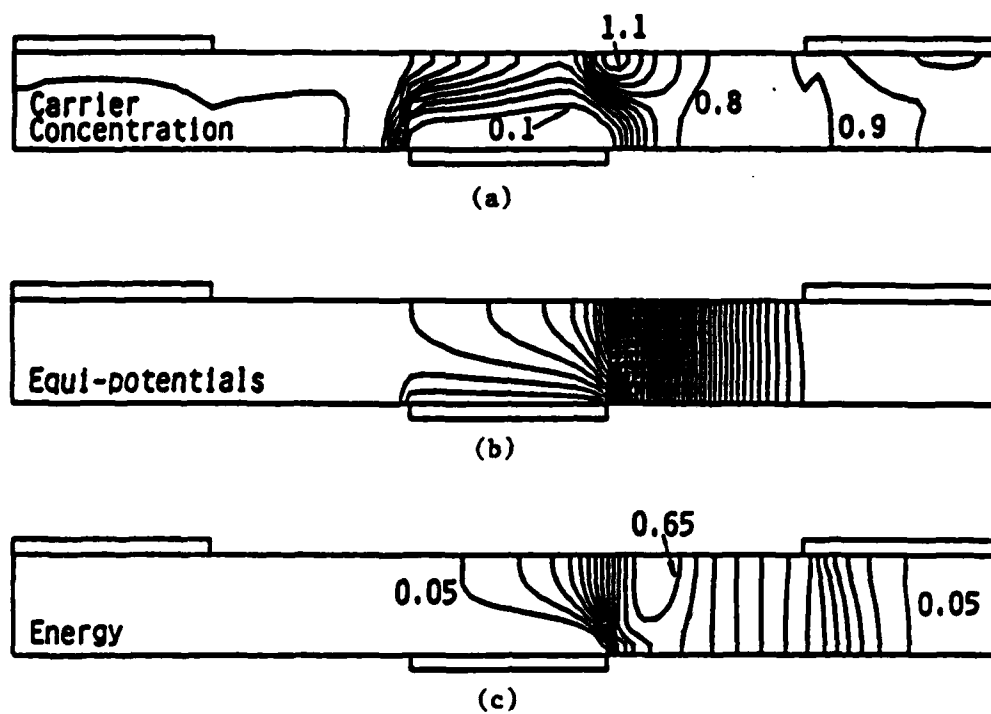


Fig. 4.5. The contour plots of Device II at $V_g = 0.6$ volt and $V_{ds} = 5.0$ volts.

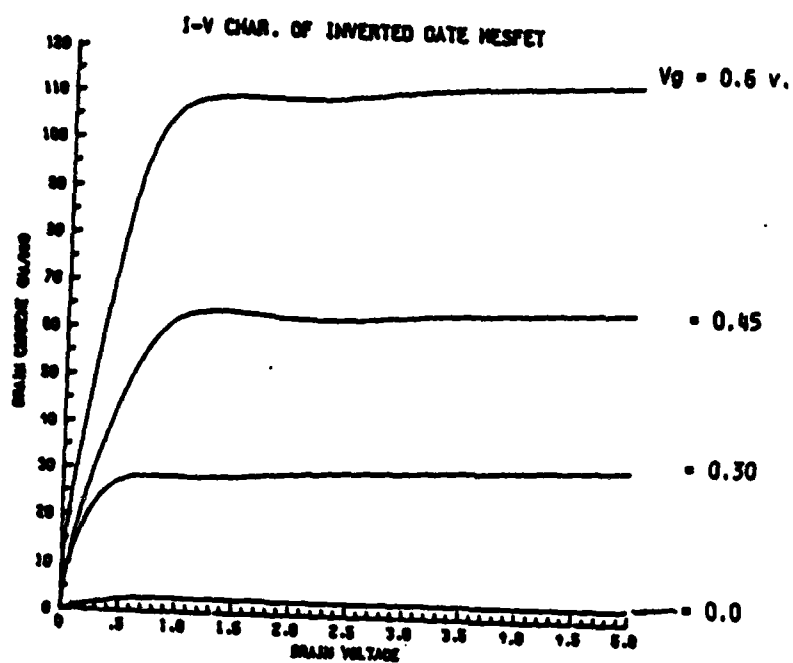


Fig. 4.6. The I-V characteristics of the INGFET, Device II.

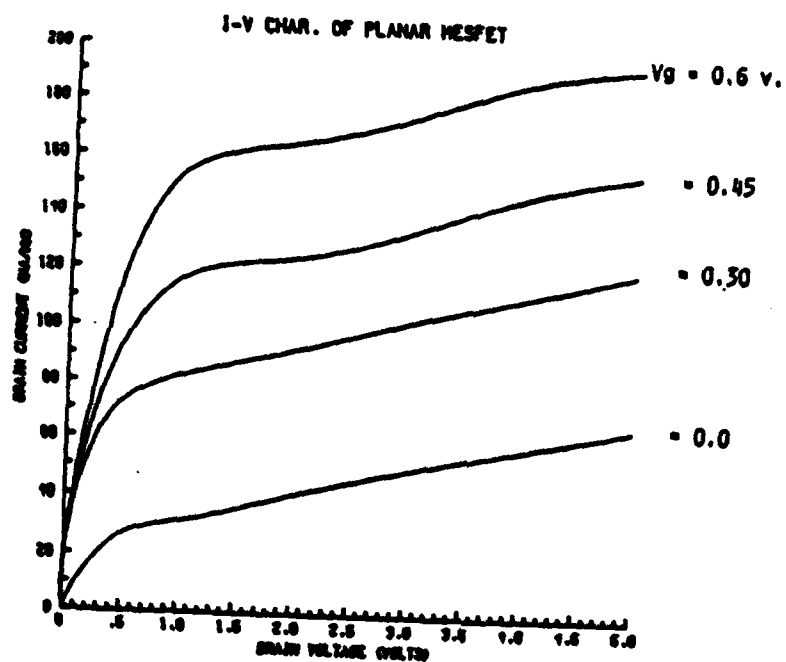


Fig. 4.7. The I-V characteristics of the coplanar MESFET, Device III.

- 2) At $V_g = 0.0$, Device II reaches complete pinch-off while Device III still has an appreciable output current.
- 3) The I-V curves of Device III have a higher slope in the saturation region which means higher drain conductance (g_d).

These three major differences can be attributed to the carrier injection into the semi-insulating buffer-layer of Device III. This is clearly illustrated in Fig. 4.8(a). This figure shows that at $V_g = 0.0$ and $V_{ds} = 4.0$ volts, the channel of Device III is practically depleted, but the buffer-layer still has a carrier concentration above 10^{16} cm^{-3} , injected from the active-layer. Considering Fig. 4.9 which shows the amount of current passing through the buffer-layer as a percentage of the total drain current for Device III, it is shown that all the drain current is actually passing through the buffer-layer at $V_g = 0.0$.

The transconductance dependence on V_{ds} for Device II and Device III is shown in Fig. 4.10. It is shown that the non-coplanar MESFET has the highest transconductance (above 300 mS/mm) at high gate bias. However, it drops to about half the corresponding values of the coplanar MESFET at low gate voltage. Again, this is due to the carrier injection into the buffer layer in case of device III which results in a larger dynamic range. The gate-to-source-capacitance of these two devices is shown in Fig. 4.11. It is quite interesting to notice that the non-coplanar MESFET always has a lower gate-to-source capacitance compared to the coplanar MESFET for the same bias condition. By combining the data of Figures 4.10 and 4.11 to obtain the current-gain-cutoff frequency ($f_t = g_m / 2 \pi c_{gs}$), one can easily see that the non-coplanar MESFET supersedes the coplanar one from this figure of merit point of view.

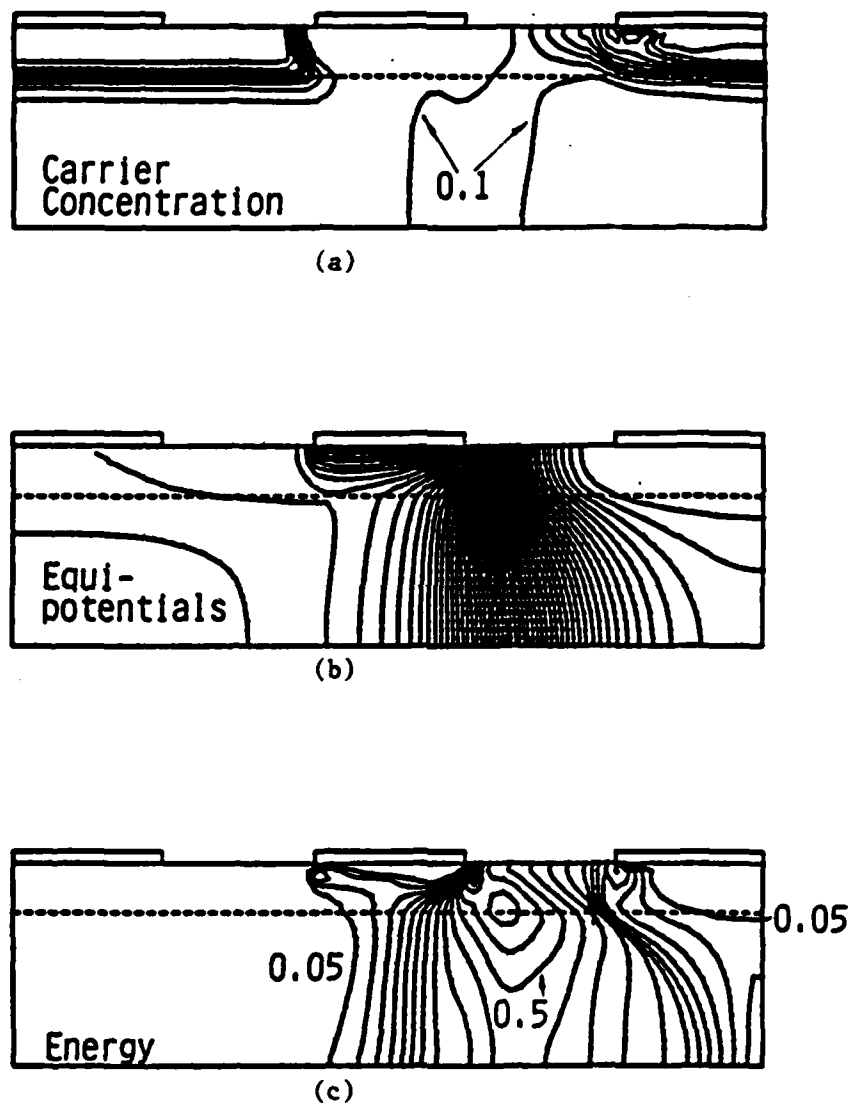


Fig. 4.8. The contour plots of the coplanar MESFET at $V_g = 0.0$ and $V_{ds} = 4.0$ volts.

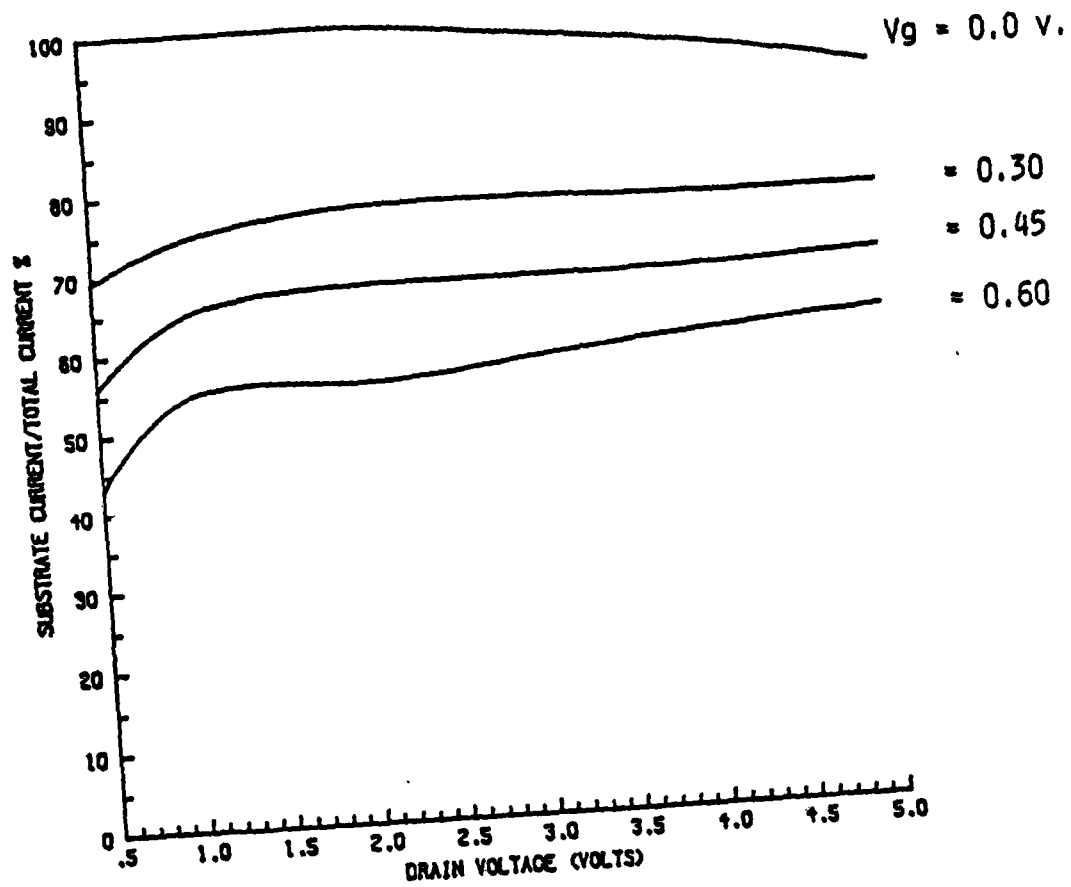


Fig. 4.9. The substrate current as a percentage of the total drain current versus the drain voltage, for different gate voltages.

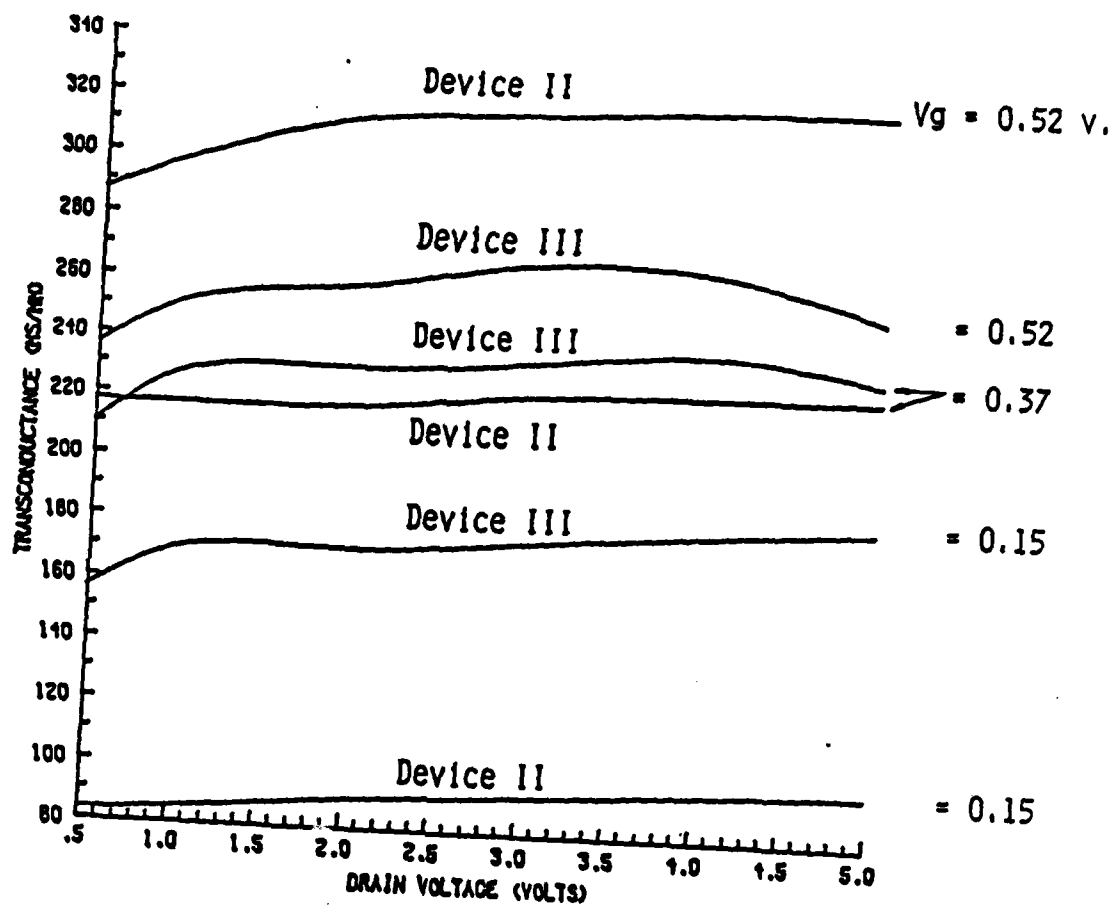


Fig. 4.10. The transconductance in mS/mm of the INGNET, Device II, and the coplanar MESFET, Device III, as a function of V_{ds} . V_g is a parameter.

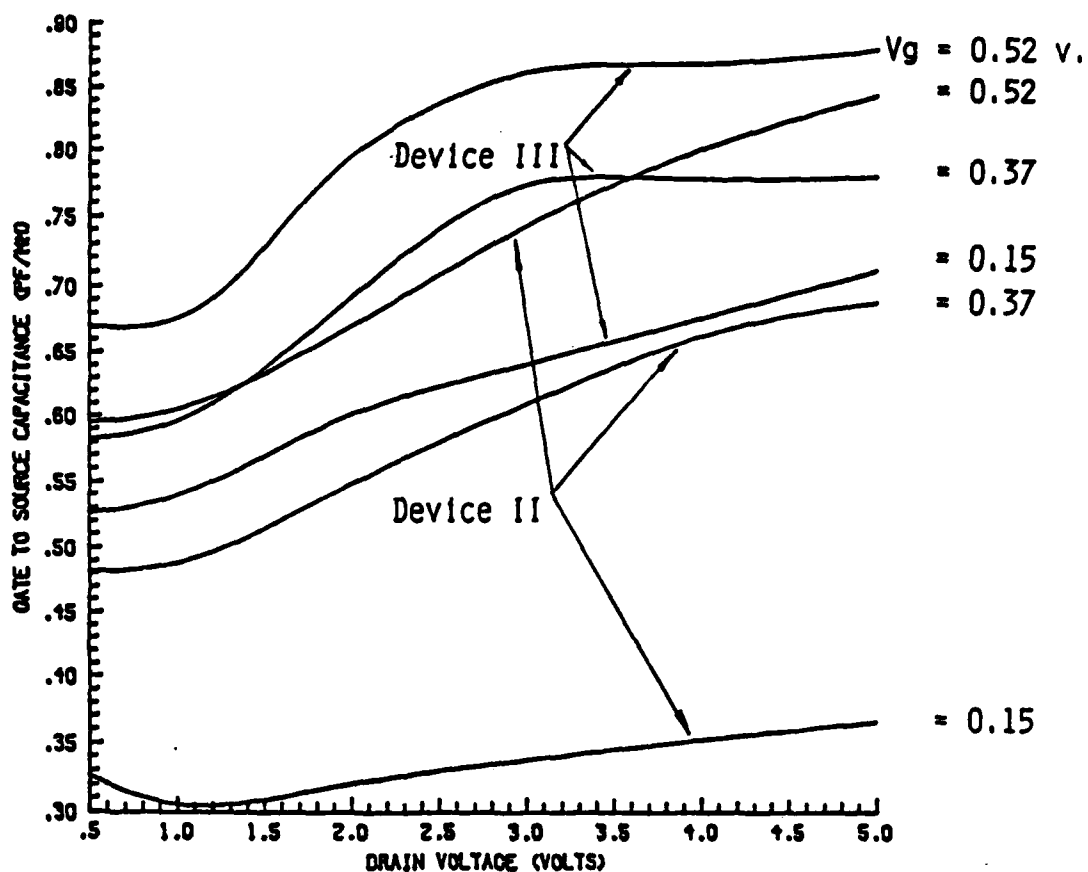


Fig. 4.11. The gate-to-source-capacitance in pF/mm of the INGFEt, Device II, and the coplanar MESFET, Device III, as a function of V_{ds} . V_g is a parameter.

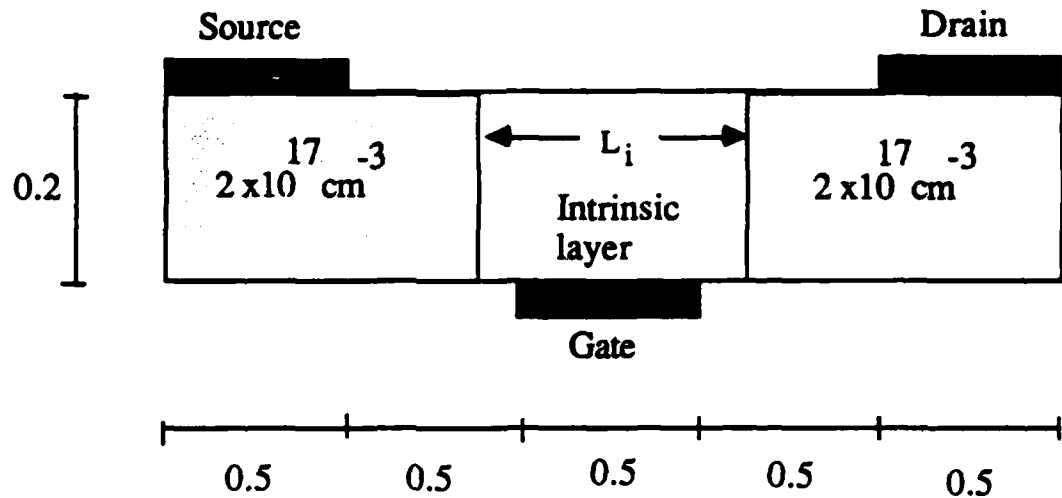


Fig. 4.12. The Inverted Gate Injection FET. Dimensions are in microns.

4.4. INVERTED-GATE-INJECTION FET

One of the alternatives, that can be used to permanently suppress the traveling domain in the INGfet, is to lightly dope the active layer. Direct application of this idea is not desirable since it may drastically reduce the device current. This idea can be applied indirectly by introducing a lightly doped region between two highly doped regions as shown in Fig. 4.12. The principle of operation of this device is the injection of the space-charge carriers over the $N^+ \text{-i-} N^+$ structure. Most of the applied potential is absorbed in the $i\text{-}N^+$ junction in the drain side of the device; this mechanism ensures that no domain can be formed inside this device. It is called Inverted- Gate-Injection FET (INGIFET).

The INGIFET has two advantages over the INGfet. First, the doping density, the active layer thickness and the intrinsic region length can be changed independently for any practical design values without any possibility of having a traveling domain. This greatly simplifies the optimization procedure that has to be performed in order to exploit the potential capabilities of this transistor. Second, the low field electron mobility above the gate is increased due to the absence, or at least

reduction, of the scattering by ionized impurities. This directly leads to a higher transconductance and higher operating frequency owing to the smaller transit time under the gate.

This principle of operation, space-charge-carrier injection, was proposed in a general form by Eastman *et al.* [41] without any determination of the performances. Fauquembergue *et al.* studied a symmetrical N^+ -i- N^+ FET, which employs the same principle of operation, using Monte-Carlo simulation [42]. They showed its superiority over the conventional FET's. One should notice that although the same concept is used here, as the other two authors, the motivation that led to it is different; their motivation was up-grading the FET performance while our major concern is to suppress the traveling domain; although the other improvements were gained as well

To study the effect of the intrinsic layer length (L_i) we simulated the structure shown in Fig. 4.12. The two identical N^+ regions are doped at $2 \times 10^{17} \text{ cm}^{-3}$; the low field mobility is set equal to $4000 \text{ cm}^2/\text{v}.\text{sec}$. The low field mobility in the intrinsic region is equal to $7500 \text{ cm}^2/\text{v}.\text{sec}$. This intrinsic region is symmetrically positioned around the center of the device. The total device length is equal to $2.5 \mu\text{m}$ and the thickness of the active layer is taken as $0.2 \mu\text{m}$. Three different values for the intrinsic region length (L_i) are considered, $0.7 \mu\text{m}$, $0.5 \mu\text{m}$ and $0.3 \mu\text{m}$. The I-V curve for the three devices, at $V_g = 0.6 \text{ V}$, is shown in Fig. 4.13. It shows that the device current dramatically increases by the decrease of L_i . Moreover, by reducing L_i , a transition from a typical saturating pentode-like characteristics of MESFET's to a triode-like characteristics is observed. This transition is because of the square-law nature of the space-charge-limited current in the intrinsic region [43]-[45].

The INGIFET which has $L_i = 0.3 \mu\text{m}$ is selected to evaluate its complete I-V characteristics, since it produces the largest current per unit width. It will be referred to as Device IV. Fig. 4.14 shows the contour plots of this device at $V_g = 0.6 \text{ volt}$ and $V_{ds} = 3.0 \text{ volts}$. Fig. 4.14(a) shows that the carrier concentration exceeds 10^{16}

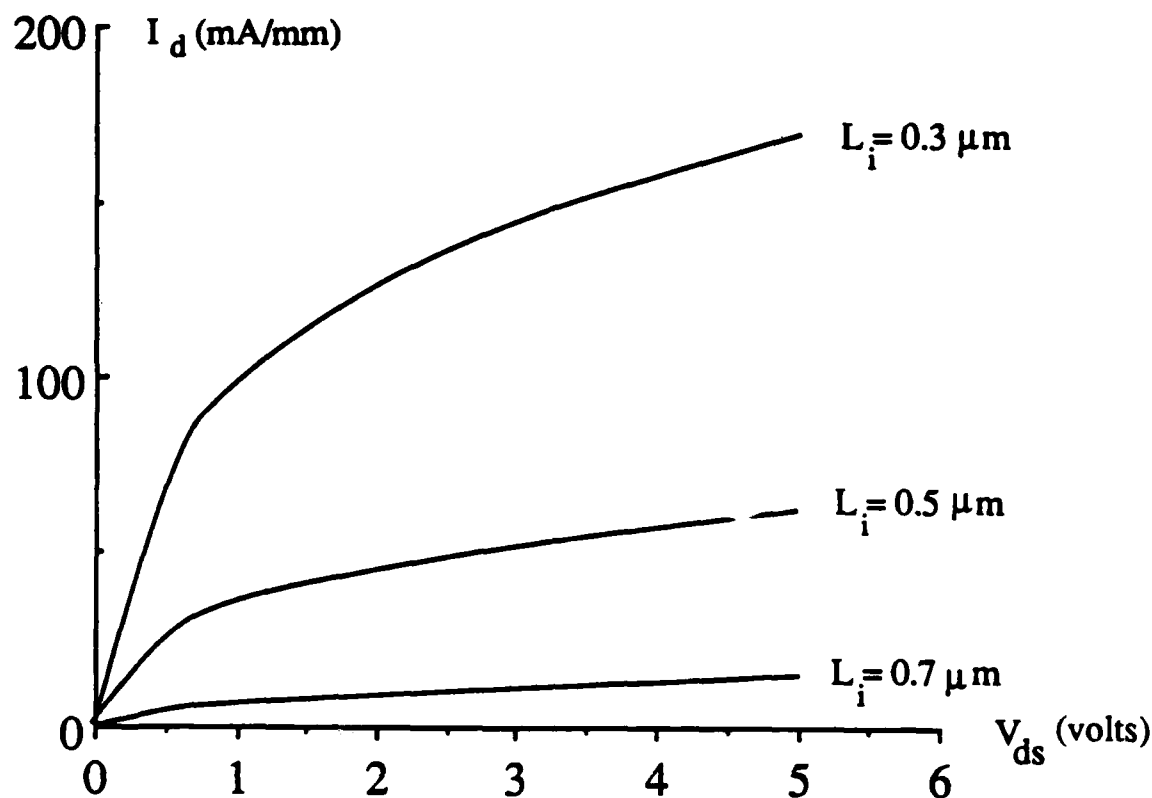


Fig. 4.13. The drain current variation of the INGIFET with the drain voltage at $V_g = 0.6$, for three different intrinsic region lengths (L_i).

cm^{-3} in the intrinsic region and reaches up to $8 \times 10^{16} \text{ cm}^{-3}$; this clearly manifests the strong injection mechanism over the $N^+ \text{-i}$ junction. Fig. 4.14(b) confirms that most of the applied potential is stored in the i-N^+ junction in the drain-side of the device and, hence, neither traveling nor stationary domain can be formed in the INGIFET. Furthermore, this high field region results in a high energy region. Apart from this region, the electron energy is below 0.05 e.V. The characteristic I-V curves of this device are shown in Fig. 4.15. The triode-like I-V behavior of these curves is quite obvious over the whole range of V_g values.

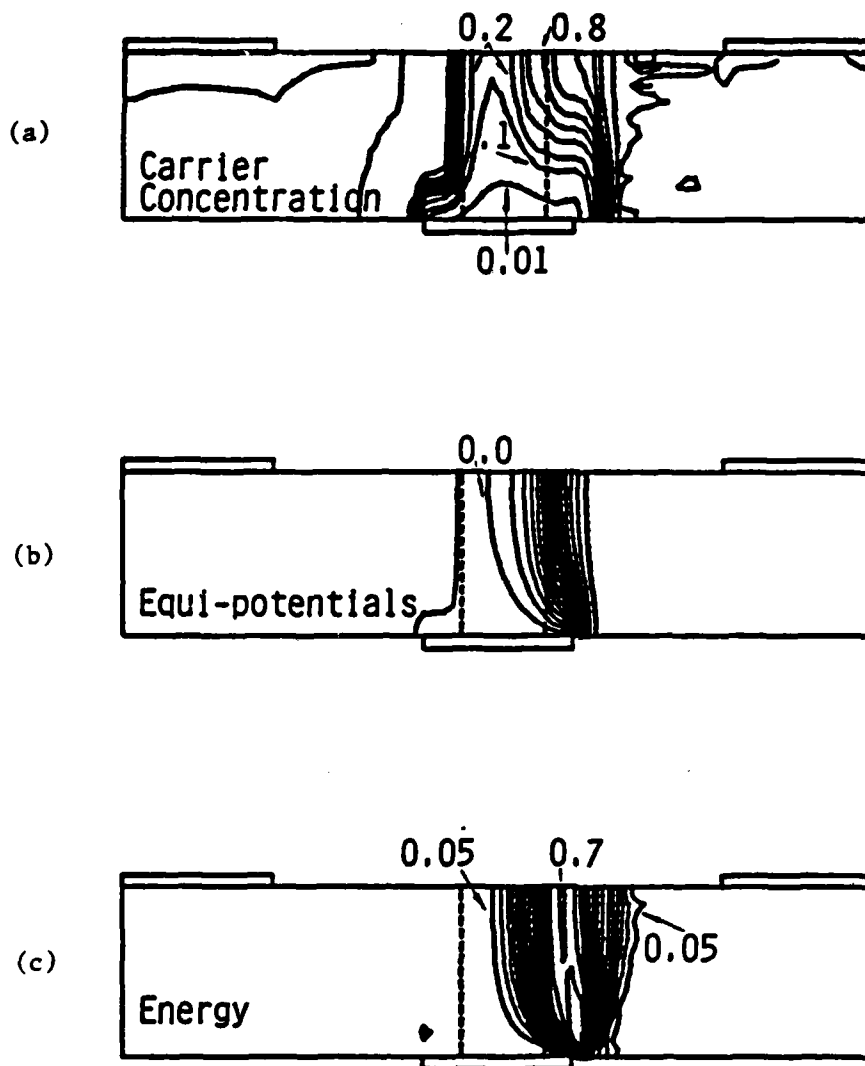


Fig. 4.14. The contour plots of the INGIFET, Device IV, at $V_g = 0.6$ V and $V_{ds} = 3.0$ V. (a) The carrier concentration lines ($n/10^{17}$) are shown as 0.01, 0.1, and steps of 0.2 hereafter. (b) The equip-potential-lines are shown in steps of 0.2 V. (c) The average electron energy is shown in steps of 0.05 eV.

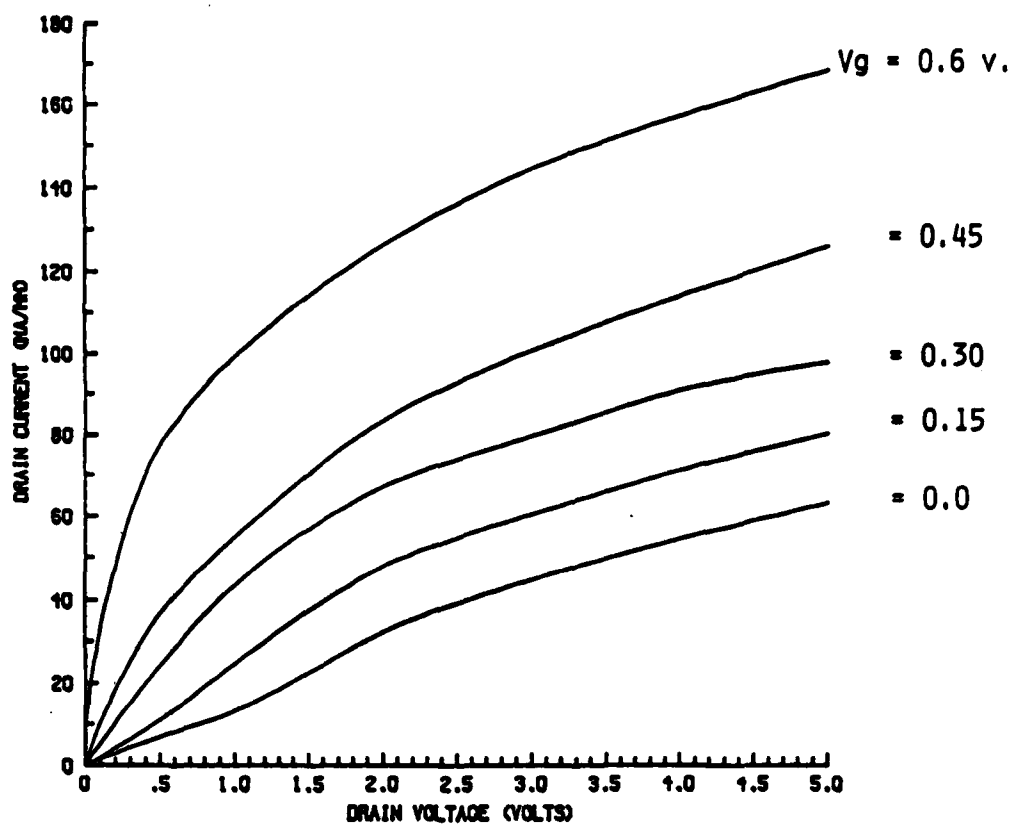


Fig. 4.15. The I-V characteristics of the INGIFET, Device IV.

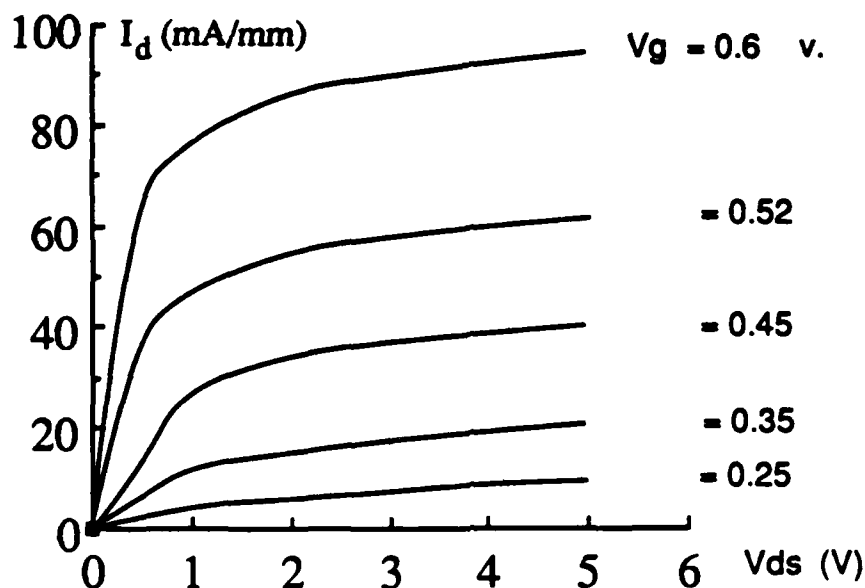


Fig. 4.16. The I-V characteristics of the INGIFET, Device V.

For the sake of comparison between the INGIFET and the INGIFET, another transistor, Device V, which has an active layer thickness equal to $0.1 \mu\text{m}$ is simulated. In order to get a practical current out of this device, the N^+ layers are doped at $4 \times 10^{17} \text{ cm}^{-3}$; consequently the low-field mobility is adjusted to $2000 \text{ cm}^2/\text{V}\cdot\text{sec}$. The electrodes dimensions and locations are kept the same as in Device II and Device IV. The I-V characteristics of this INGIFET are shown in Fig. 4.16. One major difference is observed between this Figure and Fig. 4.15; the triode-like characteristics is changed into a saturated pentode-like characteristics. Actually, this saturated pentode-like characteristics is a direct result of the high doping of the N^+ regions which enhances the injection mechanism so that the current is not a space-charge limited any longer. Another major difference is that Device V has a smaller current than Device IV although both devices have the same doping-density-active-layer-thickness product. This shows that this device is more sensitive to the active layer thickness than to its doping.

The transconductance dependence on V_{ds} for Device V is shown in Fig. 4.17. This device produces the highest transconductance obtained throughout this study, above 400 mS/mm. On the other hand, the gate-to-source-capacitance is also the highest obtained, as shown in Fig. 4.18. Nevertheless, this high capacitance does not impair the potential of this device since its current-gain-cutoff frequency is still high, more than 63 GHz.

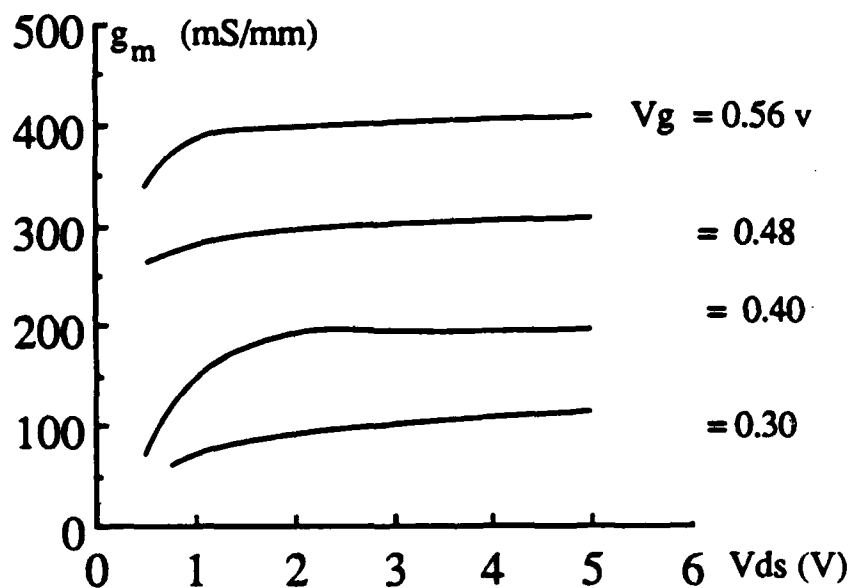


Fig. 4.17. The transconductance, in mS/mm, of the INGIFET, Device V, as function of the drain voltage at different gate voltages.

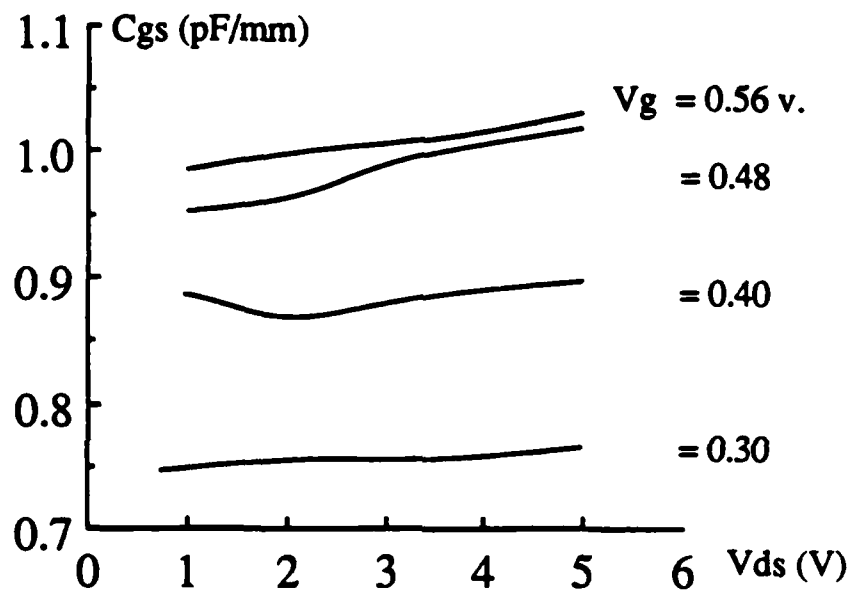


Fig. 4.18. The gate-to-source-capacitance, in pF/mm, of the INGIFET, Device V, as a function of the drain voltage at different gate voltages.

For rapid comparison between these different structures, the current-gain-cutoff frequencies will be presented as function of V_g at $V_{ds} = 5.0$ volts, for Device II (INGFET), Device III (coplanar MESFET) and Device V (INGIFET) in Fig. 4.19. This figure clearly manifests the superiority of the inverted-gate structures over the coplanar MESFET's. This suggests that these non-coplanar structures can be used even in the case when the traveling-wave phenomenon along the device electrodes is irrelevant.

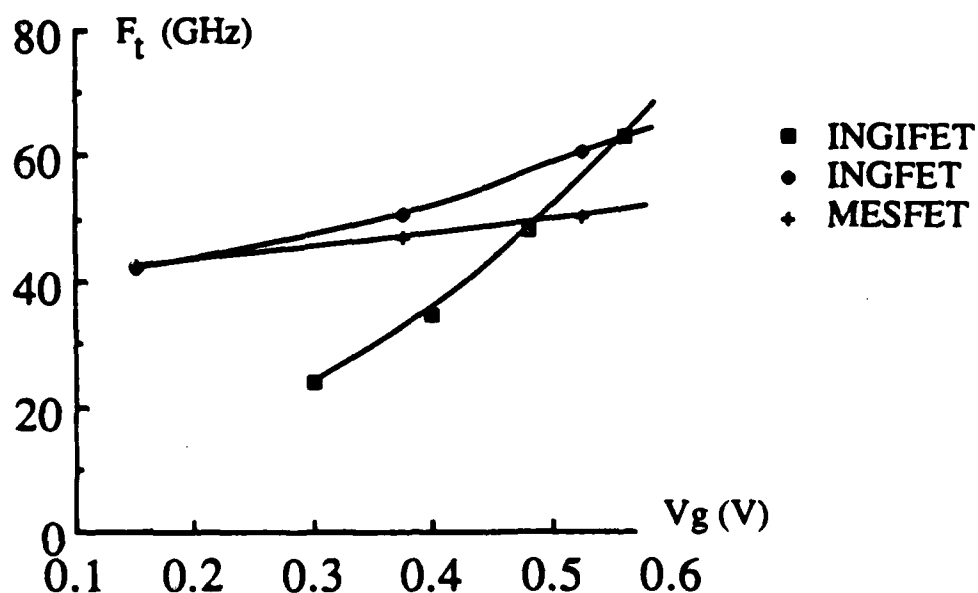


Fig. 4.19. The current-gain cutoff frequency as a function of V_g of the INGFET, Device II, the coplanar MESFET, Device III, and the INGIFET, Device V. Drain voltage = 5 V.

CHAPTER 5.

CONCLUSION

In this study, some novel MESFET structures are proposed. Their performance is evaluated using a suitable computer simulation.

By careful integration of Boltzmann Transport Equation and its moments, a set of conservation equations which is valid over a single valley of a semiconductor is derived. These equations are averaged over the upper and lower valleys of the GaAs to derive a set of hydrodynamic conservation equations that can be used to simulate the multi-valley semiconductor using its equivalent single electron gas. The characteristics of this equivalent gas are the average weighted characteristics of the constituting gases. The nonstationary effects, such as the velocity overshoot, are included by considering the mobility, the electron temperature and the energy relaxation-time as energy dependent parameters instead of being immediate functions of the local electric field. The dependence of these parameters on the average electron energy is obtained from Monte-Carlo simulations at steady state. A finite difference scheme is used to discretize these equations into a two-dimensional mesh over the device cross-section including the upper part of the substrate or the buffer-layer. The equations are decoupled in time using the semi-implicit scheme.

In order to extract the effect of the carrier injection from the MESFET active-layer, three MESFET structures with different substrate effects are simulated. It is observed that the carrier injection into the MESFET buffer-layer increases the drain current in the saturation region. The current also shows a continuous increase with the drain voltage. The MESFET dynamic range is increased as well. This results in a relatively low transconductance but with a smaller amount of nonlinearity with the gate voltage. The substrate-less MESFET produces a smaller current in the saturation region. The transconductance is high for the open channel but it rapidly drops by closing the channel. The drain conductance of this device is much smaller than the MESFET on a buffer-layer. A third MESFET, in which the carriers are partially confined to the active-layer due to an interfacial potential barrier created by a P type substrate, is also simulated. The characteristics of this MESFET are intermediate

between those of the other two devices. This suggests that a P substrate can be used to reduce the carrier injection from the active-layer of the MESFET. However, the thickness of the active-layer has to be increased in order to compensate for the partial depletion caused by the P-N junction created at the interface.

To optimize the doping of the P-substrate, three MESFET's on P-substrates of different acceptor dopings are simulated. It is shown that the resulting potential-barrier between the active-layer and the substrate greatly reduces the carrier injection from the active-layer. However, increasing the doping of the P-substrate leads to a more depletion in the active layer and, of course, a lower drain current. For MESFET with a thin active-layer, it is advised to use a thin P-layer between the SI substrate and the N active-layer. The P-layer should be so thin that it becomes fully depleted. The height of the potential barrier should be chosen such that it is capable of producing a good carrier confinement without too much depletion in the active-layer. It can be adjusted by controlling either the thickness or the doping of the P-layer or both.

This study also shows that relatively-thick-active-layer GaAs MESFET's can support traveling Gunn domains for the open channel. The oscillation frequency of these domains is much higher than the normal operating frequency of the MESFET. The travelling domain becomes stationary by increasing the reverse bias of the gate (i.e. by making the channel narrower). Reducing the thickness of the active layer permanently suppresses the traveling domain. However, the stationary domain exists for open channel.

Another new MESFET structure is introduced, the Inverted-Gate FET (INGFET). This INGFET has the ability to operate as a Traveling-Wave Transistor. Its design greatly reduces the parasitic gate resistance. The D.C. characteristics of the INGFET are simulated for the first time. It is shown that a traveling domain may exist inside this device for some bias combinations. A design that is permanently free from the traveling domain is easily obtained. The drain current of the INGFET has a smaller value and shows a lower drain voltage dependence in the saturation region, compared to that of the coplanar MESFET. This is due to the electron confinement to the active-layer in the case of the INGFET. The transconductance of the INGFET is higher than that of the conventional MESFET at high gate voltage. It drops below that of the conventional MESFET at low gate bias. The gate-to-source capacitance is

always lower than that of the conventional MESFET for the same bias combination. This results in a higher current-gain-cutoff frequency for the INGfET.

Inserting an intrinsic region in the middle of the active layer of the INGfET produces a very flexible device from the design point of view. Moreover, this increases the electron mobility under the gate and, hence, reduces the electron transit time. This device is called Inverted- Gate-Injection FET (INGIFET). The INGIFET shows a triode-like I-V characteristics, for relatively low doped N^+ regions, due to the space-charge-limited current flow. The INGIFET demonstrates the highest transconductance obtained throughout this study. Its gate-to-source capacitance is high compared to the other structures. However, an optimization study must be performed in order to reduce this capacitance and obtain the highest possible transconductance in the same time.

Future research in this domain can be directed towards improving the simulation program by including more physical phenomena in it. For example, the surface potential, the traps in the substrate, heterojunction effects,... etc. may be implemented in the program. A more intensive study of the effect of the thin P-layer on the overall performance is required. It is also interesting to compare the different effects, if any, of the thin P-layer on epitaxially grown active-layers and on ion-implanted ones. One may also perform an optimization study on the INGIFET to more exploit its potential characteristics. The traveling-wave aspect of the INGfET and the INGIFET is an interesting topic which has to be thoroughly investigated.

REFERENCES

- [1] E. Constant; "Modeling of Sub-Micron Devices," Inst. Phys. Conf., No. 57, p. 141, 1981.
- [2] M. Reiser; "A Two-Dimensional Numerical FET Model for DC, AC and Large-Signal Analysis," IEEE Trans. Electron Devices, vol. ED-20, No. 1, pp 35-45, 1973.
- [3] K. Yamaguchi, S. Asai and H. Kodera; "Two-Dimensional Numerical Analysis of Stability Criteria of GaAs FET's," IEEE Trans. Electron Devices, vol ED-23, pp. 1283-1290, 1976.
- [4] J. Barnes, R. Lomax and G. Haddad; "Finite Element Simulation of GaAs MESFET's with Lateral Doping Profiles and Submicron Gates," IEEE Trans. Electron Devices, vol. ED-23, No. 9, pp. 1042-1048, 1976.
- [5] A. Kaszynski; Etudes des Phenomenes Transport Dans Les Materiaux Semiconducteurs Par Les Methodes de Monte-Carlo. These de Docteur d'Ingenieur: Université des Sciences et Techniques de Lille, France, 1979.
- [6] M. Shur; "Influence of Nonuniform Field Distribution on Frequency Limits of GaAs Field-Effect Transistors," Electron. Lett., vol. 12, No. 23, pp. 615-616, 1976.
- [7] M. Shur, GaAs Devices and Circuits. New York: Plenum Press, 1987.
- [8] A. Cappy, Sur un Nouveau Modele de Transistor a Effect de Champ a Grille Submicronique. These de Troisieme Cycle: Universite des Sciences et Techniques de Lille, France, 1981.
- [9] R. Cook and J. Frey; " Two-Dimensional Numerical Simulation of Energy Transport Effects in Si and GaAs MESFET's," IEEE Trans. Electron Devices, vol. ED-29, No 6, pp. 970-977, 1982.
- [10] W. Curtice and Y. Yun; " A Temperature Model for the GaAs MESFET," IEEE Trans. Electron Devices, vol. ED-28, No 8, pp. 954-962, 1981.

- [11] S. El-Ghazaly, M. Lefebvre, G. Salmer, M. Ibrahim and O.L. El-Sayed; "Two Dimensional FET Simulation in Non-Stationary Conditions," Proceedings of the 13th European Solid State Device Research Conference, Canterbury, England, P 127, 1983.
- [12] C. Snowden and D. Loret; "Two-Dimensional Hot-Electron Models for Short-Gate-Length GaAs MESFET's," IEEE Trans. Electron Devices, vol. ED-34, No 2, pp. 212-223, 1987.
- [13] K. Blotekjaer; "Transport Equations for Electrons in Two-Valley Semiconductors," IEEE Trans. Electron Devices, vol. ED-17, No. 1, pp. 38-47, 1970.
- [14] M. Ibrahim, Two Dimensional Simulation of Microwave Gallium Arsenide Submicronic-Gate Field-Effect Transistor. M.Sc. Thesis: Cairo University, Egypt, 1983.
- [15] S. El-Ghazaly, Effect of Substrate and Gate Length on the GaAs MESFET Performance. M.Sc. Thesis: Cairo University, Egypt, 1983.
- [16] M. Reiser; "On the Stability of Finite Difference Schemes in Transient Semiconductor Problems," Computer Methods in Applied Mathematics and Engineering, 2, pp. 65-68, 1973.
- [17] R. Hockney; "The Potential Calculation and Some Applications," Math. in Comp. Physics, 9, p. 135, 1970.
- [18] G. Salmer, M. Lefebvre, F. Heliodore, O.L. El-Sayed, K. Isamil and S. El-Ghazaly; "Substrate Effects in Submicronic Gate Low Noise GaAs MESFET's," Gallium Arsenide and Related Compounds (Inst. Phys. Conf. Ser. No. 74), pp. 503-507, 1984.
- [19] N. Yokoyama, A. Shibatomi, S. Ohkawa, M. Fukuta and H. Ishikawa; "Electrical Properties of the Interface Between an N-GaAs Epitaxial Layer and a Cr-Doped Substrate," Gallium Arsenide and Related Compounds (Inst. Phys. Conf. Ser. No. 33b), pp. 201-209, 1977.
- [20] K. Kitahara, K. Nakai, A. Shibatomi and S. Ohkawa; "Electrical and Photoelectronic Properties of Cr-Doped Semi-Insulating GaAs," J. Appl. Phys, vol. 50, No 8, pp 5339-5344, 1979.
- [21] J.V. DiLorenzo and D.D. Khandelwal; GaAs FET Principles and Technology. Artech House: Massachusetts, 1982.

- [22] Y.M. Houngh and G.L. Pearson; "Deep Trapping Effects at the GaAs-GaAs:Cr Interface in GaAs FET Structures," J. Appl. Phys., vol. 49, No 6, pp 3348-3352, 1978.
- [23] P. Bonjour, R. Castagne, J-F.Pone, J-P. Courat, G. Bert, G. Nuzillat and M. Peltier; "Saturation Mechanism in 1- μ m Gate GaAs FET with Channel-Substrate Interfacial Barrier," IEEE Trans. Electron Devices, vol. ED-27, No 6, pp 1019-1024, 1980.
- [24] T. Itoh and H. Yanai; "Stability of Performance and Interfacial Problems in GaAs MESFET's," IEEE Trans. Electron Devices, vol ED-27, No 6, pp 1037-1045, 1980.
- [25] R.H. Wallis, A. Faucher, D. Pons and P.R.Jay; "Surface and Bulk Traps in GaAs MESFET's," Gallium Arsenide and Related Compounds (Inst. Phys. Conf. Ser. No. 74), pp. 287-292, 1984.
- [26] F.J. Tegude and K. Heime; "Investigation of Deep Levels at Interfaces by Means of FET Structures and Optical excitation," Gallium Arsenide and Related Compounds (Inst. Phys. Conf. Ser. No. 74), pp. 305-310, 1984.
- [27] C.P. Lee, S.J. Lee and B.M. Welch; "Carrier Injection and Backgating Effects in GaAs MESFET's," IEEE Trans. ED Letters, 3, No 4, pp 97-98, 1982.
- [28] S. Makram-Ebied and P. Minondo; "The Roles of the Surface and Bulk of the Semi-Insulating Substrate in Low-Frequency Anomalies of GaAs Integrated Circuits," IEEE Trans. Electron Devices, vol. ED-32, No 3, pp. 632-642, 1985.
- [29] S. El-Ghazaly, T. Itoh and G. Salmer; " Optimization of the P Substrate Doping for the N Channel GaAs Submicronic-Gate MESFET," National Radio Science Meeting, Boulder, Colorado, 1988.
- [30] T. Enoki, K. Yamasaki, K. Osafune, K. Ohwada; " 0.3- μ m Advanced SAINT FET's Having Asymmetric n^+ -Layers for Ultra-High-Frequency GaAs MMIC's," IEEE Trans. Electron Devices, vol. ED-35, no. 1, pp.18-24, 1988.
- [31] R. Engelmann and C. Liechti; "Bias Dependence of GaAs and InP Parameters," IEEE trans. Electron Devices, vol ED-24, pp. 1288-1296, 1977.
- [32] T. Fjeldly and J. Johannessen; "Negative Differential Resistance in GaAS MESFET's," Electron. lett., vol 19, pp. 649-650, 1983.

- [33] T. Fjeldly; "Analytical Modeling of the Stationary Domain in GaAs MESFET's," *IEEE Trans. Electron Devices*, vol. ED-33, No. 7, pp. 874-880, 1986.
- [34] A. Holden, D. Daniel, I. Davis, C. Oxley and H. Rees; " Gallium Arsenide Traveling-Wave Field-Effect Transistors," *IEEE Trans. Electron Devices*, vol. ED-32, No 1, pp. 61-66, 1985.
- [35] K. Fricke and H. Hartnagel; " Experimental Study of MESFET Travelling-Wave Structures," *Int. J. Electronics*, vol. 58, No 4, pp. 629-638, 1985.
- [36] W. Heinrich; " Distributed Equivalent-Circuit Model for Traveling-Wave FET Design," *IEEE Trans. Microwave Theory Tech.*, vol. MTT-35, No 5, pp. 487-491, 1987.
- [37] K. Kretschmer, P. Grambow and T. Sigulla; " Coupled-Mode Analysis of Travelling-Wave MESFET's," *Int. J. Electronics*, vol. 58, No 4, pp. 639-648, 1985.
- [38] M. Yoder, Private information.
- [39] S. El-Ghazaly and T. Itoh; " Inverted-Gate GaAs MESFET Characteristics," *Proceedings of the 17th European Microwave Conf.*, Rome, Italy, 1987.
- [40] J. Krusius and J. Bernez; " Simulation of the Novel High-Frequency FET with an Opposed Gate-Source Structure," *IEEE Trans. Electron Devices*, vol. ED-30, No 9, pp. 1116-1123, 1983.
- [41] L. Eastman, R. Stall, D. Woodard, N. Dandekar, C. Wood, M. Shur and K. Board; "Ballistic Electron Motion in GaAs at Room Temperature," *Electron. Lett.*, vol. 16, pp. 524-525, 1980.
- [42] R. Fauquembergue, M. Pernisek and E. Constant; " Monte-Carlo Simulation of Space-Charge Injection FET," *Electron. Lett.*, vol. 18, pp. 670-671, 1982.
- [43] P. Richman; " Modulation of Space-Charge-Limited Current Flow in Insulated-Gate Field-Effect Tetrodes," *IEEE Trans. Electron Devices*, vol. ED-16, No 9, pp. 759-766, 1969.
- [44] J. Geurst; "Theory of Insulated-Gate Field-Effect Transistors Near and Beyond Pinch-off," *Solid-State Electronics*, vol. 9, pp. 129-142, 1966.
- [45] G. Neumark and E. Rittner; " Transition From Pentode- to Triode-Like Characteristics in Field Effect Transistors," *Solid-State Electronics*, vol.10, pp.299-304, 1967.